Demonstration of High Energy-Transfer Efficiency for Quality-Preserving, Beam-Driven Plasma-Wakefield Accelerators

Demonstration von hoher Energietransfereffizienz
für einen qualitätserhaltenden, mit Elektronenbündel getriebenen
Plasma Kielfeld-Beschleuniger

Dissertation
zur Erlangung des Doktorgrades
an der Fakultät für Mathematik, Informatik und Naturwissenschaften
Fachbereich Physik
der Universität Hamburg

vorgelegt von

Felipe Lars Peña Asmus

Hamburg, 2024

Universität Hamburg
DER FORSCHUNG | DER LEHRE | DER BILDUNG

DESY.

Gutachter/innen der Dissertation:	Prof. Dr. Wolfgang Hillert
	Dr. Carl A. Lindstrøm
Zusammensetzung der Prüfungskommission:	Prof. Dr. Daniela Pfannkuche
	Prof. Dr. Wolfgang Hillert
	Dr. Carl A. Lindstrøm
	Prof. Dr. Peter Hauschildt
	Prof. Dr. Richard D'Arcy
Vorsitzende/r der Prüfungskommission:	Prof. Dr. Daniela Pfannkuche
Vorsitzender des Fach-Promotionsausschusses Physik:	Prof. Dr. Markus Drescher
Leiter des Fachbereichs Physik:	Prof. Dr. Wolfgang J. Parak
Dekan der Fakultät MIN:	Prof. Dr.-Ing. Norbert Ritter
Datum der Disputation:	19.06.2024

Eidesstattliche Versicherung / Declaration on oath

Hiermit versichere ich an Eides statt, die vorliegende Dissertation selbst verfasst und keine anderen als die angegebenen Hilfsmittel und Quellen genutzt zu haben. Die eingereichte schriftliche Fassung entspricht der auf dem elektronischen Speichermedium. Die Dissertation wurde in der vorgelegten oder einer ähnlichen Form nicht schon einmal in einem früheren Promotionsverfahren eingereicht.

I hereby affirm that I wrote the present dissertation myself and that I have not used any other sources than those given. The written version submitted corresponds to that on the electronic storage medium. The dissertation was not submitted in the present or in a similar form in an earlier doctoral procedure.

Hamburg, den 16.04.2024

Felipe Lars Peña Asmus

Abstract

With the advancement of climate change, greenhouse gas emissions in all aspects of society must be reduced, including research. Particle collider and free-electron laser (FEL) facilities have become increasingly large as their scientific reach has been extended by using higher-energetic particles. While they have proven indispensable in fundamental research and industry and have impelled technological advances, they also have a large environmental footprint.

Plasma accelerators, which accelerate particle bunches in the wakefields of a charged bunch propagating through a plasma, can sustain orders-of-magnitude-greater accelerating gradients than state-of-the-art accelerators. This would shrink the size of collider and FEL facilities, reducing their construction-arising environmental footprint and costs. However, a large fraction of the carbon footprint across the lifetime of such high-beam-power machines comes from power consumption during operation. Plasma accelerators must operate at high energy-transfer efficiency to ensure that the benefits of a smaller facility are not rendered futile by excessive power consumption. This thesis treats the topic of energy efficiency in plasma accelerators, presenting experimental results with high energy efficiency in the two transfers occurring within the plasma: from the driving bunch to the plasma and from the plasma to the accelerating bunch. However, these types of facilities require high-quality bunches. Therefore, the experimental results must also be relevant for quality-preserving acceleration.

Measuring high-quality bunches and a high energy-transfer efficiency requires precise diagnostics, for which a detailed dipole spectrometer calibration is performed. This allowed demonstrating experimentally the acceleration of a particle bunch at 0.8 GV/m while preserving its energy spread, charge, and transverse emittance. The plasma-to-accelerating-bunch energy-transfer efficiency in this first quality-preserving working point is 22%, close to the literature's record efficiencies.

The main result of this thesis is the experimental demonstration of $(59 \pm 3)\%$ driver-to-plasma energy-transfer efficiency – an order of magnitude larger than previous results in the literature. This result was achieved at the limit of re-acceleration, a process that would hinder preserving the quality of an accelerating bunch, where the first driver electrons become non-relativistic, slip backward in phase and get re-accelerated. For the first time, this process, which limits the energy efficiency of a plasma accelerator, is measured in detail and with two separate diagnostics.

While the high efficiency of these results was achieved separately, they represent key milestones in demonstrating high-efficiency and quality-preserving plasma accelerators.

Zusammenfassung

Angesichts des fortschreitenden Klimawandels müssen die Treibhausgasemissionen in allen Bereichen der Gesellschaft reduziert werden. Dies betrifft auch die Forschung, wo Teilchenbeschleuniger und Freie-Elektronen-Laser (FEL) immer größer werden, da ihre wissenschaftliche Reichweite durch noch energetischere Teilchen erweitert wird. Solche Einrichtungen haben sich in der Grundlagenforschung und in der Industrie als unentbehrlich erwiesen, aber sie haben auch einen großen ökologischen Fußabdruck.

Mittels Plasma kann ein Teilchenbündel im Kielfeld eines vorläufigen Bündels beschleunigt werden. Die Gradienten können um Größenordnungen höher sein als in der derzeitig verwendeten Beschleunigertechnologie. Dies würde die Länge von Teilchenbeschleuniger- und FEL-Einrichtungen verkürzen und somit auch ihren ökologischen Fußabdruck und die Baukosten reduzieren. Ein substantieller Teil des gesamten Fußabdrucks solcher Maschinen ist jedoch durch den Stromverbrauch während des Betriebs bestimmt. Damit die ersparten Treibhausemissionen nicht durch einen erhöhten Stromverbrauch zunichte getragen werden, müssen Plasmabeschleuniger mit hoher Energieübertragungseffizienz arbeiten. Die vorliegende Dissertation befasst sich mit diesem Thema und präsentiert experimentelle Ergebnisse mit hoher Energieeffizienz in den zwei Transfers innerhalb des Plasmas: vom treibenden Bündel zum Plasma und vom Plasma zum beschleunigenden Bündel. Da für diese Art von Einrichtungen hochwertige Bündel erforderlich sind, wird der Fokus auf qualitätserhaltende Ergebnisse gesetzt. Dies erfordert präzise Diagnostiken, weshalb eine detaillierte Kalibrierung durchgeführt wird. Auf diese Weise konnte experimentell die Beschleunigung eines Teilchenbündels mit 0,8 GV/m unter Beibehaltung seiner transversalen Emittanz nachgewiesen werden. Dabei beträgt die Energietransfereffizienz vom Plasma zu dem beschleunigten Teilchenbündel 22% und ist vergleichbar zu den Rekordwerten in der Literatur.

Das wichtigste Ergebnis dieser Arbeit ist der experimentelle Nachweis, dass ein treibendes Bündel $(59 \pm 3)\%$ seiner ursprünglichen Energie im Plasma deponiert, was eine Größenordnung über den bisherigen Ergebnissen ist. Dies wurde kurz vor dem Prozess gemessen, wo treibende Elektronen auf nichtrelativistischen Energien verlangsamt und wieder beschleunigt werden, welches die Erhaltung der Qualität eines beschleunigten Bündels verhindern würde. Dieser Prozess, welcher somit die Energieeffizienz eines Plasmabeschleunigers begrenzt, wird hier zum ersten Mal detailliert gemessen.

Auch wenn die hohe Effizienz dieser Ergebnisse in getrennten Messungen erzielt wurde, stellen sie einen wichtigen Meilenstein zur Demonstration hocheffizienter und qualitätserhaltender Plasmabeschleuniger dar.

Resumen

Ante el avance del cambio climático, debemos reducir las emisiones de gases de efecto invernadero (GEI) en todos los aspectos de la sociedad, incluyendo la investigación. En este ámbito, colisionadores de partículas y láseres de electrones libres (free-electron lasers, FELs) han ido agrandándose a medida que se ampliaba su alcance científico mediante partículas más energéticas. Aunque se han demostrado indispensables en la investigación básica y en la industria, también tienen una gran huella medioambiental.

Los aceleradores de plasma, que aceleran haces de partículas en los campos de estela de otro haz propagando a través de un plasma, pueden mantener gradientes de aceleración de órdenes de magnitud mayores que los aceleradores más modernos. Esto reduciría el tamaño de colisionadores y FELs, y con ello su huella medioambiental y los costes de construcción. Sin embargo, una gran parte de la huella medioambiental durante su vida útil tiene su origen en el consumo energético durante su funcionamiento. Por lo tanto, los aceleradores de plasma deben operar con una alta eficiencia energética para conseguir una reducción neta de emisiones de GEI. Esta tesis doctoral trata este tema, presentando resultados experimentales con alta eficiencia energética en las dos transferencias que ocurren dentro del plasma: del haz impulsor al plasma y del plasma al haz acelerador. Dado que este tipo de instalaciones requieren haces de alta calidad, se presta especial atención a resultados que puedan mantener la calidad del haz acelerante.

La medición de haces de alta calidad y acelerados con alta eficiencia energética requieren diagnósticos precisos, para lo cual se realiza una calibración detallada del espectrómetro dipolar. Esto permite demostrar experimentalmente la aceleración de un haz de partículas con un gradiente de aceleración de 0,8 GV/m y manteniendo su emitancia transversal. Aquí, la eficiencia de transferencia energética (del plasma al haz acelerado) es del 22 %, similar a eficiencias récord.

El principal resultado de esta tesis doctoral es la demostración experimental del haz impulsor transfiriendo el (59 ± 3) % de su energía inicial al plasma, siendo los resultados una orden de magnitud mayor que los previos descritos en la literatura. Esto se consiguió justo antes del inicio del proceso en el cual electrones impulsores se convertirían en no relativistas y se acelerarían de nuevo, lo que evitaría mantener la calidad de un haz acelerador. Por primera vez, este proceso, que limita la eficiencia energética de un acelerador de plasma, se mide meticulosamente y con dos diagnósticos independientes.

Aunque la alta eficiencia de estos resultados se consiguió por separado, representan un hito clave en la demostración de aceleradores de plasma de alta eficiencia que mantengan la calidad del haz acelerador.

"Cuanto más amor das, mejor estás."

— Kase.O

Acknowledgments

The period of my PhD had many ups and downs, but I'm sure that the ups were caused by the excellent people I had the chance to work with, live or be befriended. I would like to acknowledge all those involved in some way, but I find it very hard as so many have helped in so many different aspects. I can only really share a subset of what they have contributed and taught me. Here goes an attempt.

I'm thankful to Professor Daniela Pfannkuche, Professor Wolfgang Hillert, Dr. Carl A. Lindstrøm, Professor Richard D'Arcy, and Professor Peter Hauschildt for agreeing to be part of the defense committee. Professor Wolfgang Hillert kindly agreed to be my doctoral supervisor and thesis reviewer.

I think I won the lottery by getting Carl A. Lindstrøm as a direct 'day-to-day' supervisor of my PhD. He is very supportive and, while trying to let me delve into science as independently as possible, he was always ready to lend a helping hand or brain to pull me out of rabbit holes and frustration. From him, I learned to keep in mind what one wants 'at the end of the day', which helps get things done. For me, he was not merely a supervisor, but a friend, and I hope that our paths continue to cross for many more years.

Approximately in the middle of my PhD, Carl left for his own green pasture in Oslo but continued to supervise me remotely, which, in my biased view, still worked great. At DESY, I decided to bother other great scientists and try to learn as much as possible from them. This includes Rob Shalloo, who, while working on quite a separate topic from mine, still regularly provided good advice, especially of the kind that keeps one sane. He also was one of those who read my first draft of the thesis and helped me see that it was horrible. He did not describe it as such and gave feedback in a motivating way, making sure not to lessen my spirit. I know that he is considered by many as a role model. I also considerably bothered Maxence Thévenet, who patiently explained to me theory regarding plasma wakefields and intricacies in simulations, and was always keen on providing feedback on drafts. As this is getting long, I'll try to summarize a bit:

- Stephan Wesch is the Rückgrat of FLASHForward, a beacon of hope for anyone in disarray, and seemingly has infinite knowledge of FLASH and DESY.
- Richard D'Arcy has shown me how a scientific team can be managed effectively and how to steer it successfully to goals.
- Alberto Martinez de la Ossa y Ángel Ferran Pousa me aclararon muchas dudas de teoría y simulaciones, y me hicieron sentir como en España aunque afuera lloviera e hiciese frío.
- Jon Wood gave me good feedback on my thesis, which was tough and gave me a lot of work, but it greatly improved it. He also allowed me to retreat to finish this thesis, which partly led to him taking a significant amount of long night shifts.
- I had great discussions with Jens Osterhoff helping me understand what goals are important scientifically, for publications, and funding.

- Sandra Kottler helped me cope with IT shenanigans.
- I have a lot of respect for the expert technicians Kai Ludwig, Andrej Schleiermacher, and Amir Rahali, as only thanks to their knowledge and experience the experiment works.
- I'm thankful for the help Brian Foster has offered and delivered in writing manuscripts for publication, and for preparing me for the defense.
- Ich danke Daniela Koch für ihre Fürsorge, das Mitgefühl und netten Gespräche im Alltag.
- Jonas Björklund Svensson is a deep well of knowledge concerning all papers that exist out there that are somewhat related to our field. He has a keen mind for details and is a great person.

I was fortunate to have other PhD peers join me in my adventure. They all contributed by keeping me sane and realizing that struggle, frustration, and desperation were common feelings.

- Pau González Caminal, per recordar-me que trobo a faltar Catalunya, i per escriure una tesi increïble que em va ajudar a entendre el que jo estava fent en la meva pròpia tesi.
- Severin guided me through my first dive into the realm of simulations. While I kept bugging him with all my simulation problems, he never showed any annoyance. He also gave me a sonorous feedback slap concerning my first thesis draft – but he was right.
- Sarah Schröder was always eager to give feedback, including my first thesis draft.
- Cristina Mariani for being a beacon of positivity.
- Rino Farace for showing me how one can live carelessly.
- I shared office time with Advait Kanekar, which was fun with out-of-nowhere questions, banter, gossip, and jokes. In summary: great vibes.
- Lewis Boulton can stay cool even if nothing really works. He is a great teammate for (night) shifts, work, and drinks.
- I appreciated a lot the confidentiality with Judita when we asked each other the simple questions we were unsure if we could ask others. And, of course, the great gossip.

Me gustaría tambien expresar my agradecimiento a Papa, Mama y Julian, für eure Unterstützung von ganz Anfang an, als ich noch ein kleiner Zwerg war :)

Den Doktorgrad zu erlangen war kein leichtes Abenteuer für mich. Es war aber bestimmt auch nicht leicht für meine bessere Hälfte, die auch bereit war dafür wegzuziehen. Ich saß oft verzweifelt am Laptop und kam gefühlt nicht weiter. Ich konnte nie richtig

einschätzen, wann ich mit etwas fertig werden würde. Ich war oft am Wochenende mit Experimenten beschäftigt. Vielen Dank für deine Geduld und Verständnis, Katharina Meenenga. Du hast mir geholfen, nicht verrückt(er) zu werden.

Contents

Role of the Author

Experimental results in plasma-wakefield accelerators are generally a group effort, and the results presented in this thesis are no exception. They are the product of a multidisciplinary group of people. To help identify the work of the author in the experimental results presented in this thesis, the author's involvement is briefly disclosed here.

The main result of the thesis is the high driver-depletion efficiency in Chapter 5, with the team composed of F. Peña, C. A. Lindstrøm, J. Beinortaitė, J. Björklund Svensson, L. Boulton, S. Diederichs, B. Foster, J. M. Garland, P. González Caminal, G. Loisch, S. Schröder, M. Thévenet, S. Wesch, J. C. Wood, J. Osterhoff, and R. D'Arcy. The author led the experimental campaign and performed the spectrometer calibrations, data analysis, and simulations. While there was supervision and support from C. A. Lindstrøm in all these parts, others also contributed in their respective expert areas. J. Beinortaitė, J. Björklund Svensson, L. Boulton, P. González Caminal, S. Schröder, S. Wesch and J. C. Wood were vital in preparing and operating the FLASH accelerator. J. M. Garland and G. Loisch provided data and analysis for estimating the plasma density. S. Diederichs and M. Thévenet helped the author in setting up the initial simulations and continued supporting with guidance on issues concerning the simulations.

The experimental result presented in Sec. 4.2, demonstrating emittance preservation in a plasma accelerator, was led by C. A. Lindstrøm. Involved were also J. Beinortaitė, J. Björklund Svensson, L. Boulton, J. Chappell, S. Diederichs, B. Foster, J. M. Garland, P. González Caminal, G. Loisch, F. Peña, S. Schröder, M. Thévenet, S. Wesch, M. Wing, J. C. Wood, R. D'Arcy and J. Osterhoff. The author was involved in the varied experimental campaigns by helping set up and optimize the plasma interaction, providing guidance in the calibration of the spectrometer, and in detailed discussions of the analysis.

The work on the longitudinally resolved energy-extraction efficiency in Sec. 4.4 was led by L. Boulton, with involvement from C. A. Lindstrøm, J. Beinortaitė, J. Björklund Svensson, J. M. Garland, P. González Caminal, B. Hidding, G. Loisch, F. Peña, K. Põder, S. Schröder, S. Wesch, J. C. Wood, J. Osterhoff, and R. D'Arcy. Here, the author was involved in the experimental campaign by establishing the plasma interaction and optimizing for high energy-extraction efficiency, and by providing guidance on the spectrometer calibration.

List of Publications

The work presented in this thesis has led to preparing the following publications for submission:

F. Peña, C. A. Lindstrøm, J. Beinortaitė, J. Björklund Svensson, L. Boulton, S. Diederichs, B. Foster, J. M. Garland, P. González Caminal, G. Loisch, S. Schröder, M. Thévenet, S. Wesch, J. C. Wood, J. Osterhoff, and R. D'Arcy, **Energy Depletion and Re-Acceleration of Driver Electrons in a Plasma-Wakefield Accelerator**, *in review*

DOI: 10.48550/arXiv.2305.09581

C. A. Lindstrøm, J. Beinortaitė, J. Björklund Svensson, L. Boulton, J. Chappell, S. Diederichs, B. Foster, J. M. Garland, P. González Caminal, G. Loisch, **F. Peña**, S. Schröder, M. Thévenet, S. Wesch, M. Wing, J. C. Wood, R. D'Arcy and J. Osterhoff. **Emittance preservation in a plasma-wakefield accelerator**, *in review*

DOI: 10.48550/arXiv.2403.17855

L. Boulton, C. A. Lindstrøm, J. Beinortaitė, J. Björklund Svensson, J. M. Garland, P. González Caminal, B. Hidding, G. Loisch, **F. Peña**, K. Põder, S. Schröder, S. Wesch, J. C. Wood, J. Osterhoff, and R. D'Arcy, **Longitudinally Resolved Measurement of Energy-Transfer Efficiency in a Plasma-Wakefield Accelerator**, *in review*

DOI: 10.48550/arXiv.2209.06690

The author was also involved in other experimental results not covered in this thesis that led to publications or manuscripts:

C.A. Lindstrøm, J. Beinortaitė, J. Björklund Svensson, L. Boulton, J. Chappell, J.M. Garland, P. González Caminal, G. Loisch, **F. Peña**, L. Schaper, B. Schmidt, S. Schröder, S. Wesch, J. Wood, J. Osterhoff and R. D'Arcy, **Progress of the FLASHForward X-2 high-beam-quality, high-efficiency plasma-accelerator experiment**, *Proceedings of The European Physical Society Conference on High Energy Physics – PoS(EPS-HEP2021).* Vol. 398, (2022), p.880.

DOI: 10.22323/1.398.0880

J. C. Wood, L. Boulton, J. Beinortaitė, J. Björklund Svensson, S. Bohlen, G. Boyle, J. M. Garland, P. Gonzalez Caminal, C. A. Lindstrøm, G. Loisch, S. M. Mewes, T. Parikh, **F. Peña**, K. Põder, S. Schröder, M. Thévenet, S. Wesch, J. Osterhoff, and R. D'Arcy, **Brightness-Boosted Electron Bunches from a Plasma Accelerator**, *in review*

List of Figures

List of Tables

Chapter 1

Introduction

With decades of research, it has become unequivocal that the world's climate is changing. Driven by human action, this catastrophe will lead to a significant increase in extreme weather events such as droughts, flooding, and forest fires [1]. It is the responsibility of each individual to reduce the emission of *greenhouse gasses* (GHG) driving the climate crisis, for example, by advocating for governmental changes and adapting our lifestyles[†]. These changes have to come in all aspects of society, including research infrastructure. As these can become quite large, they will fall under stronger public scrutiny due to their environmental footprint.

For the general public, possibly the first research infrastructure that comes to mind is the *Large Hadron Collider* (LHC) [3], which led to the discovery of the Higgs boson [4, 5]. For this, a tunnel with a 27 km circumference was built 100 m below the surface in the Geneva area. Constructing such a tunnel and the accelerator it houses is bound to impact the environment with, among others, a large emission of GHG. Considering the history of ever-larger collider facilities and new proposals with up to a 100 km circumference, it has become unavoidable to consider the environmental footprint of such machines and develop strategies to reduce GHG emissions.

[†]A detailed analysis, discussion, and list of recommendations regarding research in *High Energy Physics, Cosmology, Astroparticle Physics, and Hadron and Nuclear Physics* (HECAP+) can be found in Ref. [2].

Admittedly, the smallest environmental impact is not constructing such research facilities at all. However, accelerators provide significant benefits to the broader public. In high-energy particle colliders, they give us the ability to research the fundamental constituents of matter. Over time, this has led to the discovery of many fundamental particles, such as the W and Z bosons in 1983 [6], the top quark in 1995 [7, 8], or the Higgs boson in 2012 [4, 5]. During the process of design, construction, and operation of such colliders, many diverse benefits have come out. These range from the creation of the World Wide Web, which was developed by scientists for effective communication within international collaborations, to medical positron-emission tomography (PET) scans, where the detectors used are based on detectors developed for particle colliders. Furthermore, accelerators themselves have been found useful for various applications, remarkably summarized in Ref. [9] with:

> "*A beam of the right particles with the right energy at the right intensity can shrink a tumor, produce cleaner energy, spot suspicious cargo, make a better radial tire, clean up dirty drinking water, map a protein, study a nuclear explosion, design a new drug, make a heat-resistant automotive cable, diagnose a disease, reduce nuclear waste, detect an art forgery, implant ions in a semiconductor, prospect for oil, date an archaeological find, package a Thanksgiving turkey or discover the secrets of the universe.*"

As a consequence of such versatility, there are more than 46 000 commercial accelerators worldwide [9–11]. A special application of accelerators is their use for free-electron lasers (FELs), where, in essence, radiation is produced by passing an accelerated charged particle bunch through alternating magnetic fields. Such radiation can be used in various research fields [12], e.g., in structural biology to image proteins [13], in photochemistry to investigate electronic and structural changes from photoexcitation [14], in shock physics to measure the response of solids to high-pressure shocks [15], and in the industry for imaging lattice strain during the manufacture of materials such as metals [16].

As particle accelerators have clear benefits, be it as particle colliders, FELs, or spin-offs in the industry, it would be valuable to continue developing and constructing them. As a result, the financial and environmental price tag must be balanced with their benefits to a reasonable burden for society and the climate. This difficult act is out of the scope of this thesis. Instead, a different approach can be pursued: reducing the environmental footprint of accelerator facilities with the use of a different acceleration scheme. In the following sections, first, the underlying reason for long(er) accelerator facilities is introduced. Then, a possible path to reduce the environmental footprint with plasma accelerators is presented, which is then compared to other proposed collider schemes. Finally, key requirements for plasma accelerators are introduced if they are to be used for colliders. These include the preservation of beam quality during the acceleration and high energy-transfer efficiency, being the topics treated in this thesis.

1.1 Why so big?

For colliders, the energy at which the particles collide determines how much energy is available for producing new particles. Therefore, the more energy, the more massive the new particles can be. The LHC, as pictured on the top in Fig. 1.1, is a circular collider, where bunches of counter-propagating protons are intersected at different interaction points, where a small fraction of their protons collide. In such a design, the bunches can be reused by recirculating and repeatedly intersecting them, allowing for more collisions per bunch than in a single-pass collider. The circulation of the bunches is done by bending their trajectory with magnetic fields. This becomes more difficult for higher particle energies, and the maximum magnetic field strengths determine the radius of the collider*. An added benefit of this design is that the bunches use the accelerating section repeatedly, allowing the use of a low accelerating gradient.

Instead of recirculating the bunches through an accelerating section and the final

*A more detailed discussion on how the trajectory is bent can be found in Sec. 2.2.

Figure 1.1: In the top: aerial image of the CERN accelerator complex in the Geneva area. The 27-km-long LHC tunnel is marked in yellow, with the four different detectors marked in white. The pre-accelerator Super Proton Synchrotron (SPS) is marked in blue with various extraction lines. Image from Ref. [17]. In the bottom: aerial image of the European XFEL facility, with the start marked in orange on the bottom right and its end on the top left, spanning a length of 3.4 km. The accelerating section ends after 1.6 km, at around the center of the image, where the beamline is bifurcated. Image from Ref. [18].

particle energy being limited by the ability to bend its path, the particles can also be accelerated in a single-pass linear accelerator. This is the design of the *European X-Ray Free-Electron Laser Facility* (European XFEL) [19], depicted on the bottom in Fig. 1.1. Here, the particles do not collide. Instead, they are used to produce X-Ray radiation [20] and to, for example, observe proteins with sizes as small as 14 nm [21]. For FELs [12], the motivation for high energies is the ability to reach smaller radiated wavelengths, which in turn allows the investigation of smaller structures. For a given design energy, the length is determined by the accelerating gradient of the accelerating section, which is usually based on *radio-frequency* (RF) technology. Here, an alternating field is generated within cavities such that the particles, when passing through, experience an accelerating field. The gradient with which the particles can be accelerated is limited by electrical breakdown (sparking). The breakdown mechanism is not understood in detail, but electron field emission could be the initiating process [22, Chp. 5.10–11]. Nevertheless, the breakdown limit was empirically described in Ref. [23], and, as cited in Ref. [22], rewritten to [24]

$$f = 1.64\, E_K^2\, e^{-8.5/E_K}, \tag{1.1}$$

where f is the frequency in megahertz and E_K is the *Kilpatrick limit* in megavolts per meter, which is the maximum field* up to which breakdown-free operation is possible. The relationship in Eq. 1.1 is depicted in Fig. 1.2, showing that increasing the frequency allows using higher accelerating gradients. However, higher frequencies also require smaller cavity structures. For this reason, the gradients are usually 10–100 MV/m [26, 27]. In the case of the European XFEL, with a design accelerating gradient of 23.6 MV/m in the cavities [19], a 1.6 km long accelerating tunnel† was constructed to reach a maximum energy of 20 GeV.

*There have been significant advances in vacuum systems since then and new cavity systems can go beyond this limit, e.g., by a factor of two or more [25, Sec. 6.6].

†Accelerators do not only consist of accelerating modules but also other components such as for diagnosis and steering, which lower the average gradient. Also, while at the European XFEL 20 GeV is possible, the standard operation is at 17.5 GeV.

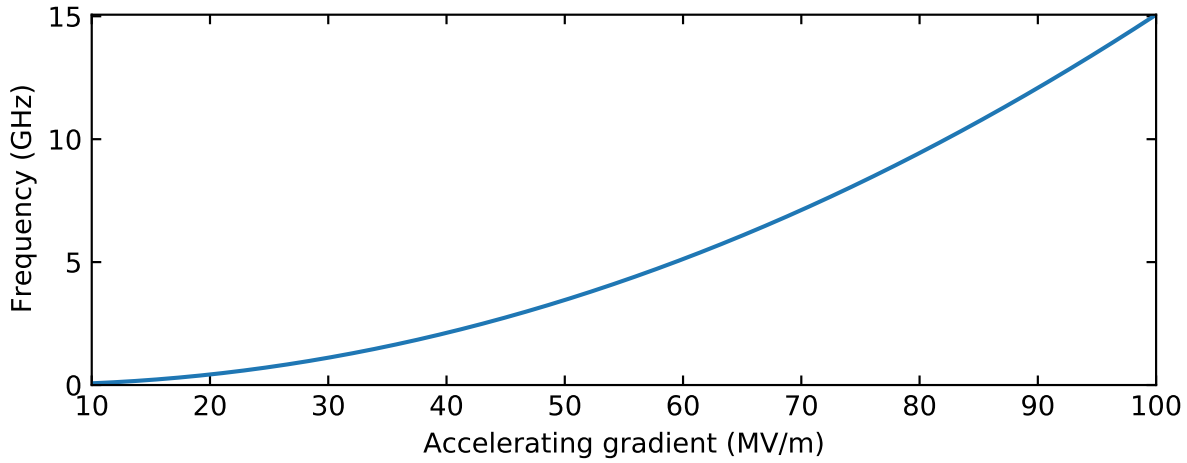

Figure 1.2: Relationship between the Kilpatrick limit and frequency, following Eq. 1.1.

1.2 A possible path for reducing the environmental footprint of accelerators

A possible way to reduce the environmental footprint of applications with high energies is plasma accelerator technology*. Its main selling point is the ability to sustain large accelerating gradients, generally of $\mathcal{O}$(1–100 GV/m), with up to 265 GV/m [28, 29] demonstrated experimentally. Such gradients could shrink the accelerator length, resulting in a lower environmental footprint from construction. As an example, Fig. 1.3 shows the proposed Hybrid, Asymmetric, Linear Higgs Factory (HALHF) [30]. Here, positrons and electrons are accelerated to 31 GeV with RF modules, and then, with plasma accelerator modules, the electrons are boosted to 500 GeV. This collider could lead to a similar scientific output to other proposed colliders like the *International Linear Collider* (ILC) [31] or *Compact Linear Collider* (CLIC) [27, 32], as their luminosity† is comparable. However, its length is only a fourth and third compared to the ILC and CLIC, respectively‡. As a significant fraction of GHG emissions arises from construction, this will be shown later with Fig. 1.4, such facility shortening suggests that the environmental

*This is treated in more detail in Sec. 2.4.

†This figure of merit is defined in Sec. 1.4.

‡With a 250 GeV center-of-mass energy, HALHF and the ILC have a luminosity of 0.81 and 1.35×10^{34} cm^{-2}s^{-1}, and a facility length of 3.3 and 13.3 km, respectively. For CLIC, at a 380 GeV center-of-mass energy, the corresponding values are 2.3×10^{34} cm^{-2}s^{-1} and 11.4 km.

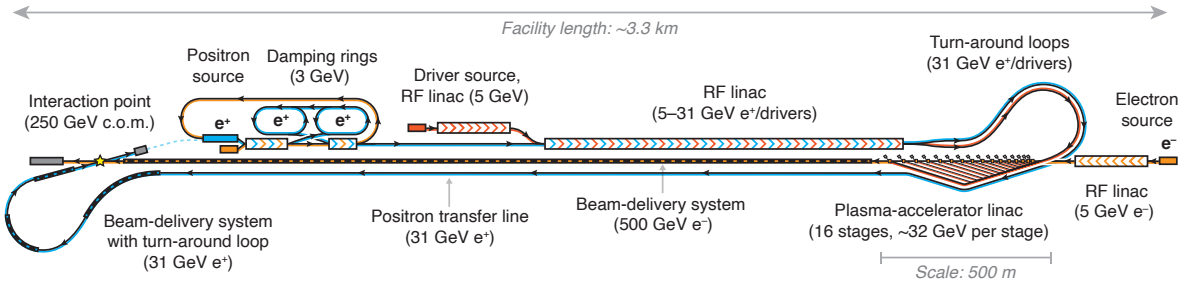

Figure 1.3: Schematic of the proposed HALHF collider. The positron bunches (blue) are produced and radiatively dampened and then accelerated together with electron drive bunches (red). After the turnaround, the drive bunches are used to accelerate an electron bunch (orange) in plasma stages, and the positrons are transferred to the interaction point at the other end. Image from Ref. [30] (CC-BY 4.0).

footprint could shrink similarly. In the HALHF design, only 80 m of the beamline is dedicated to plasma acceleration, and the rest uses the common RF accelerator technology. Therefore, the collider design could be considered, overall in terms of environmental footprint, as an RF-technology collider. It should be noted that, although the focus here is made on the environmental footprint, similar reasoning can be made with construction costs. Such a research facility could optimize the scientific output for the taxpayer's money.

While plasma accelerators promise a reduction in facility size, for applications such as colliders and FELs, high gradients alone are not sufficient. Further requirements need to be met to prove their suitability, with one being operation at a high repetition rate. Promising results show that ∼10 MHz is, in principle, possible [33]. However, the operation of plasma accelerators at a repetition rate > 1 kHz has not been demonstrated*. This topic is not treated in this Thesis; detailed discussions can be found in Refs. [33, 35]. While high-repetition-rate operation is often treated separately from beam-quality preservation and energy-transfer efficiency, there is a clear connection to the latter in plasma accelerators, which is further discussed in Sec. 4.

Other key requirements for plasma accelerators are operation at high energy-transfer

*Laser-driven plasma accelerators have produced few MeV electron bunches with ∼20 pC at 1 kHz [34].

efficiency and quality preservation of the accelerating beam. These aspects are discussed separately in the following two sections.

1.3 The importance of high energy-transfer efficiency

Fig. 1.4 shows, for proposed collider facilities, the *Global Warming Potential* (GWP), which quantifies the warming potential of GHG emissions in equivalent CO_2 mass (CO_2e) [2]. The GWP of the circular machines, i.e., the *Future Circular Collider* (FCC) [36, 37] and the *Circular Electron Positron Collider* (CEPC) [38, 39], is significantly above that of the linear colliders, dominated by emissions from construction due to their longer tunnels (see Table 1.1). The operational GWP was computed with the electricity consumption over the collider's lifetime, taking into account downtime, commissioning, and development times, as done in Ref [40]. The exact GWP per consumed power is determined by the local electrical mix. Based on the stated policies of each country, the GWP per produced power in 2040 will be 40, 45, 150, and 300 ton CO_2e/GWh , for the EU, USA, Japan, and China, respectively [41, Fig. 6.14]. As each project can lower the GWP relative to the region by implementing additional measures such as local renewable power production and reuse of heat waste (see Green ILC [42]), a common carbon intensity can be used in a comparison. Assuming an electricity-production carbon intensity of 20* ton CO_2e/GWh for all proposals, as in Ref. [40], reflects the expectation that the GWP of such productions will decrease over time. Under these assumptions, the GWP from running the different colliders can be estimated with their power consumption, and it is comparable to or even larger than that from construction.

For the HALHF proposal, the power consumption is estimated as follows. The power consumed by the collider during operation is approximately 100 MW. Assuming the same

*Currently, the carbon intensity of nuclear, wind, hydroelectric, and solar energy production is around 5, 15, 25, and 30 ton CO_2e/GWh, respectively [40].

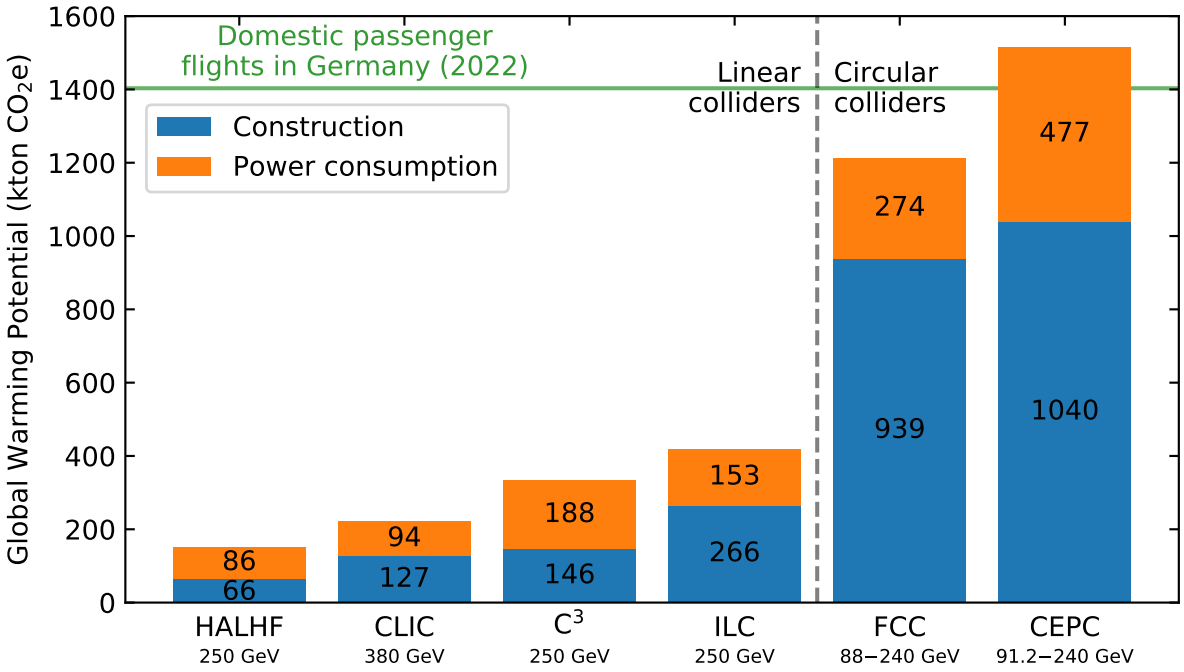

Figure 1.4: GWP from different colliders over their planned operational lifetime, with emissions from construction in blue and from power consumption in orange. The linear and circular colliders are separated by the vertical dashed line. The center-off-mass energy included for this estimation is noted below the name of each design. Note that for the C^3 design, energy-saving schemes reducing the power consumption by 44% were proposed [40]. Also note that this is a comparison of Higgs factories, and higher center-of-mass energies for other physics cases are considered in some designs, e.g. FCC and CEPC. As a reference, the GWP from German domestic passenger flights in 2022 is shown with the horizontal green line [43]. This Figure is an adaptation from Ref. [40] (CC-BY 4.0), with the HALHF GWP estimated as described in the text.

operation schedule across the year as for the other colliders in Ref. [40], which includes commissioning, machine development, and downtime, the average power consumption per year is 0.54 TWh. As a reference, the power demand of Geneva's canton, with a population of ∼514 000 [44], is 2.7 TWh/year [45]. With the same operational lifetime as CLIC (8 years), this yields a lifetime energy consumption of 4.3 TWh, resulting in 86 kton CO_2e from operation. From construction, as the length dedicated to plasma accelerators is negligible compared to that for RF technology, one can assume that the GWP will be similar to those with only RF technology. Table 1.1 shows that, for linear facilities, the GWP per kilometer constructed varies from 11–20 kton CO_2e.

Parameter	Unit	HALHF [30]	CLIC [27, 32]	C^3 [46]	ILC [47]	FCC [36, 37]	CEPC [38, 39]
Center-of-mass energy	GeV	250	380	250	250	88–240	91.2–240
Tunnel length	km	3.3	11.5	8.0	13.3	90.6	100.0
GWP from construction	kton CO_2e	66	127	146	266	939	1040
GWP from constr. per km	kton CO_2e/km	20	11	18	20	10	10
Peak power consumption	MW	100	110	150	111	222–273	283–340
Yearly power consumption	TWh/y	0.54	0.59	0.94	0.70	1.13–1.39	1.58–1.90
Operational lifetime	years	8	8	10	11	9	13

Table 1.1: Summary of parameters used for Fig. 1.4, with the values extracted from Ref.[40]. The GWP from construction for CLIC and ILC are reported in detail in Ref. [48], and this is used to estimate that of the FCC and CEPC. For C^3, Ref. [40] is used. To give a conservative estimate on HALHF, the same CO_2e/km as from the ILC is used, which is the largest from the linear colliders. For better comparison, the operational lifetime of HALHF is set equal to that of CLIC.

Assuming the highest emission per kilometer and a length of 3.3 km, HALHF's GWP from construction would be approximately 66 kton CO_2e.

Overall, the GWP of HALHF from construction and operation is the lowest of the proposed colliders, with 152 kton CO_2e, while the next lowest, CLIC, is at 221 kton CO_2e. It should be noted that the reduction in GWP is mainly achieved by a reduction in accelerator length. Also, the power consumed by HALHF is dependent on the assumed energy-transfer efficiency in the plasma accelerator stages, which is 38%. However, such an efficiency has not been demonstrated, and worse efficiency will increase the power consumption. In the extreme case, the reduced environmental footprint from construction can be rendered futile by an inefficient machine. While such a setup could still be financially advantageous, in the context of environmental footprint, energy inefficiency can render plasma accelerators in colliders useless. Therefore, for plasma accelerators to be used in high-beam-power facilities, high energy-transfer efficiency must be demonstrated. As an added incentive, this would also lower the running costs, as it decreases the electricity bill.

1.4 The requirements in beam quality

Applications such as colliders and FELs not only require high energy-transfer efficiency to keep their environmental footprint and costs reasonable, but they also require sufficient beam quality.

The figure of merit to describe the performance of colliders is the *luminosity* $\mathcal{L}$, which is the event rate $\frac{dR}{dt}$ divided by the unit cross-section of an interaction σ_{cs} [49], i.e.,

$$\frac{dR}{dt} = \mathcal{L} \cdot \sigma_{\text{cs}}. \tag{1.2}$$

The cross-section describes the probability of an interaction taking place. It is inherent to each process individually and scales inversely with the particle energy. The luminosity for two colliding identical Gaussian bunches is [49]

$$\mathcal{L} = \frac{N^2 f}{4\pi\sigma_x\sigma_y}, \tag{1.3}$$

where N is the number of particles in a bunch, f the frequency of bunch collisions, and $\sigma_{x,y}$ the transverse root-mean-square (rms) beam size. The beam size is a function of the beta function* β and the geometric emittance† ϵ_G, with $\sigma = \sqrt{\beta\epsilon_G}$. The former describes the evolution of the transverse beam size along the beamline and is determined by the beamline. The latter is a measure of the beam quality, i.e., how tightly a bunch can be focused; in essence, the lower, the better. While the emittance of a bunch can be lowered through involved techniques, e.g., with a damping ring [50], usually care is taken to produce low-emittance bunches and not to spoil the emittance during the acceleration process and transport through the beamline. While this is routinely achieved in RF accelerators, it has so far not been shown in plasma accelerators. Failing to demonstrate this will bar plasma accelerators from collider facilities, as insufficient beam quality

*Described in more detail in Sec. 2.2.4.
†Described in more detail in Sec. 2.2.3.

would cause a drop in luminosity.

The figure of merit to describe the performance of FELs is the *brightness*, which is the particle flux per unit solid angle and area. It is defined with [51]

$$B = \frac{2I}{\pi^2 \epsilon_{Gx} \epsilon_{Gy}}, \tag{1.4}$$

with I as the bunch current and $\epsilon_{G,x/y}$ as the transverse geometric emittance. In its essence, it quantifies "how much monochromatic radiation power can be focused onto a tiny spot on the target" [52]. Again, similar to the luminosity in colliders, the performance is dependent on the beam quality.

1.5 Thesis Outline

This section gives a brief outline of the thesis structure.

Chapter 2 – Theory

The theory relevant to the subsequent chapters is described, including a definition of plasma and its most important parameters for plasma accelerators, as well as accelerator beam dynamics. The concept of plasma-wakefield acceleration, as well as its relevant properties and scalings, is introduced. As energy-transfer efficiency is the core topic of this thesis, the energy flow in a plasma accelerator is introduced, together with the definitions of efficiency.

Chapter 3 – Experimental facility

This chapter briefly introduces the experimental facility, describing the RF accelerator producing and delivering bunches and the subsequent plasma accelerator beamline. Then, the cell producing and containing the plasma is presented, showing a typical plasma density evolution.

Chapter 4 – Energy-extraction efficiency and beam-quality preservation

First, the limits on the overall performance of a plasma accelerator by insufficient energy-extraction efficiency are discussed, placing it as a key requirement together with beam-quality preservation. This is followed by experimental results demonstrating emittance preservation in a plasma accelerator with significant energy-extraction efficiency. As instabilities could limit higher efficiency, a novel diagnostic method that could measure the onset of such instabilities is discussed.

Chapter 5 – Driver-depletion efficiency

The evolution of a driving bunch through a plasma is simulated, introducing the depletion-limiting process of electron re-acceleration. This process is then shown experimentally and compared with predictions from theoretical models. To determine the depletion efficiency at this limit, the energy spectrum is reconstructed and corrected for various charge-loss processes, yielding an improved estimate of depletion. Finally, different strategies for higher driver-depletion efficiency are presented.

Chapter 6 – Summary, comparison to RF and outlook

This chapter provides an executive summary of the thesis and a selection of the literature's experimental and theoretical results concerning energy-transfer efficiency. The energy efficiency of plasma accelerators is then compared with that of collider concepts based exclusively on RF technology. The thesis finishes with a discussion on how to increase the overall energy-transfer efficiency of a plasma-accelerator stage by showing the interplay between different bunch and plasma parameters.

Chapter 2

Theory

This chapter explains the theory relevant to the experimental results presented in this thesis. Here, the concept of plasma and its relevant parameters for plasma accelerators are introduced. Later, as particle beams are used to drive plasma wakefields and are accelerated by them, several beam dynamics concepts are introduced. These include energy spread and emittance, which, for some applications, quantify the quality of a particle beam. As the beam–plasma interaction will be modeled in this thesis with particle-in-cell simulations to compare with experimental results, their working principle is introduced. Then, the concept of plasma-wakefield acceleration is introduced, first in the more intuitive linear regime and then in the blowout regime. The latter best describes the beam–plasma interactions presented in this thesis and allows for beam-quality preservation. Approximations in this regime based on a heuristic model are then presented, as they will be used later to compare to the experimental results presented. The chapter finishes with a description of the energy transfers within a plasma accelerator and defines the corresponding efficiencies.

2.1 Definition of plasma

"A plasma is a quasineutral gas of charged and neutral particles which exhibits collective behavior" [53, p. 2]. The quasineutrality refers to a similar amount of positive and negative charges. The collective behavior arises from the Coulomb force, with its long-range potential decaying in distance with $1/r$, which allows local disturbances to affect remote regions of the plasma [54].

There are different ways to produce plasma, one of which is photoionization by electromagnetic radiation. This can be done with an intense laser pulse, which can, among others, lead to multiphoton or optical field ionization [55–58]. A different method is collisional ionization, where fast particles, such as from a discharge current, collide with atoms and ionize them. Following Paschen's law [59], such current can be achieved by sustaining a large voltage around a gas capillary [60, 61]. Here, free electrons are accelerated and start an avalanche that ionizes the gas. This is the technique used for the results presented in this thesis.

The most important plasma parameter for plasma accelerators is its *number density*, i.e., the number of charged particles per volume. For a quasi-neutral plasma, this is the same in both species, i.e., $n_e \approx Z n_i$, where the subscripts $_e$ and $_i$ stand for plasma electron and ion density, respectively, and Z stands for the charge state of the ions. If one were to slightly displace the electrons and ions in a plasma and then release them, they would oscillate at the electron and ion plasma frequencies, which define the characteristic timescales on which a particle species reacts to external fields. The *plasma frequency* for ions and electrons is given by

$$\omega_{p,e/i} = \sqrt{\frac{n_{p,e/i} e^2}{m_{e/i} \epsilon_0}}, \tag{2.1}$$

with the electron/ion mass $m_{e/i}$, the elementary charge e and the vacuum permittivity ϵ_0. Because of the mass difference of the two species, the electrons react faster to external

forces than the ions.

In this thesis, for better readability, when referring to plasma parameters such as density or frequency, that of the plasma electrons and not ions is meant, and denoted with the subscript $_p$.

The characteristic length of plasma perturbations can be approximated with the so-called plasma *skin depth*, i.e., the inverse of the angular wavenumber,

$$k_p^{-1} = \frac{c}{\omega_p} = \sqrt{\frac{m_e \epsilon_0 c^2}{n_p e^2}}, \tag{2.2}$$

where c is the speed of light in vacuum. Closely related to this is the *plasma wavelength*, which is the wavelength at which the plasma electrons oscillate, with

$$\lambda_p = \frac{2\pi}{k_p}. \tag{2.3}$$

As an example, for a plasma density of 1×10^{16} cm^{-3}, the plasma electron frequency is 5.6 THz, the skin depth is 53 µm, the wavenumber is 1.9×10^4 m^{-1}, and the wavelength is 334 µm.

2.2 Particle-beam dynamics

The motion of a charged particle in an electric and a magnetic field is described by the Lorentz force

$$\vec{F} = \frac{d\vec{p}}{dt} = q(\vec{E} + \vec{v} \times \vec{B}), \tag{2.4}$$

where q, $\vec{v}$ and p are the charge, velocity and momentum of the particle, respectively, $\frac{d}{dt}$ is the derivative in time, and $\vec{E}$ and $\vec{B}$ are the electric and magnetic fields. While an electric field can impart a force parallel to the particle's propagation, the cross-product implies that the force resulting from a magnetic field is perpendicular. In addition, the force resulting from a magnetic field is scaled with the particle's velocity, which

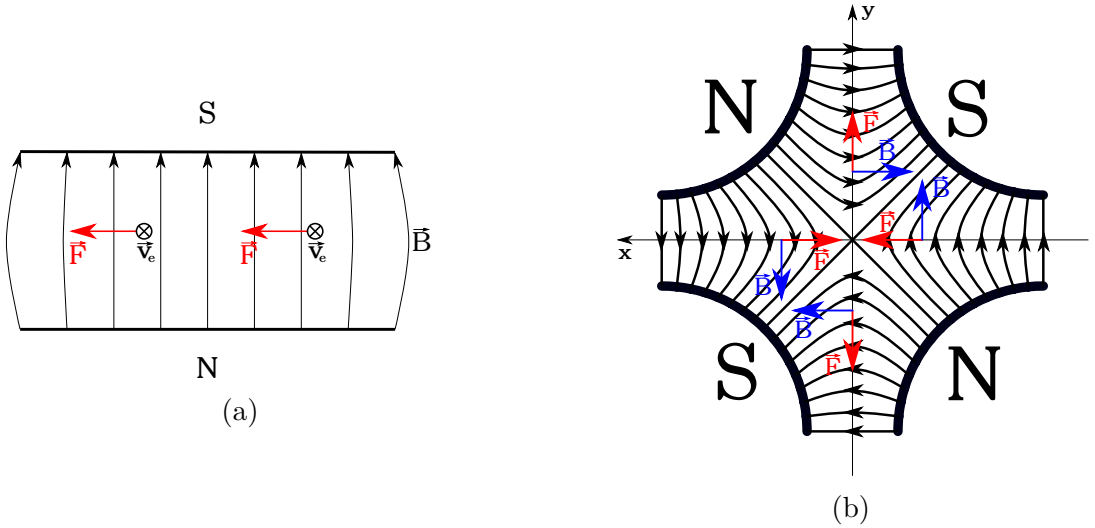

Figure 2.1: The force of a dipole (a) and quadrupole (b) magnetic field on an electron moving into the plane of the page at different locations within the fields. The opposite forces can be achieved when switching the polarities of the magnet. Image from Ref. [62].

approaches c when relativistic. This makes a moderate magnetic field equivalent to a very strong electric field (1 T $\approx$ 300 MV/m). As a result, electric fields are used for the acceleration of particles in an accelerator, and magnetic fields for steering and focusing. Fig. 2.1 illustrates the force acting on a negatively charged particle traversing a magnetic dipole (a) and quadrupole (b). In the dipole field, the force has the same strength and direction regardless of a particle's position: these are used for steering a particle bunch. In contrast, in the quadrupole field, while the strength increases linearly from the center, the force is opposite in the vertical and horizontal axis. By convention, the quadrupole magnet focusing in the horizontal plane is called the focusing quadrupole magnet, and the converse is the defocusing quadrupole magnet. To achieve net focusing of a bunch in both transverse planes, so-called FODO (focusing-nothing-defocusing-nothing) lattices are used, where the polarity of quadrupole fields is alternated.

While the trajectory of individual particles can be calculated with Eq. 2.4, accelerators usually work with large numbers of particles (beyond millions), where it is not feasible to treat all particles individually. A collection of particles clustered together and moving in a similar direction is called a *particle bunch*. Depending on the goal, it is common to

either treat a particle bunch as an average single particle or as an ensemble with its collective behavior described by a set of parameters. In the following, the parameters required to understand the results presented in this thesis are introduced. A more detailed description can be found in Ref. [63].

2.2.1 Energy, momentum and velocity of a particle

The total energy of a particle is the sum of the kinetic E_{kin} and the rest E_0 energy, with

$$E = \gamma m_0 c = E_{\text{kin}} + E_0, \tag{2.5}$$

with the Lorentz factor $\gamma = (1 - \frac{v^2}{c^2})^{-1/2}$, the electron rest mass $m_0 \approx 0.511$ keV, $E_0 = m_0 c^2$, and $E_{\text{kin}} = (\gamma - 1) m_0 c^2$. The momentum is defined as

$$p = \gamma m_0 v = \gamma m_0 c \beta_{\text{rel}}, \tag{2.6}$$

with $\beta_{\text{rel}} = v/c$. Relativistic particles have $\gamma \gg 1$, and, as $v = c(1 - 1/\gamma)^{-1/2}$, their velocity is approximately c, and $\beta_{\text{rel}} \approx 1$. During acceleration or deceleration, their velocity is approximately constant, and rather E_{kin} is changed. Therefore, for relativistic particles, usually their kinetic energy is quoted instead of their velocity, and, as the rest energy is negligible in comparison, it is simply referred to as energy.

2.2.2 Energy spread and chromaticity

Recalling Eq. 2.4, for a fixed field, the trajectory of particles with different momenta will vary*, as illustrated in Fig. 2.2. While ideally, all the particles of a bunch have identical energies, in reality, this is practically not achievable. Therefore, different parts of a bunch will be focused differently based on the particles' momenta. This effect is

*This becomes clear if, for the transverse axis x, the momentum p_x is approximated with αp_z, where α is the bending angle, and $p \approx p_z$.

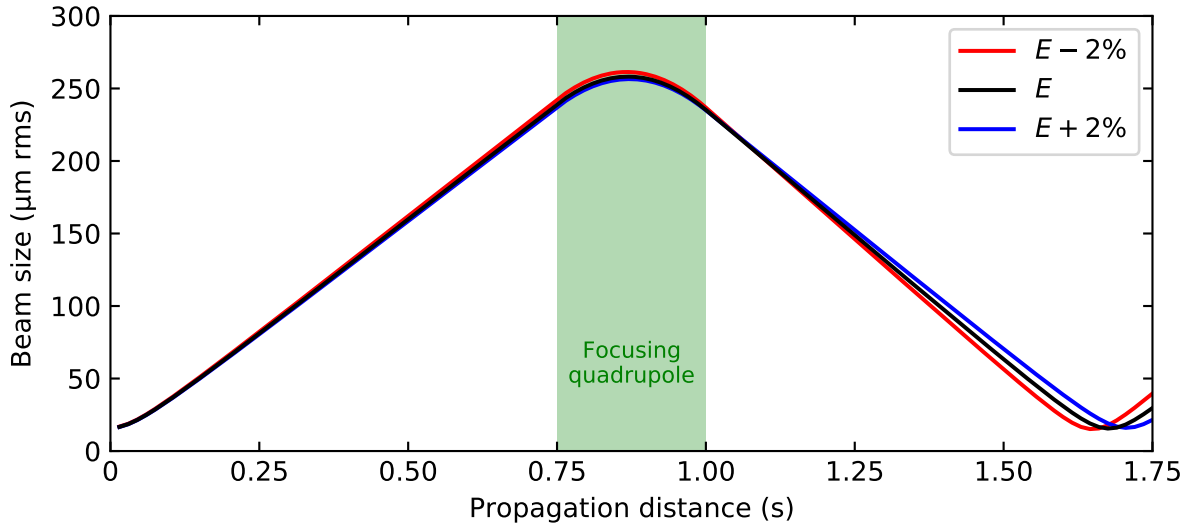

Figure 2.2: Transverse beam size evolution along a beamline consisting of a drift, a focusing quadrupole, and a second drift. Only the beam size in the focusing plane is shown. The black line shows the bunch with the design energy E, and the red and blue lines with a 2% lower and higher energy, respectively. The waist location downstream of the quadrupole varies in energy, and, at the waist of the design energy, the effective beam size is larger.

called *chromaticity* [64, 65]. How problematic this becomes for the accelerator is mainly determined by how similar in energy the particles are. This is quantified by σ_δ, the rms of the relative energy spread, with

$$\delta = \frac{\Delta E}{E}, \tag{2.7}$$

where ΔE is the difference of a particle's energy with the average energy E.

Different processes can impose limits on the accepted energy spread for an accelerator. In the case of FELs, for the emission of coherent radiation, the energy spread is usually at or below 0.1% [19, 66]. For colliders, a small transverse beam size at the interaction point is required. The chromaticity of the final focusing system will, as depicted in Fig. 2.2, increase the effective beam size at the focus as a function of the energy spread [67]. To mitigate this effect, the energy spread is typically 0.1–1% [31, 32, 67].

2.2.3 Emittance

Emittance is a measure of transverse beam quality [51]. The rms geometric emittance in x (and equivalently in y) is defined with [68, 69]

$$\epsilon_{G,x,\mathrm{rms}} = \sqrt{\langle x^2 \rangle \langle x'^2 \rangle - \langle x x' \rangle^2}, \tag{2.8}$$

where x and x' are a particle's position and angle, respectively. $\langle\ \rangle$ denotes the second central moment of the beam particle distribution, defined with

$$\begin{aligned}
\langle x^2 \rangle &= \frac{\sum_i^n x_i^2}{n} - \left(\frac{\sum_i^n x_i}{n} \right)^2, \\
\langle x'^2 \rangle &= \frac{\sum_i^n x_i'^2}{n} - \left(\frac{\sum_i^n x_i'}{n} \right)^2, \\
\langle x x' \rangle &= \frac{\sum_i^n x_i x_i'}{n} - \left(\frac{\sum_i^n x_i \sum_i^n x_i'}{n^2} \right)^2,
\end{aligned}$$

where i iterates over all n particles.

As illustrated in Fig. 2.3 for a Gaussian beam, the rms geometric emittance represents

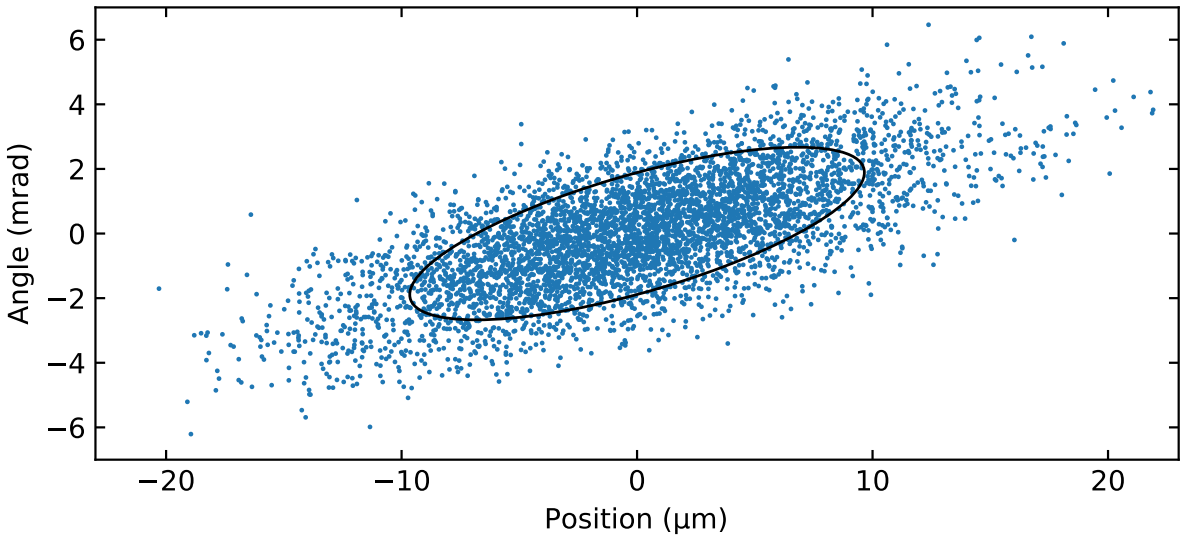

Figure 2.3: Transverse trace space distribution of a beam, where each point corresponds to a particle's position and angle. The ellipse shows the covariance of the trace-space, and its area is the rms geometric emittance.

the area of its rms ellipse in trace space. When a bunch is accelerated, the longitudinal momenta of the particles increase, while the transverse momenta p_x and p_y are kept constant, shrinking the divergence angle ($x' \approx p_x/p_z$). This decreases the emittance as defined in Eq. 2.8, in a process named *adiabatic damping* [70]. While the definition above might be more intuitive, it is useful to use the phase space instead (x–p_x), whose area is invariant under acceleration. This normalized rms emittance is defined by

$$\epsilon_{N,x,\mathrm{rms}} = \frac{1}{mc}\sqrt{\langle x^2\rangle\langle p_x^2\rangle - \langle x p_x\rangle^2}, \tag{2.9}$$

with p_x as the particle's momentum in x and m its mass. These two emittances are related by [70]

$$\epsilon_{N,x,\mathrm{rms}} = \gamma\beta_{\mathrm{rel}}\epsilon_{G,x,\mathrm{rms}}, \tag{2.10}$$

Following Liouville's theorem, which states that the phase space density is constant under linear transformations, i.e. if there are no nonlinear forces or coupling forces between different planes, the normalized emittance is constant in an accelerator* [51]. For the remainder of the thesis, emittance refers to the normalized emittance unless stated otherwise.

2.2.4 Beta function

In vacuum and only with conservative forces, the geometric emittance is the constant that tells us how tightly a beam can be focused, and the beta function describes the evolving transverse beam size $\sigma(s)$ with

$$\sigma(s) = \sqrt{\epsilon_G\beta(s)}, \tag{2.11}$$

*Here, manipulations exchanging the emittance between different planes are excluded, i.e., so-called emittance exchange schemes [71], as manipulations are usually performed on one plane at a time. Still, in such cases, the 6D phase-space volume is preserved following Liouville's theorem.

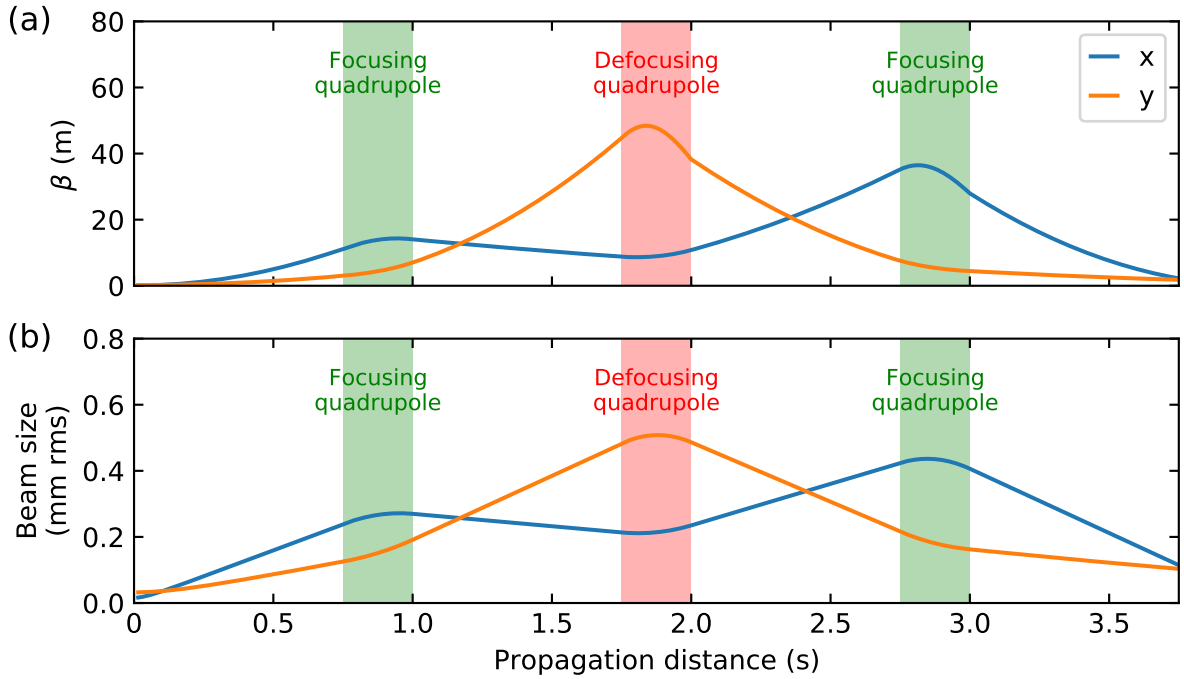

Figure 2.4: The beta function (a) and transverse beam size (b) along a simplified beamline, consisting of a concatenation of quadrupole magnets connected by drift sections.

where s is the position along the accelerator beamline. In other words, it describes the radial offset away from the centroid of a particle along the beamline, and it is determined by the beamline optics. The evolution of the beta function and beam size along a simplified beamline is illustrated in Fig. 2.4.

Around the waist/focus of a beam and in a vacuum without magnetic fields, the beta function follows [63, Sec. 3.10]

$$\beta(s) = \beta_0 + \frac{(s - s_0)^2}{\beta_0}, \tag{2.12}$$

where β_0 and s_0 are the waist beta function and waist location, respectively. Together with Eq. 2.11, the transverse beam size around a waist can be described with

$$\sigma(s) = \sqrt{\epsilon_G \left(\beta_0 + \frac{(s - s_0)^2}{\beta_0} \right)}. \tag{2.13}$$

Also at the waist, the geometric emittance and the waist beta function determine the

divergence of the beam, with

$$\sigma' = \sqrt{\frac{\epsilon_G}{\beta_0}}. \tag{2.14}$$

As will be shown later in Sec. 2.4.2, in a plasma accelerator, the bunches are accelerated within a focusing channel, centered at the propagation axis, with a strength

$$k = \frac{k_p^2}{2\gamma}. \tag{2.15}$$

This leads to the particles oscillating transversely and to a beam envelope oscillation at the betatron frequency $\omega_\beta = \frac{c}{\beta_m}$ [72], with the matched beta function defined as

$$\beta_m = \frac{1}{k} = \frac{\sqrt{2\gamma}}{k_p}. \tag{2.16}$$

This oscillation, caused by *beam mismatch* [72, 73], rotates the beam ellipse in the transverse phase space. As the frequency is energy-dependent, any energy spread will have different energy slices in a bunch rotating at different rates, leading to *betatron decoherence* and growth in the projected emittance [74, 75]. As the focusing force is constant, so is the average beam-envelope size. Then, with an increasing emittance, following Eq. 2.11*, the beta function decreases until the beam is matched: the focusing force is balanced with the diverging beam, and the decoherence has saturated. This occurs at a distance $L_{\text{decoh}} = \beta_m/\sigma_\delta$ [75]. Decoherence can be avoided by focusing the beam into the plasma such that the beam is matched from the start. This is the case when the waist beta function is equal to the matched beta function defined with Eq. 2.16, with the waist located at the start of the plasma column. As an example, for a bunch with 1 GeV and a plasma density of 1×10^{16} cm^{-3}, this corresponds to $\beta_m = 3.3$ mm. For comparison, in the collider design of CLIC, the horizontal and vertical beta function at the interaction point is 6.9 and 0.068 mm, respectively [27, Table A.4].

*This equation uses the geometric emittance, but the geometric and normalized emittance are connected with Eq. 2.10.

2.2.5 Matrix formalism

This section briefly introduces transfer matrices, which can be used to model analytically the propagation of beam particles through a beamline. This will be used later in Sec. 5.2 to identify particles that reach the vacuum-pipe wall and are lost in transport between the plasma and the diagnostic.

The transverse offset from the design orbit of a charged particle can be described with Hill's differential Eq. [70, ch. 5.5]:

$$x'' + K(s)x = 0, \tag{2.17}$$

where $K(s)$ describes the transverse forces along the beamline position s. It is not possible to solve Eq. 2.17 analytically in a general way for an arbitrary distribution of magnetic elements, and numerical solutions are required instead. However, one can compute the principal solutions for individual magnets or drifts, and, together with the particle's initial position and angle (x_0, x_0'), compute the outcoming position and angle (x, x'). Repeating this for every magnetic or drift element allows for reconstructing the trajectory throughout the beamline. Eq. 2.18 shows this procedure for the beamline in Fig. 2.4.

$$\begin{pmatrix} x \\ x' \end{pmatrix} = M_{\text{drift}_4} \cdot M_{\text{foc}} \cdot M_{\text{drift}_3} \cdot M_{\text{def}} \cdot M_{\text{drift}_2} \cdot M_{\text{foc}} \cdot M_{\text{drift}_1} \cdot \begin{pmatrix} x_0 \\ x_0' \end{pmatrix} = M_{\text{tr}} \cdot \begin{pmatrix} x_0 \\ x_0' \end{pmatrix}, \tag{2.18}$$

where M_{tr} is the transfer matrix for the whole beamline and equal to the product of the individual matrices. Assuming no coupling between the horizontal and vertical plane, the transfer matrix in a transverse plane for a drift section can be written as [76]

$$M_{\text{drift}_1} = \begin{pmatrix} 1 & l \\ 0 & 1 \end{pmatrix},$$

and respectively for a focusing and defocusing magnet

$$M_{\text{foc}} = \begin{pmatrix} \cos(\Omega) & \frac{1}{\sqrt{|k|}}\sin(\Omega) \\ -\sqrt{|k|}\sin(\Omega) & \cos(\Omega) \end{pmatrix}$$
$$M_{\text{def}} = \begin{pmatrix} \cosh(\Omega) & \frac{1}{\sqrt{|k|}}\sinh(\Omega) \\ \sqrt{|k|}\sinh(\Omega) & \cosh(\Omega) \end{pmatrix},$$

where $\Omega = \sqrt{k}l$, with the beamline-element length l and the focusing strength $k = qg/p$. q is the particle charge, $g = \frac{\partial B}{\partial r}$ the radial magnetic field gradient, and p the particle's momentum.

When transporting a beam to a diagnostic for, e.g., measuring the transverse beam size, it is important to ensure that the position of the particles on the screen is not dependent on the initial angle of the particles, i.e., *point-to-point* imaging. This is also important for measuring energy spectra, as, in spectrometers, the particle's energy is measured with its position on the screen. Assuming no coupling between the transverse planes and using

$$\begin{pmatrix} x \\ x' \\ y \\ y' \end{pmatrix} = \begin{pmatrix} M_{11} & M_{12} & 0 & 0 \\ M_{21} & M_{22} & 0 & 0 \\ 0 & 0 & M_{33} & M_{34} \\ 0 & 0 & M_{43} & M_{44} \end{pmatrix} \cdot \begin{pmatrix} x_0 \\ x'_0 \\ y_0 \\ y'_0 \end{pmatrix},$$

the particle's position in the two transverse axes is

$$x = M_{11}x_0 + M_{12}x'_0$$
$$y = M_{33}y_0 + M_{34}y'_0.$$

Therefore, to achieve point-to-point imaging, the element M_{12} must be zero such that initial angle x'_0 has no effect on the final position x, and similarly for M_{34} in the other plane. As these matrix elements depend on the particle's momentum, the further it

is from the design momentum, the larger the impact of its angle at the object plane on its position in the image plane. The momentum where the point-to-point imaging conditions are fulfilled is called *imaging energy*.

2.3 Particle-in-cell simulations

Simulation codes for plasma-wakefield acceleration rely largely, with some exceptions [77, 78], on the particle-in-cell (PIC) [79] method. Here, plasma and beam particles can move within the simulation boundaries, with their movement dictated by the Lorentz law and the electric and magnetic fields, where the currents, charge densities, and fields are represented on a spatial grid. To lower the computational cost, instead of simulating all the particles involved in the interaction, fewer so-called macro-particles are used, each representing an ensemble of physical particles.

A PIC simulation starts by initializing the simulation domain, e.g., the spatial grid, and the number of macro-particles, with their positions and velocities. Then, with a simulation domain co-moving at the speed of the wakefield driver, which avoids simulating the full plasma column at once, the simulation code loops over the following points for each simulation step:

1. The motion of individual plasma and beam particles is calculated. Each particle's trajectory is determined by the equation of motion, using the forces from electric and magnetic fields acting on each particle.

2. The current and charge density distributions are computed. For this, the new positions of the beam and plasma particles are used.

3. The fields are calculated in the simulation space. Maxwell's equations are solved to determine the electric and magnetic fields on a discrete grid based on the current and charge density distributions.

4. The forces acting on all the particles are computed based on the electric and magnetic fields.

The simulation grid has to be fine enough to resolve the plasma response. As an example, for a plasma density of 1×10^{16} cm^{-3}, the cell grid resolution should be well below $1/k_p \approx 53$ µm. If the motion of the plasma electrons is to be resolved sufficiently, the time steps must be smaller than their oscillation period. Again, for a plasma density of 1×10^{16} cm^{-3}, the simulation steps should be

$$t_{\text{step}} = \frac{2\pi}{\omega_p N} \approx \frac{1}{N} \text{ ps} \qquad \text{or} \qquad d_{\text{step}} = \frac{2\pi c}{\omega_p N} \approx \frac{300}{N} \text{ µm}, \tag{2.19}$$

where N is the number of samples within an oscillation. Often, the simulation domains have dimensions of a millimeter, and the plasma columns are tens of millimeters. Combined with the micrometer-resolved grids and micrometer-sized simulation steps, PIC codes can become computationally expensive. This is especially the case for the simulations performed for this thesis, which use plasma columns of 200 mm.

To lower computational costs, the three-dimensional PIC code HiPACE++ [80] makes use of the quasi-static approximation [81–83], which, in its essence, uses the disparity in time scales between the motion of plasma electrons and the beam particles. The beam evolves on the time scale of its betatron wavelength $\lambda_\beta \approx \sqrt{2\gamma}\lambda_p$ [84], and can be considered frozen when calculating the plasma response. As an example, for an electron bunch with 5 GeV and $\gamma \approx 10000$, the betatron wavelength is ~ 140 larger than the plasma response, and thus the timesteps can be 140 times longer. The quasistatic approximation only holds for bunches with relativistic electrons ($\gamma \gg 1$).

2.4 Plasma-wakefield acceleration

If a negatively charged bunch traverses a plasma, its charge exerts a repelling force on the plasma electrons, causing them to move outward and leaving behind a region of

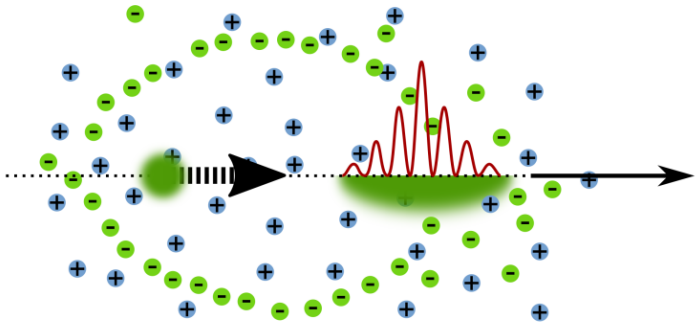

Figure 2.5: Schematic of the wakefield structure driven by a laser pulse or negatively-charged particle bunch propagating towards the right. The plasma electrons (green circles) are expelled radially outward, while the plasma ions (blue circles) are often assumed immobile. Placing a second bunch in the cavity-like structure allows for simultaneous focusing and acceleration. Adapted illustration from P. González Caminal.

positive charge density from the ions. In the framework of this thesis, the ions can be assumed immobile, as their movement is slower compared to that of the electrons (see Sec. 2.1). If the charge density of the bunch is large enough, all plasma electrons are expelled, as illustrated in Fig. 2.5. As the bunch advances, the positive charge from the ions attracts the expelled electrons back to the axis. In the wake of the *driving* bunch, there exists a region with strong electric fields, which can be used to accelerate and focus a *trailing bunch* (often called the *witness bunch*). Such wakefields can also be produced by a laser pulse [85, 86] or a positively charged bunch [87, 88]. In the case of a laser pulse, i.e., laser-driven plasma-wakefield acceleration (LWFA), the electrons are expelled by the ponderomotive force [89]. If the driver is a particle bunch, it is generally called beam-driven plasma-wakefield acceleration (PWFA). For a positively charged bunch, the plasma electrons are first attracted and, after its passing, repelled by their own collective excess negative charge on the axis, resulting in a shift in phase of the focusing and accelerating fields [87, 90]. The theory introduced hereafter is centered on electron beam drivers, as these were used for the experimental results presented in this thesis.

The drive bunch radial size σ_r, length σ_z, and the bunch and plasma densities

determine how the wakefields are driven. The transverse extent of the bunch should be of the order of or smaller than the characteristic length at which the plasma reacts to perturbations: $k_p\sigma_r < 1$ [91]. Otherwise, the filamentation instability can develop, where subregions of the beam (with a length scale of $1/k_p$) drive independent wakefields [92–94]. If the bunch is too long, there is sufficient time for the plasma to cancel the charge imbalance and no wake is driven coherently. Therefore, the driver should be short enough, fulfilling $k_p\sigma_z \lesssim \sqrt{2}$ [91]. If these conditions are fulfilled, then the bunch peak density n_b and the plasma density determine how strongly the plasma electrons are expelled, which dictates in which regime the wakefields are driven. Two of these regimes are introduced in the following sections, and then considerations on energy-transfer efficiency are introduced.

2.4.1 Linear regime

The linear regime assumes a small density perturbation ($n_b/n_p \ll 1$) driven by the bunch. Following derivations in Refs. [95, 96], the equations describing the wakefields in 2D cylindrical geometry (r,z) are introduced. The small-perturbation plasma response δn for a beam propagating to positive z can be described with

$$\delta n(z,r) = -k_p \int_z^\infty n_b(z',r)\sin(k_p(z-z'))\,dz', \tag{2.20}$$

where $n_b(z',r)$ describes the beam density. We note that the perturbation at z is an integral from z to $+\infty$, i.e., it is only dependent on the preceding beam charge. Also, after the passing of the beam, the oscillation is sinusoidal.

The longitudinal and transverse wakefields can be described with:

$$E_z(r,z) = \frac{e}{\epsilon_0}\int_0^\infty \frac{\partial\delta n(r',z)}{\partial z} K_0(k_p r_>)I_0(k_p r_<)r'dr' \tag{2.21}$$

$$E_r(r,z) = -\frac{e}{\epsilon_0}\int_0^\infty \frac{\partial\delta n(r',z)}{\partial r'} K_1(k_p r_>)I_1(k_p r_<)r'dr', \tag{2.22}$$

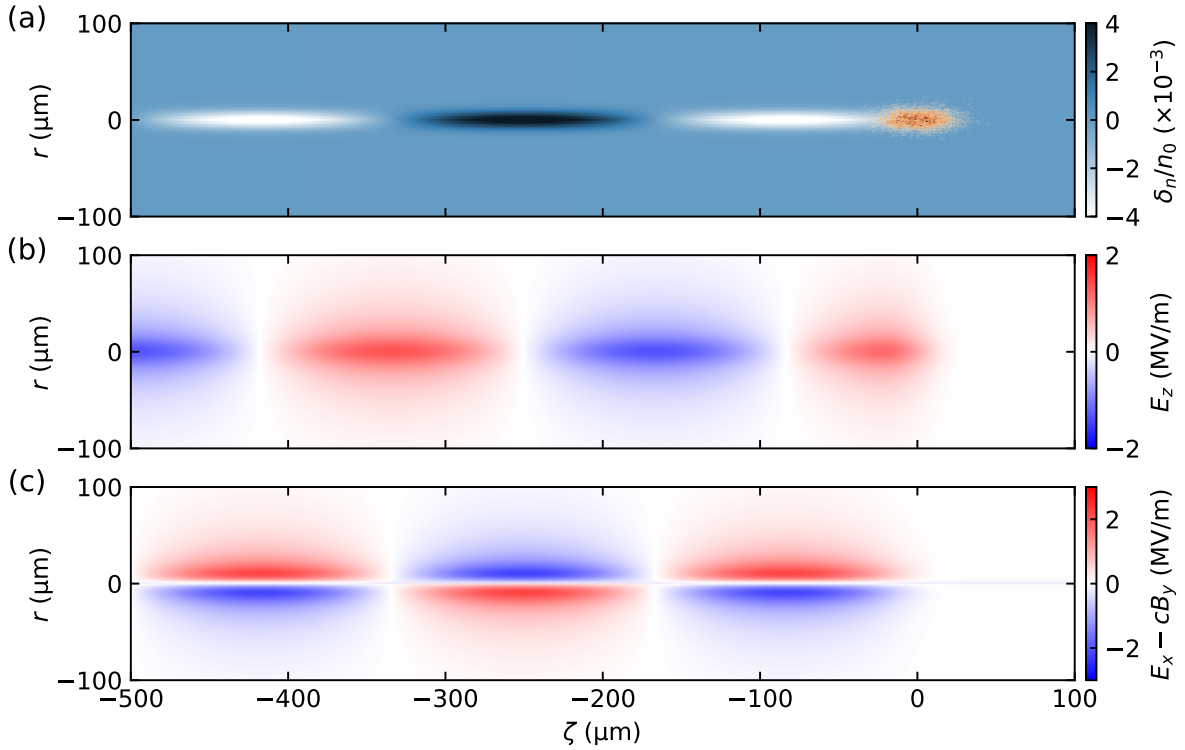

Figure 2.6: (a) Perturbation of the plasma density (1×10^{16} cm^{-3}) by a Gaussian electron bunch with a peak density of 8×10^{13} cm^{-3}, with the corresponding longitudinal (b) and transverse (c) fields. The bunch propagates towards the right. Image Ref. [98].

where $r_>$ denotes the maximum of r', and $r_<$ the minimum of r [95, p. 254]. I_n and K_n are the nth order modified Bessel functions of the first and second kind, respectively.

While the linear regime can be used to accelerate charged particles, there are significant drawbacks. First, as can be seen in Eq. 2.21 and Fig. 2.6(b), at a fixed longitudinal position, the accelerating field varies in the transverse axis. This imprints an energy spread on the accelerated bunch. Second, as is shown in Fig. 2.6(c), the focusing field is not linear, which is required to preserve the emittance of a beam, following Liouville's theorem [70, 97]. These problems mentioned can be avoided in the blowout regime.

2.4.2 Non-linear (or blowout) regime

For driver densities beyond the plasma density ($n_b/n_p \gg 1$), the repelling force of the driver is strong enough to expel all plasma electrons: these are 'blown out' and only a plasma-ion column remains in the wake. If the motion of the uniform ions can be neglected, they provide a transversely linear focusing force [see Fig. 2.7(c)], which can in principle preserve the emittance of an accelerating bunch.

In this regime, the fluid picture is not valid, because, at the front and back of the blowout bubble, the trajectories of the plasma electrons cross [99, 100]. Instead, the models derived by Lu *et al.* [99] and Golovanov *et al.* [101] use the kinetic picture. While that of Golovanov *et al.* is more complete, it is also more complicated. From here on, key concepts and scalings derived in the model from Lu *et al.* are discussed, as they sufficiently describe the experimental results presented in this thesis. Following Ref. [99], the key idea is that the wake can be described entirely by the trajectory of the blowout radius $r_b(\zeta)$, with $\zeta = z - ct$ as the co-moving longitudinal variable. The plasma density and current profile are divided into three distinct regions: an ion channel, with $r < r_b(\zeta)$; a narrow sheath of the expelled plasma electrons, with $r_b < r < r_b + L$ and $L \ll r_b$; and a region with a linear response that produces weak fields. Also, the plasma is considered at rest or cold, as the thermal velocity of the electrons is small compared to the wakefield phase velocity c. Further, using the fact that the driver evolves on a time scale much longer than the plasma response, the quasistatic assumption is made: the driver changes little while it passes by a plasma particle.

For the remainder of this chapter, the length is normalized to k_p^{-1}, the charge to e, and the beam density to n_p.

In the ultra-relativistic blowout regime, where the maximum blowout radius $R_b \gg k_p^{-1}$, the trajectory of the innermost electrons $r_b(\zeta)$ can be described with

$$r_b \frac{d^2 r_b}{d\zeta^2} + 2\left(\frac{dr_b}{d\zeta}\right)^2 + 1 = \frac{4\lambda(\zeta)}{r_b^2}. \tag{2.23}$$

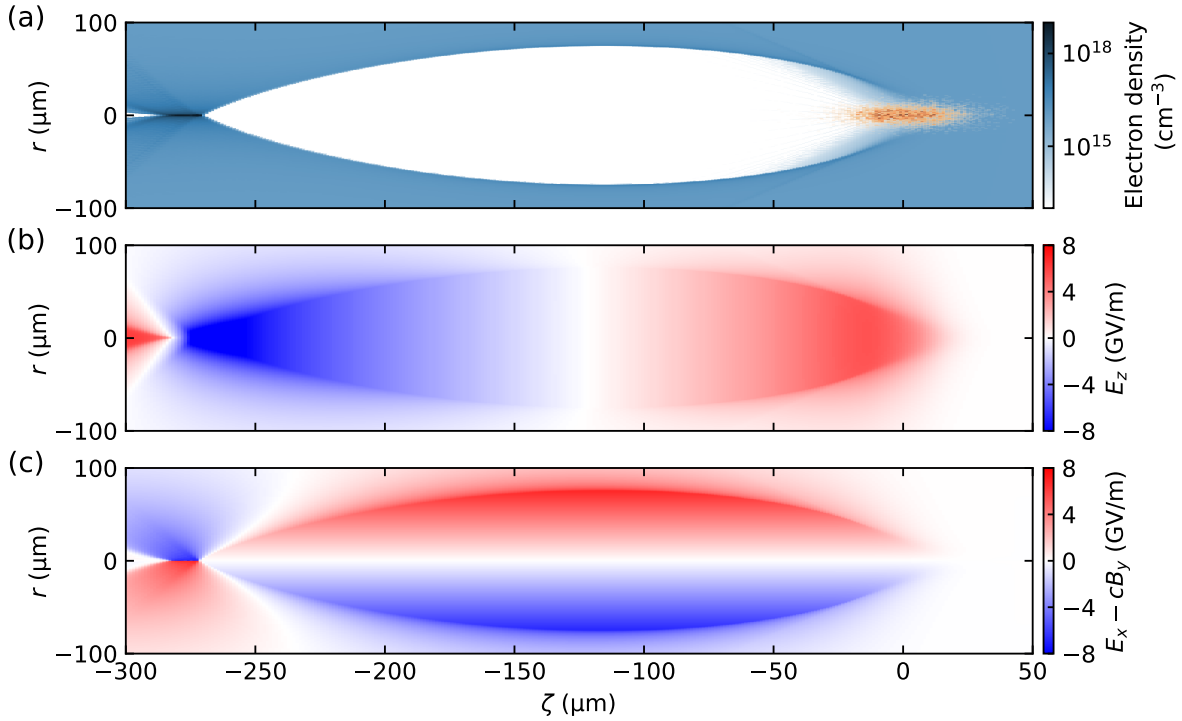

Figure 2.7: Plasma wakefields for a Gaussian electron bunch with a peak density of 9.6×10^{17} cm^{-3} propagating towards the right, where the background plasma electron density is 1×10^{16} cm^{-3}. The corresponding longitudinal and transverse fields are shown in (b) and (c), respectively. Image Ref. [98].

The normalized current profile of the drive beam $\lambda(\zeta)$ is given by

$$\lambda(\zeta) = \int_0^{r \gg \sigma_r} n_b(\zeta) r' dr',$$

where σ_r is the transverse beam size. Continuing from Ref. [99], the longitudinal and transverse wakefields can be described with

$$E_z = \frac{k_p E_0}{2} r_b(\zeta) \frac{dr_b(\zeta)}{d\zeta} \tag{2.24}$$

$$E_r - cB_\theta = \frac{k_p r}{2} E_0, \tag{2.25}$$

where the subscripts $_r$ and $_\theta$ stand for the radius and azimuthal angle, respectively, and

E_0 is the field at the (cold nonrelativistic) wave-breaking limit [102], with

$$E_0 = \frac{m_e c \omega_p}{e} = \sqrt{\frac{m_e c^2 n_0}{\epsilon_0}}. \tag{2.26}$$

From Eq. 2.25 it should be noted that the focusing field is independent of ζ and scales linearly with r. Following the Panofsky-Wenzel theorem [103], which states that the longitudinal gradient of the transverse electromagnetic field is proportional to the transverse gradient of the longitudinal field, i.e. $d(E_r - cB_\theta)/dz = \nabla_\perp E_z$, the longitudinal field, for a fixed ζ, should be uniform in r. This can be seen in Fig. 2.7(b), where E_z is independent of r. In conclusion, a trailing electron bunch will experience a transversely linear focusing force and a longitudinally varying accelerating field. The former allows for emittance preservation, and the latter poses a challenge, as trailing electrons are accelerated unevenly, imprinting a longitudinally correlated energy spread. However, as the accelerating field is a function of the blowout radius (see Eq. 2.24), and the blowout radius is a function of the beam current profile (see Eq. 2.23), the current of the trailing bunch will also affect the accelerating field. This effect, called *beam loading*, is illustrated in Fig. 2.8. When the current of the trailing bunch is shaped such that the accelerating field it experiences is uniform, all electrons are accelerated at the same rate, and the energy spread is preserved [100]. Such *optimal beam loading* occurs with a trapezoidal-shaped current and was successfully demonstrated experimentally, where the field was flattened down to 2.8% rms [104].

Often, and usually driven by incomplete knowledge of the experimental parameters, simple and heuristic approximations are useful as guidance when performing an experiment or comparing results with theory. As an example, the wave-breaking field defined in Eq. 2.26 can be used as a rough estimate of the accelerating strength at a given plasma density, with $E_z[\mathrm{V/m}] \approx 96\sqrt{n_p[\mathrm{cm}^{-3}]}$. At a density of 1×10^{16} cm^{-3} one can expect a maximum accelerating gradient on the order of 10 GV/m. More accurately, following Ref. [99] and assuming a small maximum blowout radius ($R_b \approx 1/k_p$), the

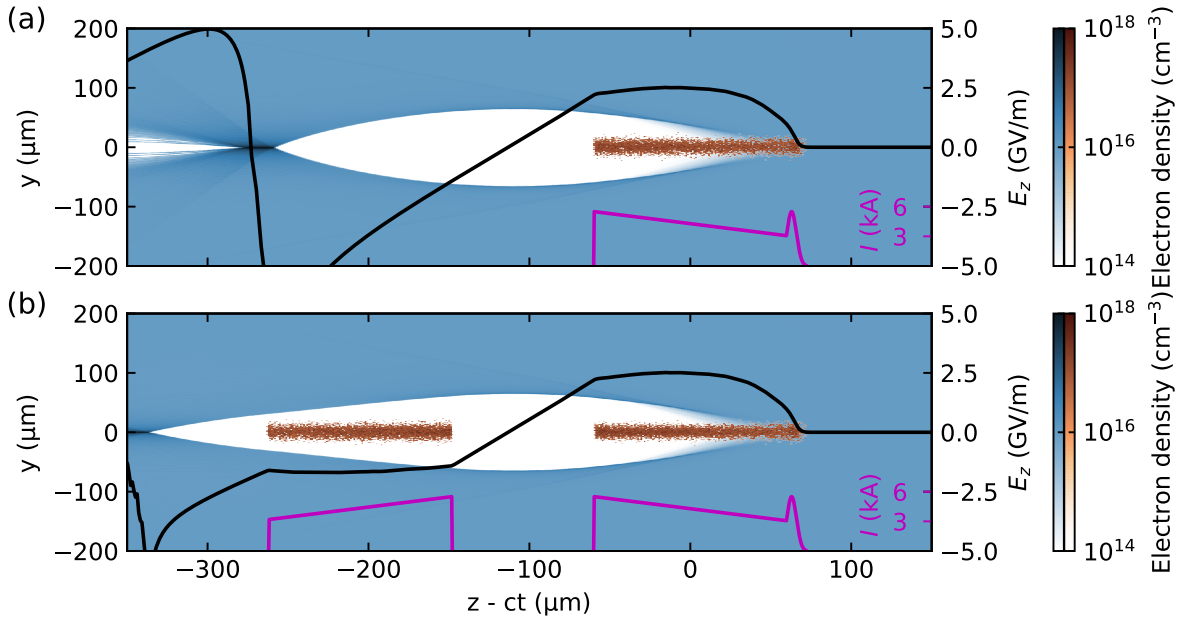

Figure 2.8: Plasma (blue) and bunch (orange) electron densities for only a drive bunch (a) and for a driver-witness pair (b). The solid black and magenta lines show the longitudinal electric field and bunch current, respectively. The blowout bubble is elongated with the beam loading shown in (b), and the accelerating field is approximately flat. Image Ref. [98].

maximum longitudinal wakefield is

$$E_{z,\,\max} = \Lambda \ln\left(\frac{1}{\sqrt{\Lambda/5.3}}\right) E_0, \tag{2.27}$$

with the normalized charge per unit length Λ defined as [99]

$$\Lambda \equiv \frac{n_b}{n_p}\sigma_r^2 k_p^2, \tag{2.28}$$

where n_b is the peak bunch density and σ_r the transverse bunch size. For a bi-Gaussian bunch, where the peak current $I_b = n_b 2\pi\sigma_r^2 ec$, and using the Alfvén current $I_{\text{Alfvén}} = 4\pi\epsilon_0 m_e c^3/e \approx 17$ kA, Eq. 2.28 can then be rewritten as

$$\Lambda = 2\frac{I_b}{I_A}. \tag{2.29}$$

The maximum blowout radius can be approximated with [99]

$$R_b \approx 2.58\Lambda^{1/2}. \tag{2.30}$$

2.4.3 Energy transfer in plasma accelerators

The maximum energy that could be transferred from a driver to a trailing bunch is the driver's initial total energy $E_{d_0}Q_{d_0}$, where E_{d_0} is the average particle energy and Q_{d_0} is the bunch charge. For this, first, the energy of the driver has to be transferred to the plasma, and, second, extracted by the trailing bunch, as depicted in Fig. 2.9.

The *driver-to-plasma* energy-transfer efficiency, also named energy-deposition or driver-depletion efficiency, is defined by the ratio of the deposited to the initial driver energy, i.e.,

$$\eta_{d\to p} \equiv \frac{\Delta E_d\, Q_d}{E_{d_0}\, Q_{d_0}}, \tag{2.31}$$

where E_d and Q_d are the driver's average particle energy and charge after the beam–plasma interaction, respectively. Given a sufficiently long plasma and strong decelerating fields, close to all the driver energy can be deposited into the plasma – except for a small fraction from the electrons at the very head of the drive bunch, as the wakefields don't fully develop there. However, when focusing a bunch to a small spot size (10 µm), the beam will quickly diverge following Eq. 2.13 and its charge density decreases – where the wakefields are formed, the focusing force impedes this. This divergent effect at the front of the bunch shifts the wakefield phase backward until, eventually, no wakefields are driven, a process known as *head erosion* [105]. This problem is exacerbated if the plasma is created by drive-bunch field ionization [105, 106], as the increasing transverse beam size lowers the strength of the beam's ionizing field [96].

Once the driver energy is deposited into the plasma in the form of wakefields, the trailing bunch must extract it. The *plasma-to-trailing-bunch* energy-transfer efficiency, also called energy-extraction efficiency, is defined by the ratio of deposited to extracted

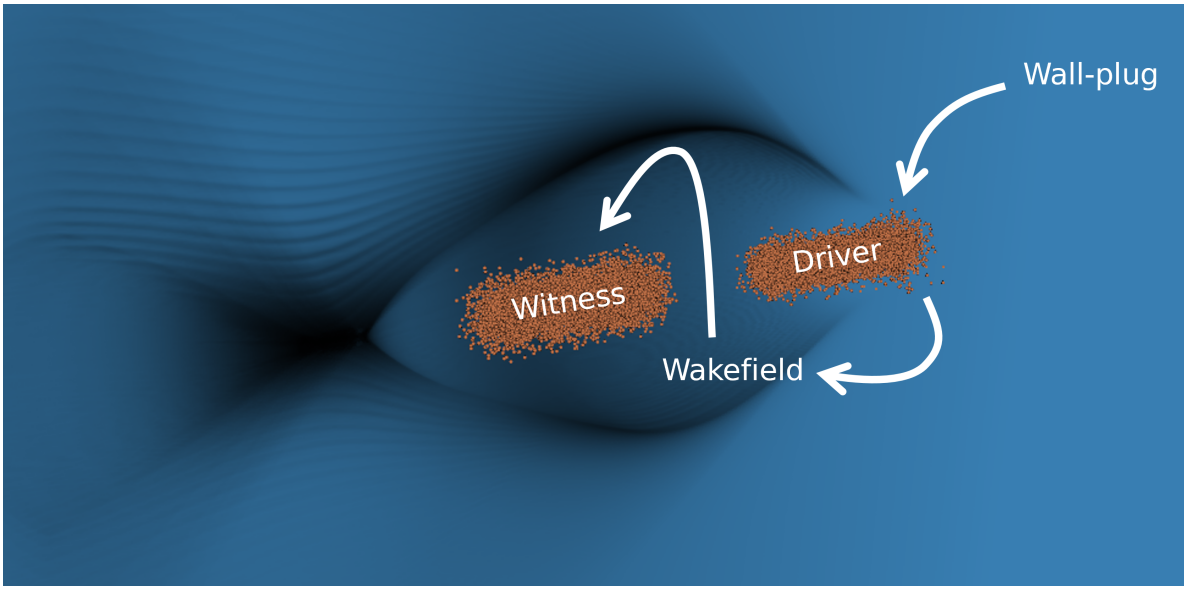

Figure 2.9: The energy transfer in a plasma accelerator is illustrated with the white arrows. The bunch macroparticles (orange points) propagate toward the upper right. The plasma density is shown with a logarithmic colormap ranging from blue (background density) to black. For convenience, the colormap is only shown for the opposite half of the blowout, as this removes the black veil masking the particle bunches from this point of view. Image Ref. [107].

energy, i.e.,

$$\eta_{p\to w} \equiv \frac{\Delta E_w \, Q_w}{\Delta E_d \, Q_d}, \tag{2.32}$$

where subscript $_w$ stands for the witness/trailing bunch.

It should be noted that the energy-extraction efficiency is closely related to beam loading. Building on the theory developed in Ref. [99], which is summarized in Sec. 2.4.2, the theory presented in Ref. [100] shows this relationship. There, the trailing-bunch current required to flatten the accelerating field until the blowout bubble closes is derived. Under these optimal beam loading conditions, the current shape of the trailing bunch is trapezoidal, and the following relationship with normalized parameters holds [100]:

$$Q_s E_s = \frac{\pi R_b^4}{16}, \tag{2.33}$$

where Q_s is the accelerated charge, and E_s is the accelerating field normalized to the

wave-breaking field (see. Eq. 2.26). Eq. 2.33 shows, for a fixed energy-extraction efficiency, under ideal beam-loading conditions, a trade-off between the accelerating gradient and charge: low charge can be accelerated with high gradients and high charge with low gradients. In other words, with the term $Q_s E_s$ as the energy extracted by the trailing bunch per unit length, it shows that, if the trailing-bunch current is shaped appropriately, the energy-extraction efficiency is independent of the accelerating gradient. It should be noted that these models assume ideal conditions such as beams without transverse tilts. Such tilts could give rise to transverse instabilities. This is treated later in Sec. 4.3, where possible limitations of energy-extraction efficiency are discussed.

Finally, the *driver-to-trailing-bunch* energy-transfer efficiency, or overall efficiency, is defined with

$$\eta_{d\to w} \equiv \eta_{d\to p}\, \eta_{p\to w} = \frac{\Delta E_w\, Q_w}{E_{d_0}\, Q_{d_0}}, \tag{2.34}$$

and with this the wall-plug power P_{WP} required to accelerate beams with a power P_{beam} can be calculated with

$$P_{\mathrm{WP}} = \frac{P_{\mathrm{beam}}}{\eta_{\mathrm{WP}\to d}\, \eta_{d\to w}}, \tag{2.35}$$

where $\eta_{\mathrm{WP}\to d}$ is the energy efficiency at which the drive bunches are produced.

Chapter 3

Experimental facility

The experimental results presented in this thesis were undertaken at the DESY research center in the photon-science user facility FLASH (*Free-electron laser in Hamburg*) [108]. The linear accelerator of FLASH delivers electron bunches to three beamlines, as shown in the schematic in Fig. 3.1.

In the first two beamlines, i.e., FLASH1 and FLASH2, the electron bunches are passed through arrays of alternating-polarity magnetic dipoles, i.e., undulators. Here, the electrons emit incoherently synchrotron radiation, which then interacts with the bunch, forming micro-bunches separated by the radiation wavelength. The emission becomes then coherent and is exponentially amplified, producing radiation with a narrow bandwidth and a peak power that can be orders of magnitude larger than that of storage ring sources. This process is called *self-amplified spontaneous emission* (SASE) [109, 110], and such radiation can be used in a plethora of scientific and industrial applications [111], as discussed in Chapter 1. FLASH can deliver radiation ranging from the vacuum ultraviolet (VUV) to the soft x-ray (XUV), and, over the years, has shown progress towards reaching shorter wavelengths: 109 nm in 2000 [112], 32 nm in 2005 [113], 13.7 nm in 2006 [114, 115], and its design wavelength of 6.5 nm in 2007 [116, 117].

The third beamline is dedicated to the FLASHForward [118] beam-driven plasma-

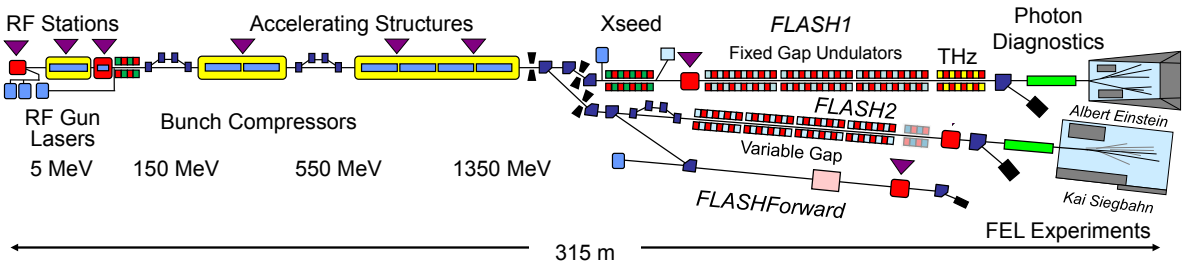

Figure 3.1: A schematic layout of FLASH, not to scale, where the bunch propagates from the left to the right. The RF stations are marked with a lilac downward triangle, where the accelerating modules are identified with yellow rounded rectangles. The red rounded rectangle at the left represents the gun and the other higher-frequency modules. The rectangles show in light blue laser systems, in dark blue dipole magnets, in black collimators or beam dumps, and in green photon diagnostics. The arrays of alternating-color squares represent magnetic undulators. Two experimental halls for users are placed at the end of FLASH1 and FLASH2. Image: DESY/Siegfried Schreiber.

wakefield experiment. It is at this experiment that the results presented in this thesis were achieved. This chapter gives a brief overview of the electron-bunch production, its usual parameters, and its transport from the photocathode at FLASH to the FLASHForward experiment. This is followed by an overview of the FLASHForward beamline, describing key elements such as the charge collimator, the plasma source, and beam and plasma diagnostics. An in-depth description of the FLASHForward beamline and its diagnostics can be found in Ref. [119].

3.1 Experimental setup

The bunches of FLASH are generated at a cesium telluride (Cs_2Te) photocathode, where ultraviolet laser pulses can inject up to 2 nC [120]. A normal-conducting RF gun at 1.3 GHz (L-band) accelerates these bunches up to 5.6 MeV. Then, seven superconducting L-band RF modules accelerate the bunch to 0.35–1.25 GeV, with an accelerating gradient of up to 25 MeV/m. The accelerating part of the facility comprises approximately 100 m. At a nominal bunch energy of 150 MeV and 450 MeV, two magnetic chicanes are placed [108]. These consist of an arrangement of dipole magnets such that the bunch

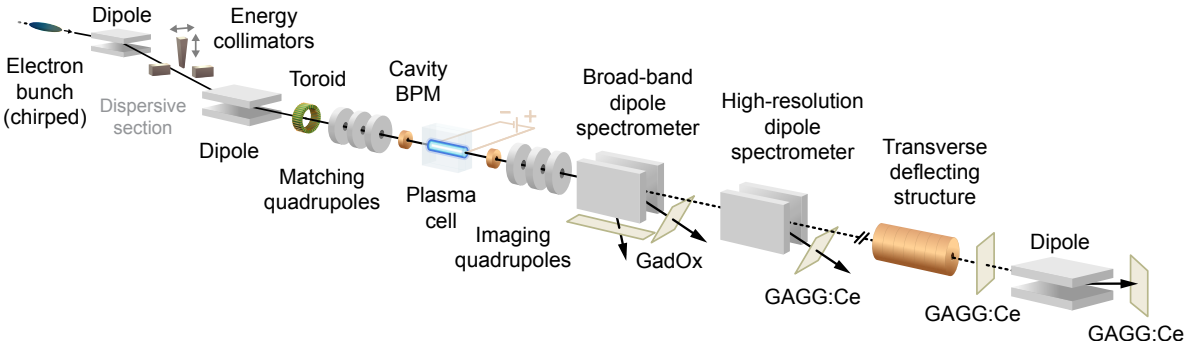

Figure 3.2: A schematic layout of the FLASHForward beamline, with the bunch delivered by FLASH propagating from left to right. The rectangular parallelepipeds in gray represent dipole magnets, the gray disks quadrupole magnets. The beige rectangles represent screens, with their scintillator material noted next to them. The charge and transverse position of the beam are measured with beam-position monitors (not all shown), while the former is also measured with toroids (not all shown). At the end of the beamline, the beam is stopped with a beam dump (not shown). Image adapted from Ref. [104] (CC-BY 4.0).

undergoes a parallel detour, where, at the end, it propagates collinearly to the initial trajectory. If the bunch has been imprinted an *energy chirp*, i.e., a correlation between particle energy and longitudinal position, the particles with a higher energy will follow a shorter path than the lower-energy ones. For a negative chirp, where the tail of the bunch has higher energy than the head, this leads to the tail moving forward and the head lagging back, relative to the center of the bunch. This process shortens the bunch length and is called *bunch compression*. The RF modules upstream of the magnetic chicanes can be used to imprint the energy chirp on the bunch and control the compression [108, 121, 122]. More control on this is given by a third-harmonic (3.9 GHz) module right before the first magnetic chicane, which can be used to linearize the cosine chirp imprinted by the L-band modules and thus linearize the longitudinal phase space [123, 124]. As an example, for a 1 nC bunch, its length can be compressed from 2 mm down to 50 µm rms, achieving a peak current of 2.5 kA. The nominal uncorrelated energy spread is below 0.1%, with a normalized transverse emittance of 1.4 mm mrad.

In the FLASHForward beamline, with a schematic shown in Fig. 3.2, the beam first traverses a dispersive section between two magnetic dipoles, where the horizontal

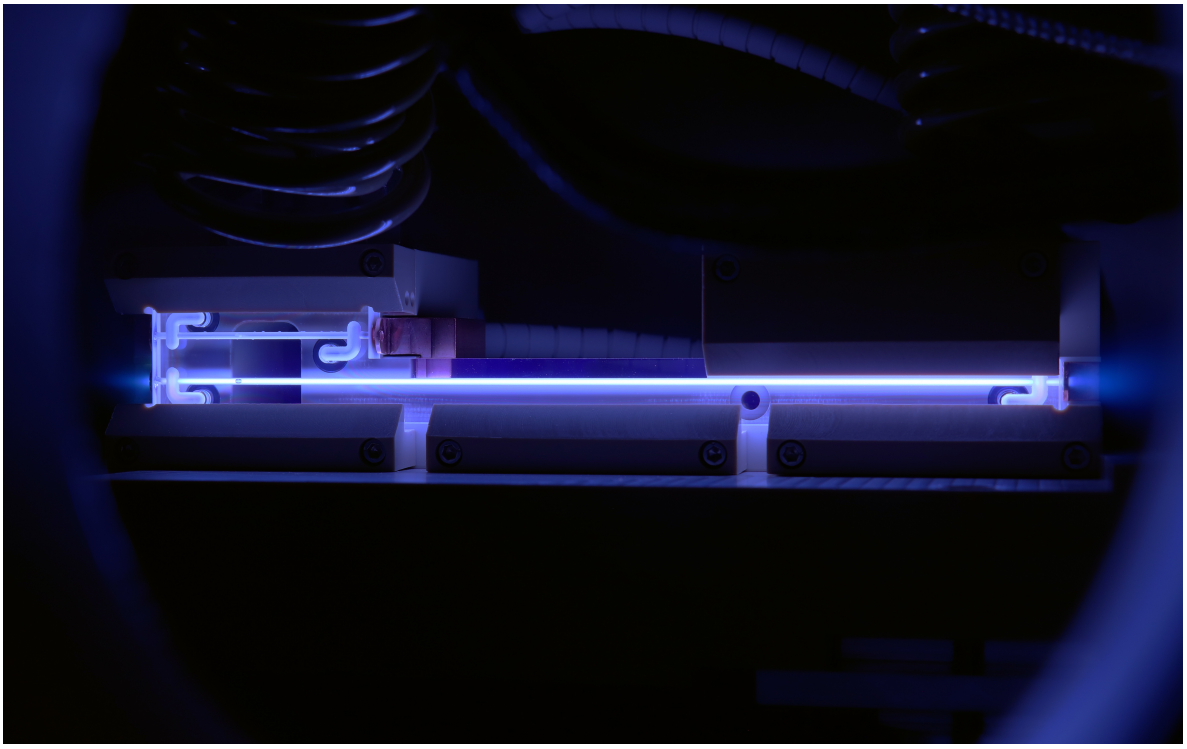

Figure 3.3: High-dynamic-range composite image of two plasma cells, with 50 mm (above) and 195 mm (below, bright) long sapphire capillaries. Both have L-shaped gas inlets near their ends and copper electrodes clamped at the ends. A cell can be selected for experimentation by moving it vertically such that the beam traverses it. To allow the introduction of a perpendicular-propagating laser pulse for a separate plasma injection experiment [130], transverse apertures are placed 20 mm downstream from the plasma entrance. The longer cell glows from recombination light, as the plasma was generated with an electrical discharge shortly before the picture was taken. A faint glow can be seen outside of the cell as plasma is expelled through the open ends. Image: Ref. [131] (CC-BY-NC-ND 4.0).

trajectory of each particle is determined by its energy. Here, as the particles correlate in longitudinal position and energy, they also do in longitudinal and horizontal position. Three movable energy collimators can block partially or fully the path of the beam, producing bunches of adjustable length [125–127]: one moves in from the left, one from the right, and one vertically at the center, each scraping at the tail, head, and center of the bunch, respectively. An in-depth description of this system can be found in Refs. [128, 129]. Further downstream, the micrometer transverse size of the electron bunches at the plasma cell entrance is adjusted with a set of magnetic quadrupoles.

Fig. 3.3 shows a picture of two stacked plasma cells: the upper being 50 mm long and the lower 195 mm. They each consist of a cylindrical channel with a 1.5 mm diameter and bent inlets near their ends that continuously supply gas. While the cells can be supplied with different types of gases, such as hydrogen, helium, nitrogen, and krypton, argon was exclusively used for the results of this thesis. At the ends of the channels, electrodes are placed such that, when triggered, they produce an electric potential in the order of tens of kilovolts. When the electrical discharge is triggered, free electrons are quickly accelerated and drive an avalanche-ionization process, ionizing the plasma [60]. The light emitted by the plasma is then collected with a lens and transported with optical fibers to an optical spectrometer, where the emission lines of different gases can be measured [132], as well as the spectral line broadening (SLB) [133]. For the H_α emission line in the Balmer series, the SLB and the plasma electron density are related by a temperature-dependent power law [132, 134, 135]. To measure the plasma density in an argon gas, it was doped with 3% hydrogen. Fig. 3.4 shows the plasma density decaying approximately exponentially with a half-life of 3.8 ± 0.1 µs, where the rms error between the fit and the measured densities is 7%. To change the plasma density experienced by the bunch arriving at a constant time, the discharge timing was adjusted. For example, when discharging earlier, the plasma has more time to recombine, and therefore, the bunch experiences a lower plasma density. Discharging later allows a maximum interaction density as high as at the peak in Fig. 3.4, i.e., 4.8×10^{17} cm^{-3}. For a better overview, the timing system is illustrated in Fig. 3.5.

A complementary metal-oxide-semiconductor (CMOS) camera, which is placed next to and facing the plasma cell, providing images similar to Fig. 3.3, measures the optical light emitted by the plasma, by integrating the light over 24 µs shortly after the beam–plasma interaction. The purpose of this camera is to measure the light emitted by the plasma during recombination, as it is correlated with the energy remaining after a beam–plasma interaction [136–138]. As described previously, the plasma density is adjusted by changing the electrical-discharge timing, which also changes the light yield

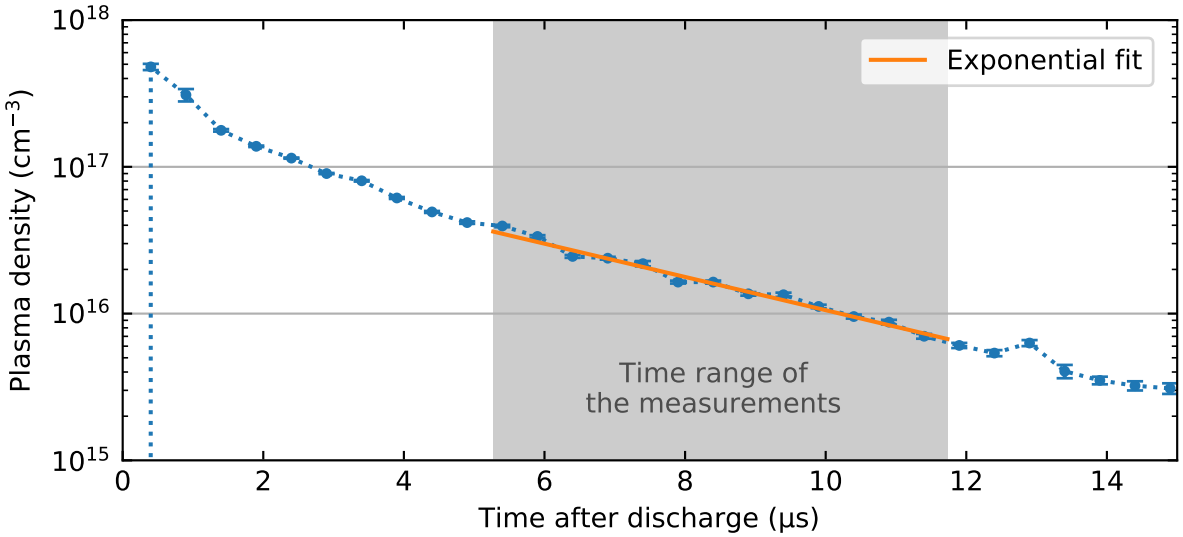

Figure 3.4: Plasma density, as measured with optical-emission spectroscopy, decaying from 4.8×10^{17} cm^{-3} to $\sim 3 \times 10^{15}$ cm^{-3} in 15 µs. Within the typical timing range of the experiment, an exponential fit yields a half-life of 3.8 ± 0.1 µs. The analysis was performed by J. M. Garland.

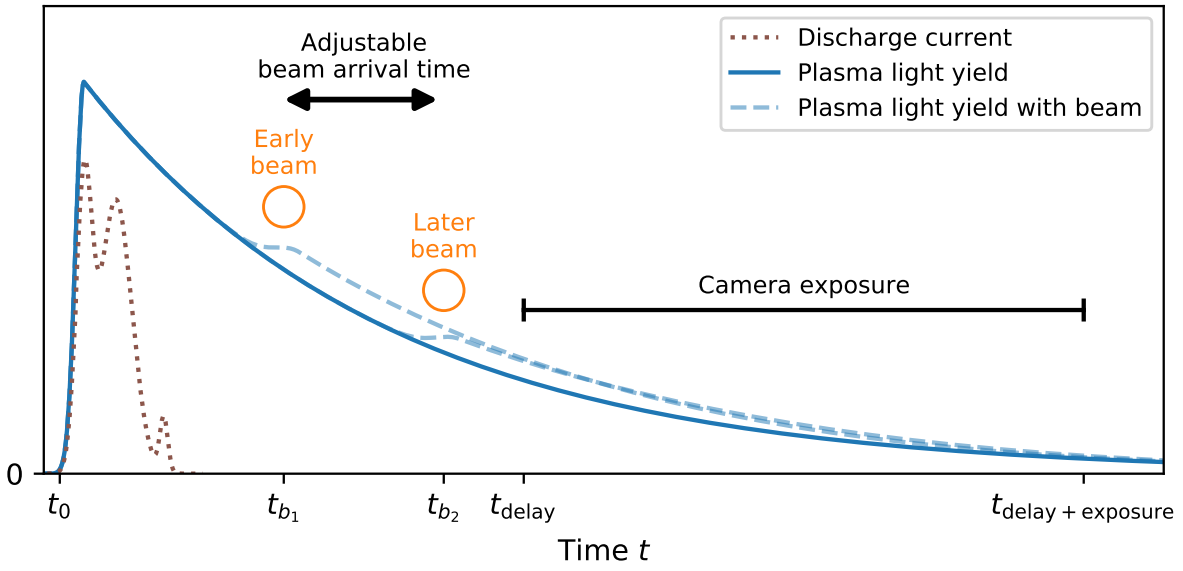

Figure 3.5: A qualitative schematic showing the discharge current (brown dotted line), starting at t_0, and the exponentially decaying plasma recombination light (blue line). The orange circle represents the arrival time of the beam t_b, which, through its energy deposition, increases the light emission (blue dashed line); two different timings of the same bunch are shown here. The camera starts the acquisition at t_{delay} and stops at $t_{\text{delay + exposure}}$, integrating the plasma light.

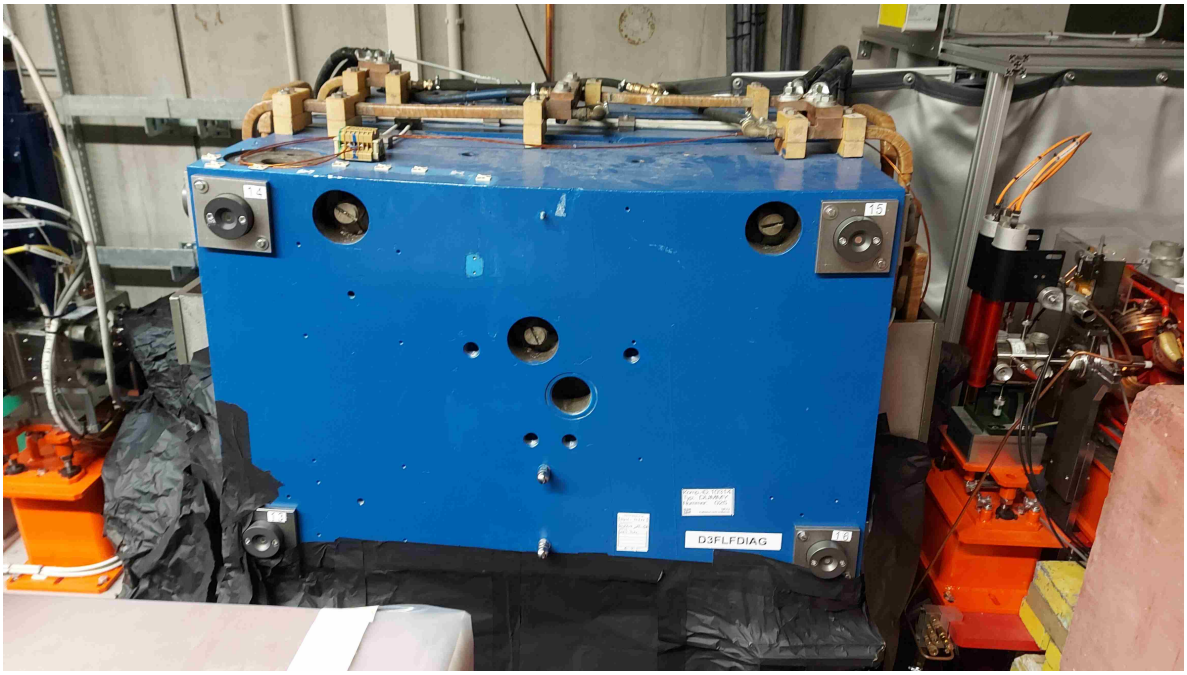

Figure 3.6: Picture of the broad-band-spectrometer dipole magnet (blue). The beam propagates through a pipe in a vacuum from right to left.

recorded by this camera. Therefore, to keep the background light during plasma-density scans constant, the camera was also shifted in time, keeping the relative time between discharge initiation and camera delay constant. This procedure is equivalent to changing only the beam arrival time, as illustrated in Fig. 3.5.

After the interaction with plasma, two dipole energy spectrometers, which cannot be operated simultaneously, bend the beam trajectory with a magnetic dipole each. The position at which the particles intersect with a screen at the spectrometers is a function of their energy and allows measuring the energy spectrum of the particle bunch. The diagnostic screens consist of, respectively, *gadolinium-oxysulfide-garnet* (GadOx) scintillator screens located outside the vacuum to measure broad-band energy spectra (the dipole shown in Fig. 3.6, and the screens in Fig. 3.7), and an in-vacuum *cerium-doped gadolinium-aluminium-gallium-garnet* (GAGG:Ce) scintillator screen to measure high-resolution energy spectra and horizontal beam sizes. The resolution of the camera–screen setups are 600 µm and 50 µm for the broad-band spectrometer, respectively for the low-energy and high-energy screens (see Figs. 3.2 and 3.7), and

Figure 3.7: Left: picture of the 1-m-long low-energy screen, taken from below the dipole. A ruler for spatial calibration can be seen placed right below the screen. Right: picture of the high-energy screen, taken from the side, where the cameras are not visible. The double arrows show the same components in the pictures. In both cases, the signal emitted from the screen scintillator (blue) is reflected on a mirror to the cameras, as shown with the single gray arrows.

6.2 µm rms for the high-resolution spectrometer (see Fig. 3.2). The imaging of the bunches on the screen is controlled via magnetic quadrupoles located right after the plasma cell (see Fig. 3.2).

If the magnetic dipoles are not operational, the bunches can propagate further downstream to a *transverse deflecting structure* (TDS) [139–141]. Through variable polarization, this ∼12 GHz (X-band) RF structure can streak the bunch in different planes [140]. With its time-varying transverse fields, the deflection of particles is dependent on their longitudinal position within the bunch. In combination with a screen, this allows measuring the longitudinal charge distribution (i.e., the current along the bunch) as well as the length of the bunch [119, 139]. To keep the deflection linearly dependent on the longitudinal coordinate, the TDS is operated at the phase where the RF field switches sign, i.e., *zero crossing* (ZC), of which there are two. If the screen is not used, the beam passes through a final dipole, bending the trajectory horizontally to

the beam dump. In this dispersive section, the horizontal position of the particles is determined by their energy, and, with the TDS, the vertical position by the particle's longitudinal position within the bunch. Therefore, placing a screen before the beam dump allows measuring the longitudinal phase space of the bunch. Such a measurement of the drive bunch used later in Chapter 5 is shown in Fig. 3.8.

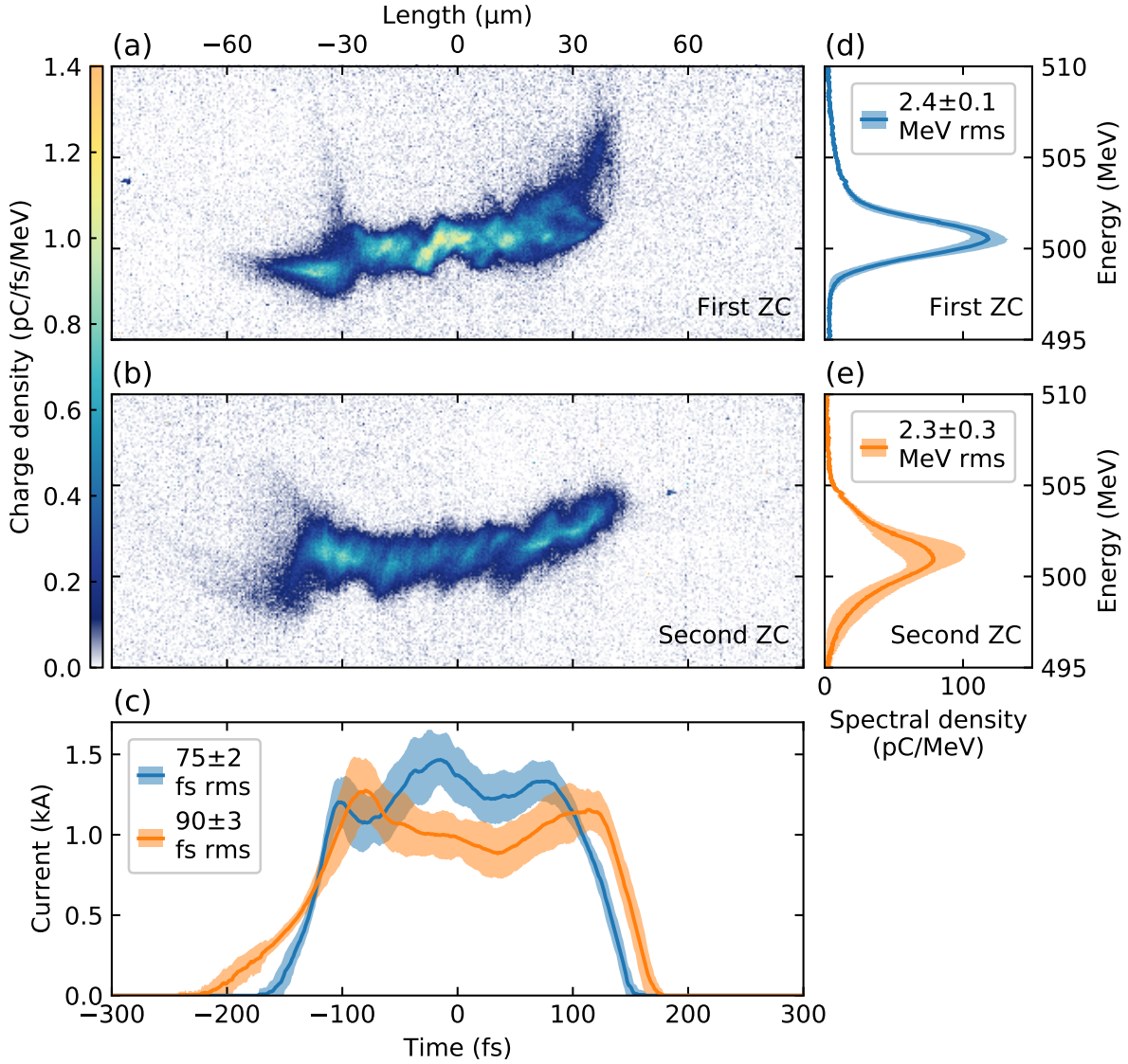

Figure 3.8: The time-streaked and energy-dispersed beam for the two ZCs, (a) and (b), and the respective projected energy spectra, (d) and (e). In (c), the bunch current is shown for both ZCs, where the colors correspond to the ZC as in (d) and (e). While (a) and (b) show individual images, the lines in (c–e) show the average of 50 measurements and the corresponding colored bands the rms along the given axis. The legends show the average of the rms spectrum or current, with the quoted error being the corresponding rms.

Chapter 4

Energy-extraction efficiency and beam-quality preservation

The major potential of plasma accelerators is their large accelerating gradients, which promise to shrink the accelerators' environmental footprint and building costs. However, the efficiency with which energy is extracted from the plasma by the trailing bunch can limit the overall performance of a plasma accelerator – in more than one way. Intuitively, any energy not transferred to the trailing bunch entails a higher electricity bill and will be missing energy at the delivery point. While this could be "only" an environmental and financial problem, the energy remaining in the plasma has to be removed in some way. Otherwise, a build-up of energy can lead to extreme heat and damage to the device containing the plasma. As applications such as linear colliders and FELs usually operate at an average repetition frequency of $\mathcal{O}(10\text{ kHz})$ and a beam power of $\mathcal{O}(1\text{ MW})$, they could be especially susceptible to this issue.

The required cooling rate can be approximated by multiplying the repetition rate f, the drive-bunch mean energy E_d and charge Q_d, the fraction of energy deposited into the plasma, i.e., the driver-to-plasma efficiency $\eta_{d\to p}$ as defined with Eq. 2.31, and the fraction of energy not extracted by the trailing bunch, i.e., $(1-\eta_{p\to w})$, with the plasma-to-trailing-bunch efficiency $\eta_{p\to w}$ defined in Eq. 2.32. Dividing by the plasma

length L gives the cooling rate per unit length, i.e.,

$$\frac{d}{ds}P_{\text{cooling}} = \frac{fE_dQ_d}{L}\eta_{d\to p}(1-\eta_{p\to w}). \tag{4.1}$$

With $\eta_{d\to p}\eta_{p\to w}\,E_dQ_d = \Delta E_wQ_w$ from Eq. 2.34 and substituting the trailing-bunch mean-energy gain over the length with the accelerating gradient, i.e., $\Delta E_w/L = E_z$., Eq. 4.1 can be rewritten as

$$\frac{d}{ds}P_{\text{cooling}} = fE_zQ_w\left(\frac{1}{\eta_{p\to w}}-1\right). \tag{4.2}$$

Equation 4.2 is valid independent of the medium and driver type. Also, it does not include any energy deposited into the plasma during its formation, which would require additional cooling. To estimate how important this is, the following approximation can be made. At FLASHForward, the plasma is created through an electrical discharge, as explained in Sec. 3.1. In this setup, an energy of $\mathcal{O}(1\text{ mJ})^*$ is deposited into the plasma during the discharge of a 50 mm cell [142]. With a bunch frequency of 10 kHz, as intended for the HALHF collider [30], this yields a power of $\mathcal{O}(0.1\text{ kW m}^{-1})$. For several reasons, this estimate is an upper bound. First, in this setup, the discharge produces an initial plasma density of $\mathcal{O}(10^{17}\text{ cm}^{-3})$. However, for acceleration, lower densities of 10^{15}–10^{16} cm^{-3} are used, which are obtainable during recombination (see Fig. 3.4). Thus, in principle, a system directly producing the required density could be designed, leading to less energy introduced into the system. Second, the discharge setup was not designed under consideration of energy efficiency, and there is potential to optimize the electrical system. Third, at a sufficiently high repetition rate, the beam would interact with the plasma before it is fully recombined [143]. This would require re-ionizing only a fraction to sustain a constant plasma density for the beams, leading to less average energy deposition by the plasma production mechanism. With the required

*This estimate is based on comparing the energy input and output of the discharge system, which includes circuit elements like resistors, where energy is also dissipated [142].

cooling power planned for the plasma accelerating stages in the HALHF collider at 93 kW m^{-1} [30], the required cooling due to the plasma formation is three orders of magnitude smaller, and it is reasonable not to consider it in Eq. 4.2.

Assuming a maximum technically feasible cooling power, Eq. 4.2 shows that a low energy-extraction efficiency will require lowering the frequency, accelerating gradient, trailing-bunch charge, or a combination of these. As an example, at a frequency of 10 kHz, accelerating 1 nC trailing bunches with a 1 GV/m gradient and a 20% energy-extraction efficiency requires a cooling rate of 40 kW/m, which is an order of magnitude larger than that of CLIC's main-bunch accelerator at 1.6* kW/m. As such key machine parameters are generally determined by the application, Eq. 4.2 shows that energy inefficiency could severely hamper the implementation of plasma accelerators. As a result, significant effort was invested in demonstrating high energy-extraction efficiency. In the following, a selection of high-impact results is introduced.

The first result with significant plasma-to-trailing-bunch energy-transfer efficiency was published in 2014, with 30% [144]. This result was achieved with a single bunch, in which charge at the head drove the wakefields and charge at the tail was accelerated. Later, in 2021, new results with a driver and trailing bunch pair were published, with 42% extraction efficiency [104]. This result was achieved while simultaneously preserving the charge and energy-spread-to-average-gain ratio of the trailing bunch – without this constraint, an efficiency of up to 71% was measured. These two publications quoted the longitudinally averaged efficiency, as it was measured with a spectrometer downstream of the plasma. With a new technique†, using the light emitted by the plasma, a localized extraction efficiency of 58% was reported in 2022 [137, 138] – averaged longitudinally, the efficiency was 38%. In principle, the extraction efficiency can be significantly higher, as analytical work shows that 90% could be possible [100] – with similar results in

*This can be estimated using Eq. 4.2 with the following collider parameters at a center-of-mass energy of 380 GeV: a frequency of 17.6 kHz, a main-bunch charge of 833 pC, an accelerating gradient of 72 MV/m, and an RF-to-main-bunch efficiency of 39.8% [32, T. 4.1 and p. 70].

†This technique will be explained in more detail in Sec. 4.4.

different simulations with optimized bunch currents [145, 146].

While the predicted efficiency and the experimental work might seem promising, applications such as colliders and FELs have additional requirements: high beam quality, i.e., low emittance and energy spread. In a collider, both are important for focusing the beam to small spot sizes at the interaction point. The importance of the beam emittance – and also the machine efficiency – becomes clear when the definition of Luminosity (see Eq. 1.3) is rewritten with beam parameters. Using $\sigma_{x/y} = \sqrt{\epsilon_{G,x/y}\,\beta_{x/y}}$ from Eq. 2.4 and $\epsilon_{G,x/y} = \epsilon_{x/y}/\gamma$ from Eq. 2.10, the Luminosity of two colliding identical Gaussian bunches becomes

$$\mathcal{L} = \frac{1}{4\pi mc^2} \frac{P_{\mathrm{WP}}}{\sqrt{\beta_x \beta_y}} \frac{N \eta_{\mathrm{WP}\to b}}{\sqrt{\epsilon_x \epsilon_y}}, \tag{4.3}$$

with the beam power $P_b = \gamma mc^2 N f = P_{\mathrm{WP}}\,\eta_{\mathrm{WP}\to b}$, the machine's wall-plug-power consumption P_{WP} and wall-plug-to-beam energy efficiency $\eta_{\mathrm{WP}\to b}$. Equation 4.3 shows that a smaller beam emittance increases the Luminosity, and, to this goal, the emittance in linear colliders can be as low as 0.01 mm mrad [27, 31]. However, to mitigate the effects of Beamstrahlung [147], the emittance in one plane is usually larger, with 1–10 mm mrad [27, 31]. In an FEL, to sustain high beam brightness (see Eq. 1.4), the emittance per 0.1% energy bandwidth has to be 1 mm mrad or smaller. While manipulation of the energy spread with plasma wakefields [148–150] and energy spread preservation have been shown [104], this is not the case for preserving the emittance. Failing to demonstrate this will bar plasma accelerators from augmenting or replacing accelerators with strict emittance requirements.

The emittance of a bunch can grow through many processes [97]. Transverse fields can lead to instabilities [151, 152]; a bunch not focused to the matched beta function or misaligned as a whole can suffer from slice decoherence [73, 153–155] (see Sec. 2.2.4); if the plasma ions move, they could lead to non-linear focusing fields [156]; and the scattering of the beam with the background gas or plasma ions can also lead to emittance growth [157–159]. While many mitigation strategies exist for all these processes, they

can be partly conflicting. For example, while moving plasma ions can lead to emittance-increasing non-linear focusing fields, they can also mitigate hosing by depressing the resonance with a longitudinally varying focusing strength. Preserving emittance is, thus, a careful balancing act of input parameters. A detailed discussion of this topic can be found in Ref. [97].

In Sec. 4.2, new experimental results are presented, where the emittance of a trailing bunch is preserved while sustaining significant energy-extraction efficiency. These experimental results were led by C. A. Lindstrøm [160], and are here presented in a summarized manner for the following reasons. The author was involved in numerous experimental campaigns, mainly in setting up the beamline and establishing and optimizing the beam–plasma interaction, which yielded this result. Also, following the argument laid out in Chapter 1, for high beam-power facilities, demonstrating high energy efficiency is only meaningful if the accelerated-beam quality is preserved, and vice versa, which necessitates introducing and discussing these results. These are followed by a discussion on the instabilities that can limit both preserving the emittance and reaching higher energy-extraction efficiencies. As such instabilities must be understood with more detail and characterized experimentally to assess their imposing limitations, a new method to non-destructively measure the energy-extraction efficiency with longitudinal resolution, and possibly the onset of instabilities, is introduced in Sec. 4.4. These results were led by L. Boulton [137, 138]. Here, again, the author was involved in establishing the experimental working point. A further reason to present these results briefly is that they verify the use of the light emitted by plasma during recombination to measure the electron re-acceleration, a process that limits energy-deposition efficiency and is later described in Sec. 5.1 and measured in Fig. 5.3. Conversely, Fig. 5.3 verifies the assumption that allows the novel method to measure the energy-extraction efficiency with longitudinal resolution.

For the results presented in this chapter, i.e. emittance preservation and longitudinally-resolved measurement of the energy-extraction efficiency, a detailed calibration of the

spectrometer diagnostic is required. The calibration of the low-energy screens of the broad-band energy spectrometer was performed by the author. The calibration process included finding methods to correct for different distorting effects, such as the light-yield dependency on the beam–screen angle, the spatially-varying photon-capture efficiency of the camera lens, and the saturation of the scintillator. While the calibration was performed for the results presented later in Chapter 5, these findings were used as guidance for the calibration of the individual screens in the results of this chapter. For this reason, and as a reference for future measurements, the following section presents an overview of the calibration process before introducing the experimental results of this chapter.

4.1 Calibration of the broad-band energy spectrometer

The energy spectrometer consists of a magnetic dipole and a screen, as can be seen in Fig. 3.2. The key idea of a dipole spectrometer is that, with a fixed magnetic field, particles with different momenta have their trajectory bent differently, as described by the Lorentz force (see Eq. 2.4). Placing a screen after propagation through the magnetic field allows for measuring the particle's position, which in turn allows to determine their energy.

This section describes the process required to retrieve the energy spectra from a raw spectrometer image. Each subsection details the consecutive steps, with a general overview in the last, which also shows the evolution of a sample spectrometer image.

In this setup, three cameras, imaging consecutive and overlapping screen sections, were used to cover the 1-m-long screen, as shown in the left picture in Fig. 3.7 and represented with the horizontal screen in Fig. 4.1(a). Since the calibration process is the same for all three cameras, only the results for one are shown. The photon counts collected by the camera are denoted with $N(\mathrm{px_y})$, reflecting that the counts are a

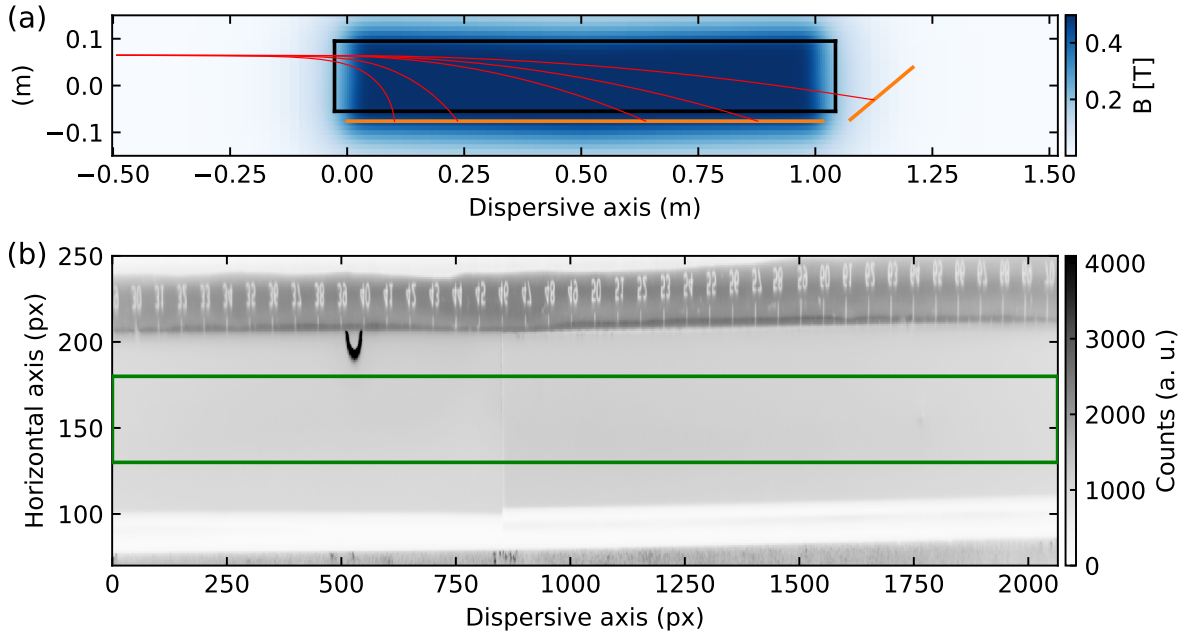

Figure 4.1: (a) Trajectory (red line) of an electron in the spectrometer dipole (black rectangle) with different momenta: 20, 50, 250, 450, and 1050 MeV/c. The electron propagates towards the right and down, crossing the horizontal with low energy and the angled screen with high energy (orange lines). The magnetic field strength (blue) is shown for a dipole current of -300 A, which, in the uniform area, corresponds to -0.5 T. (b) Image of the scintillator screen with uniform light from a nearby LED stripe. The ruler for spatial calibration is visible at the top and its warped appearance comes from how it is attached to the screen. The green rectangle shows the area in which the beam is usually located.

function of position in the vertical (y) dispersive axis discretized in pixels with equal size $\mathrm{px_y} = \mathrm{px_x}$. While the counts are also dependent on the horizontal (x) non-dispersive axis, the beam stays approximately within a ± 5 mm horizontal range during operation. This is a small fraction of the horizontal range that the camera images ($\sim$300 mm) and small compared to the range the charge moves in the dispersive axis ($\sim$410 mm). Therefore, as the beam is at approximately a constant horizontal position, the photon counts collected by the camera are assumed to be independent of x.

4.1.1 Photon collection of the camera lens

The photon-capture efficiency of the camera–lens system varies for different positions on the screen. To measure this effect, an LED light strip was placed next to the screen to illuminate it uniformly. Fig. 4.1(b) shows an image under such conditions, and Fig. 4.2 shows the projection of the signal in the region of interest on the dispersive axis. Here, the photon capture efficiency varies quadratically along the screen, with the maximum around the center. The signal drop on the center-left side is caused by the overlapping of two separate scintillator screens, which changes the reflection of light. During operation, the photons are emitted by the scintillator and not reflected; moreover, no increase in signal was observed at this position. Therefore, this area is neglected when fitting the quadratic function f_{quadr}. The photons recorded by the camera when correcting for the photon-capture efficiency, i.e., $N_\gamma(\mathrm{px_y})$, can then be calculated with

$$\frac{d^2 N_\gamma(\mathrm{px_y})}{\mathrm{px_x}\,\mathrm{px_y}} = \frac{d^2}{\mathrm{px_x}\,\mathrm{px_y}} \frac{N(\mathrm{px_y})}{f_{\mathrm{quadr}}(\mathrm{px_y})}. \tag{4.4}$$

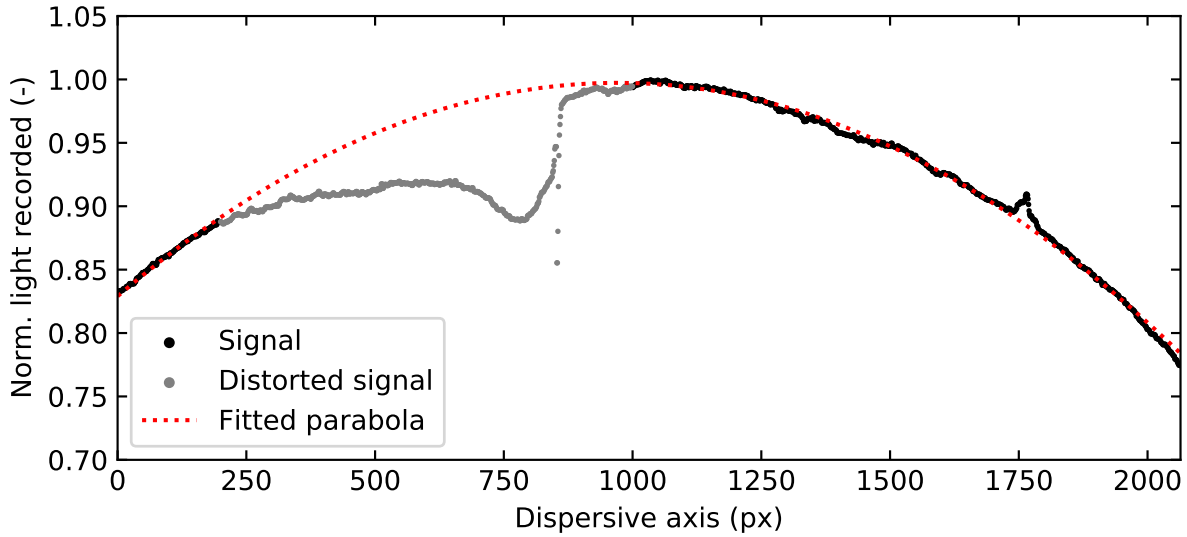

Figure 4.2: The reflected light intensity on the screen scintillator along the dispersive axis, with uniform illumination and within the usual region of interest as shown in Fig. 4.1(b).

4.1.2 Photon-yield dependency on the incident angle

Depending on the magnetic field and bunch energy, the particles will hit the scintillator screen at varying angles, and they will interact with a different amount of scintillator material, as illustrated in Fig. 4.3. Therefore, the incident angle α affects the number of photons emitted by the scintillator. Assuming that the photon count I_γ is proportional to the particle's path x within the scintillator, the intensity varies as

$$I_\gamma(\alpha) \propto x = \frac{d}{\cos(\alpha)}. \tag{4.5}$$

Using the angles from the spectrometer model as in Fig. 4.1(a), they vary as shown in Fig. 4.4. Here, one can see that the angle can change the photon yield by a factor of four. For the measurements shown with this spectrometer, each image bin is corrected by this factor, with

$$\frac{d^2 N_{\gamma\alpha}}{\mathrm{px_x}\,\mathrm{px_y}} = \frac{d^2\, N_\gamma(\mathrm{px_y})}{\mathrm{px_x}\,\mathrm{px_y}} \cdot \cos\left(\alpha(\mathrm{px_y})\right), \tag{4.6}$$

where the recorded counts are now independent of the dispersive position, as the effects influencing the counts along this axis are now corrected.

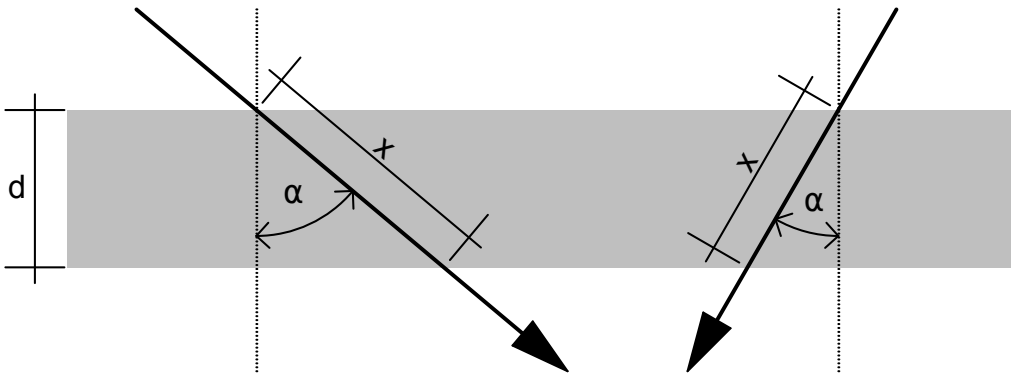

Figure 4.3: Schematic showing the incident angle α of a particle when traversing the scintillator of thickness d, showcasing two different angles. Image Ref. [161].

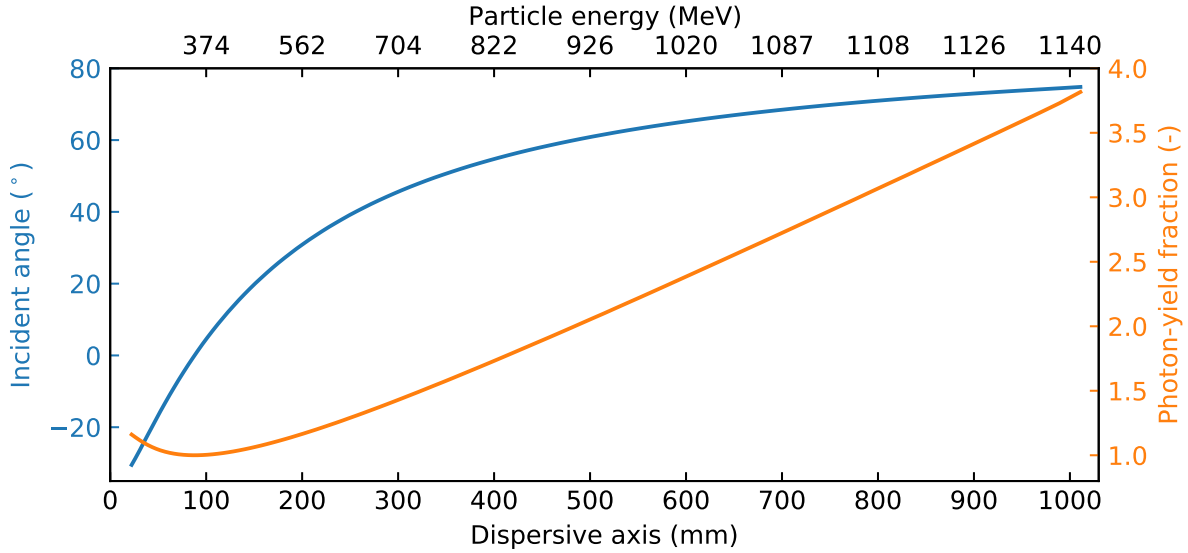

Figure 4.4: The incident angle of a particle on the scintillator screen (blue) along the dispersive axis for a dipole magnetic field at −0.5 T. The fraction by which the photon yield changes, i.e., $\cos(\alpha)^{-1}$, is shown in orange. The non-linear energy axis is shown at the top.

4.1.3 Scintillator signal decay

The number of photons emitted by the scintillator is a function of time, as shown in Fig. 4.5. Here, the camera was set to an exposure time of 30 µs, and, with a constant beam, the camera delay was scanned in time. The decay constant of the scintillator signal can be measured by fitting an exponential function. However, yielding a better agreement and following Ref. [162, Eq. 7.2], a two-component exponential function can be fitted to the signal, with

$$N(t) = A \exp\left(-\frac{t}{\tau_f}\right) + B \exp\left(-\frac{t}{\tau_s}\right), \tag{4.7}$$

where N is the number of photons, t is time, and A and B are relative magnitudes of the two decay processes. As one of the two processes is often much faster, the decay constants τ_f and τ_s are named after "fast" and "slow" [162, Ch. 7.1].

The camera's exposure time is usually $\mathcal{O}(1\text{ ms})$ to avoid image saturation, and only a fraction of the total emitted light is recorded. Therefore, the delay and exposure

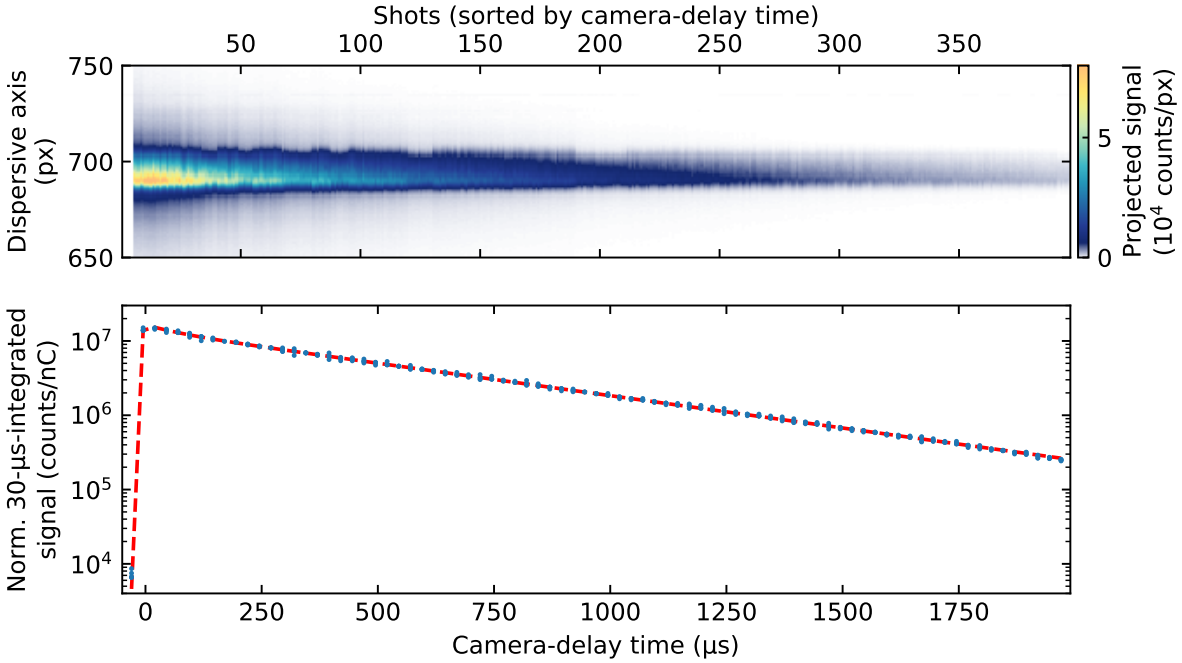

Figure 4.5: (a) A waterfall of the spectrometer images and (b) the total signal on screen normalized by the beam charge (blue points) when scanning the camera-delay time. The dashed red line in (b) shows the least-squares-fitted Eq. 4.7, where $\tau_f = 48 \pm 14$ µs and $\tau_s = 344 \pm 1$ µs.

time will affect the total number of photons recorded, and, if not corrected, lead to a wrong charge measured. This can be corrected with knowledge of the scintillator signal decay and an absolute calibration [163, 164]. A simpler option is to perform the charge calibration, as described later in Sec. 4.1.5, with the same camera delay and exposure as used in the measurements to analyze. This enforces the signal integration to occur over the same time range and to a comparable measured scintillator response, i.e., the same photon counts per beam charge. For the results in this thesis, the latter approach is used.

4.1.4 Spatial calibration and resolution

The GadOx scintillator screen resolution could allow measuring features as small as ∼30 µm. As the screen is located just outside the vacuum chamber, the electrons have to traverse a 1 mm thick stainless-steel wall. Through scattering, this causes a blurring

of the order of 10 µm. However, the resolution of the system is limited by the optical resolution of the camera–lens setup, which is approximately 600 µm. It should be noted that the resolution does not affect the average position of the charge measured on the screen and, thus, not the average energy of the particles.

For the spatial calibration, the ruler markings along the dispersive axis, as shown in Fig. 4.1(b), were used, yielding a pixel resolution of 0.196 mm/px. For the results presented in this thesis, the energy spectra of the bunches are used, which are computed by integrating the spectrometer images over the horizontal (x) axis. Therefore, a precise estimate of the horizontal resolution is not required, and it is assumed similar to the dispersive vertical (y) axis. The spatial calibration can be applied with

$$\frac{d^2N_{\gamma\alpha}}{dx\,dy} = \frac{d^2N_{\gamma\alpha}}{\mathrm{px_x}\,\mathrm{px_y}} \cdot \frac{\mathrm{px_x}}{dx}\frac{\mathrm{px_y}}{dy}, \tag{4.8}$$

where the pixel width $\mathrm{px_x} = \mathrm{px_y} = 1$.

4.1.5 Charge calibration

The signal density on the image is in counts per area and has to be converted to charge density to yield charge measurements. For this, at a fixed bunch energy and magnetic field, the bunch charge was varied with the collimators upstream, as shown in Fig. 4.6(a). A clear linear correlation between the measured charge Q by the beam-position monitors and the total counts of the recorded image is shown in Fig. 4.6(b). To convert the image to a proper measurement of charge density, the slope of the fitted linear function $\frac{dQ}{dN_{\gamma\alpha}}$ is used, with

$$\frac{d^2Q}{dx\,dy} = \frac{d^2N_{\gamma\alpha}}{dx\,dy} \cdot \frac{dQ}{dN_{\gamma\alpha}}. \tag{4.9}$$

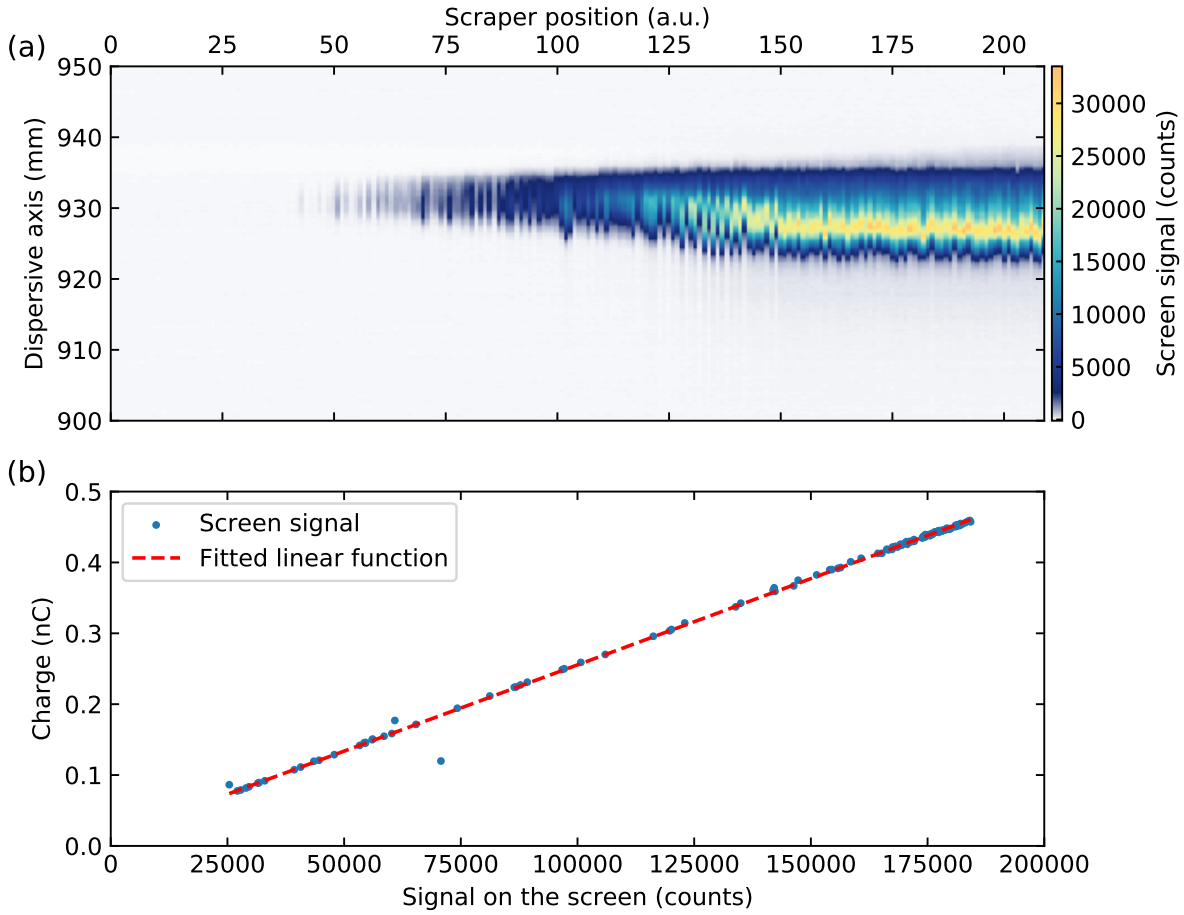

Figure 4.6: (a) Energy spectrum of a beam when removing a collimator to increase the charge on the screen. (b) The signal measured at the spectrometer screen versus the charge at the beam-position monitor, where charges below 80 pC are below the operational range of the diagnostic.

4.1.6 Scintillator saturation

Usually, the number of photons emitted by the GadOx scintillator scales linearly with the bunch charge, as demonstrated in Fig. 4.6(b). However, the scintillator can saturate at a charge density of $\mathcal{O}(\mathrm{nC/mm^2})$, leading to fewer photons emitted for each new electron. This is described by Birks' law [165, 166]

$$\rho_{\mathrm{scint}} = \frac{\rho_{\mathrm{beam}}}{1 + B_{\mathrm{const}}\rho_{\mathrm{beam}}}, \tag{4.10}$$

where ρ_{scint} is the charge density measured at the scintillator, ρ_{beam} the charge density of the beam traversing the scintillator, and B_{const} Birks' constant. Fig. 4.7 shows how the signal from a scintillator decreases due to saturation. As in Ref. [164], the saturation threshold can be "defined as the peak charge density, at which the scintillation signal has dropped to 90% compared to the linear behavior". This threshold varies for different materials.

Fig. 4.8 shows a measurement of this saturation effect at the spectrometer screen. The

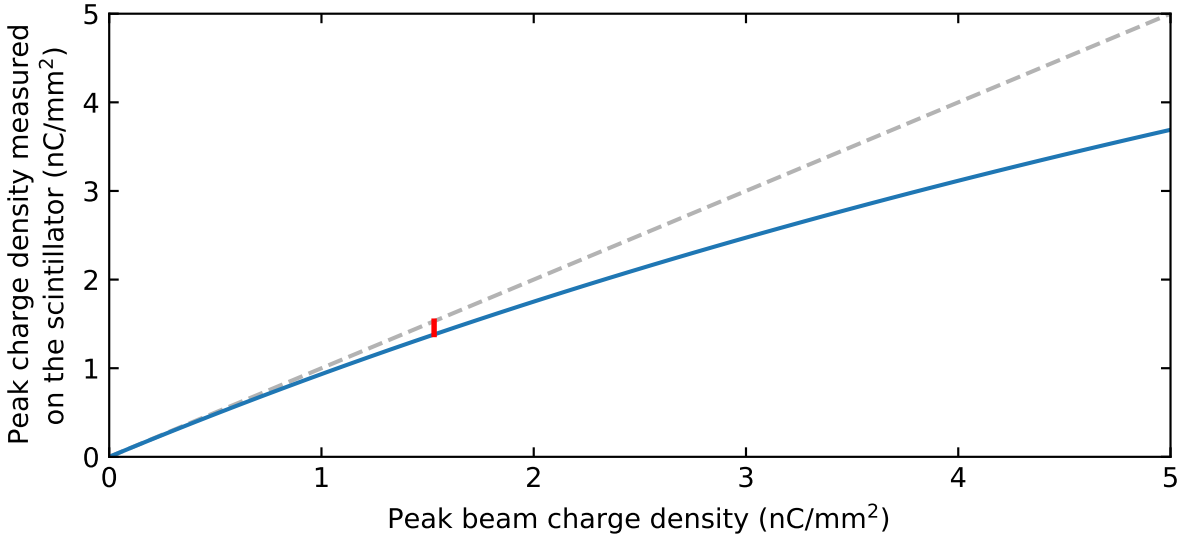

Figure 4.7: The measured charge density on a scintillator for increasing beam density (blue), following Eq. 4.10 and $B_{\mathrm{const}} = 7.1\ \mathrm{mm^2pC^{-1}}$. At lower densities, the relationship is linear; at higher densities, the signal increases at a lower rate. For comparison, a linear scaling is shown (gray dashed line). The density at which the signal differs by 10% from the linear scaling is marked (red line).

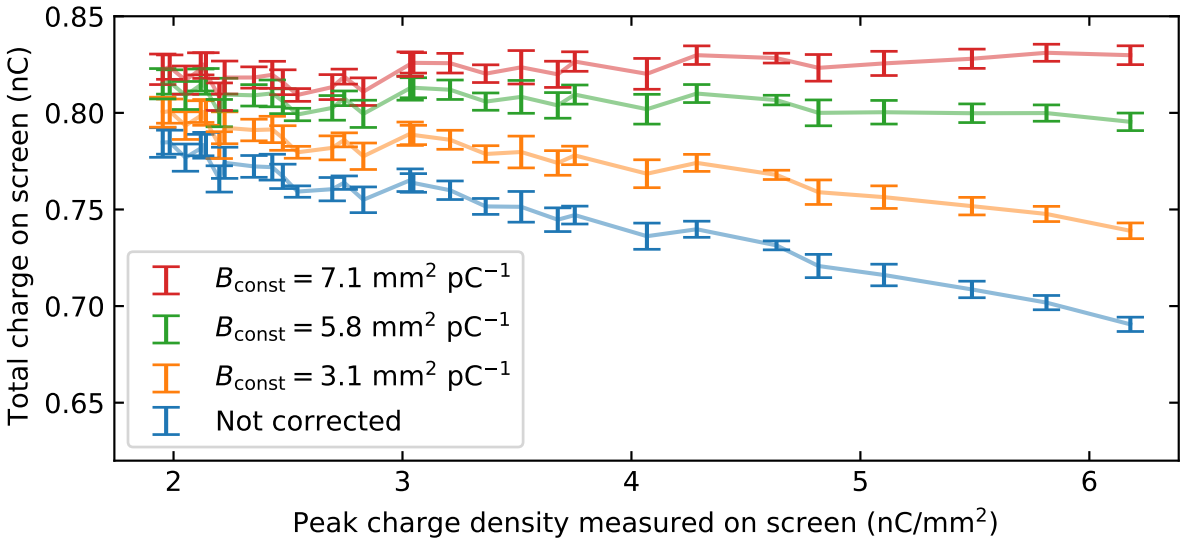

Figure 4.8: The total measured charge on the screen as the beam density increases (blue error bars and line), while the total bunch charge is kept constant. The other colors show the total measured charge when correcting for the scintillator saturation effect with different Birks' constants. Saturation can already be seen at the lowest beam density, as the corrected measurements show increased total charge.

charge on the screen was measured while the beam density was increased by shrinking the transverse beam size. While the bunch charge was kept constant, according to the measurement on the screen, the measured charge decreased along the scan by up to 12%. By using different B_{const} from literature [164], the charge density can be corrected in each pixel. The right B_{const} for this material is that which keeps the total charge constant throughout the scan. For the results in this thesis, the value $B_{\text{const}} = 7.1$ mm^{2}pC^{-1} was used, which results in a threshold at 1.5 nC mm^{-2}. With this threshold, the saturation effects are generally negligible, as the beam density is usually well below this threshold*. This is not true for the measurements without plasma interaction, where the full bunch charge is concentrated on a small fraction of the screen. However, the charge measured by beam-position monitors was used in this case.

Rearranging Eq. 4.10, together with B_{const}, allows calculating the charge density of

*As an example, for the images of the plasma-interacted beam in Figs. 5.3(b) and (d), the highest measured charge density is 1.6 pC mm^{-2}.

the beam at the screen, with

$$\frac{d^2Q_{\mathrm{B}}}{dx\,dy} = \frac{\frac{d^2Q}{dx\,dy}}{1 - B_{\mathrm{const}}\frac{d^2Q}{dx\,dy}}. \tag{4.11}$$

4.1.7 Energy calibration

For calibrating a spectrometer in energy, ideally, a beam with varying energy is used in combination with a fixed magnetic field. While ensuring that the beam enters the spectrometer at the same position and angle, the beam's position on the screen can be recorded, giving a direct relationship between energy and position. However, it can be difficult to adjust the beam energy within the desired range without affecting its trajectory, and a different approach might be required.

The position of the beam on the screen is a function of the radius of the bent trajectory, given by the Larmor radius $\rho = \frac{\gamma m v}{eB} = \frac{E}{eB}$. Thus, the position on the screen

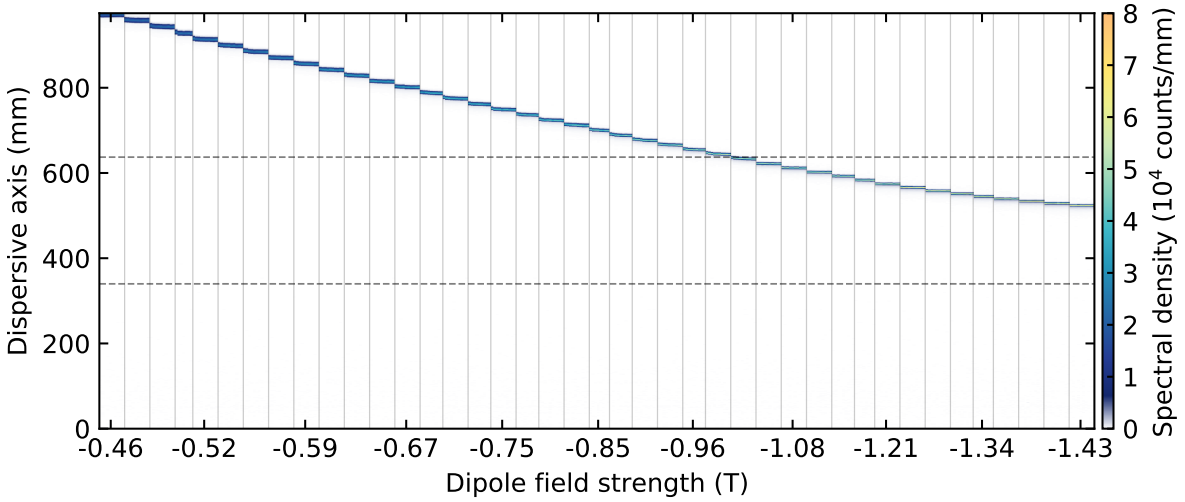

Figure 4.9: Electron bunch spectrum on the spectrometer screen as a function of the dipole field. The field is changed by increasing the dipole current from −278 A to the maximum current of −950 A, where the magnetic field starts to saturate. The vertical gray lines separate different scan steps, and the horizontal dashed lines show the boundary between consecutive cameras.

y can be written as

$$y = f\left(\frac{E}{B}\right). \tag{4.12}$$

The function f can be determined analytically, requiring precise knowledge of the geometry. Another way is to measure the beam's changing position on the screen when the magnetic field strength is scanned with a constant beam energy, as shown in Fig. 4.9. Then, either an appropriate polynomial function can be fitted to the data and inverted such that $E = Bf^{-1}(y)$, or direct interpolation can be used. Within the range of the measured positions, this can be used to calculate the energy corresponding to each position at the screen, given the known magnetic field strength. This method is limited to the range of screen positions that can be reached with the beam: the lowest position depends on the beam energy and the strongest magnetic field. For the beam parameters of the main results presented in this thesis, i.e., chapter 5, the beam does not reach below 524 mm. Therefore, a different approach was undertaken in this thesis.

The spectrometer system was modeled numerically, as shown in Fig. 4.1(a). The positions where particles hit the screen were mapped for a fixed energy and varying magnetic field, recreating the measurement shown in Fig. 4.9. The model is then

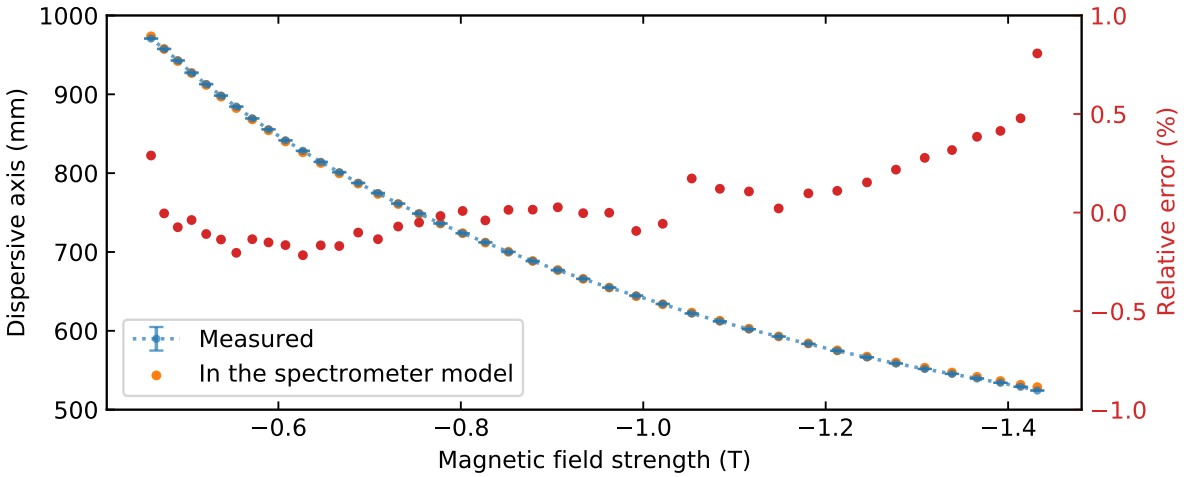

Figure 4.10: Agreement between the position of the beam on the screen in the measurement shown in Fig. 4.9 (blue error bars; mean and rms) and in the numerical spectrometer model (orange). The relative error between these two is shown in red and is below 1%.

compared with the measurement, as in Fig. 4.10, which shows an agreement better than 1%. The model can then be used to calibrate the full screen: using the same magnetic field as in the measurements, the position of particles with different energies on the screen can be calculated.

The spatial axis of the screen is linear, i.e., an image pixel is of constant spatial width. However, the position on the screen does not change linearly with the energy: the pixels shrink in energy range towards lower energies, which effectively lowers the counts – and therefore charge – per bin. To correct for this, the counts on each bin are normalized as follows:

$$\frac{d^2Q_\mathrm{B}}{dx\,dE} = \frac{d^2Q_\mathrm{B}}{dx\,dy}\cdot\frac{dy}{dE}, \tag{4.13}$$

where the factor dy/dE is a list of monotonically decreasing values toward higher energies.

4.1.8 Calibration overview

Eq. 4.14 summarizes the calibration process described in the previous section, and the changes on an example image are shown in Fig. 4.11.

$$\frac{d^2Q}{dx\,dE} = f_\mathrm{Birks}\left(\frac{d^2\,N(\mathrm{px_y})}{\mathrm{px_x\,px_y}}\cdot\underbrace{\frac{\cos\left(\alpha(\mathrm{px_y})\right)}{f_\mathrm{quadr}(\mathrm{px_y})}}_{N(\mathrm{px_y})\to N_{\gamma\alpha}}\cdot\frac{\mathrm{px_x\,px_y}}{dx\,dy}\cdot\frac{dQ}{dN_{\gamma\alpha}}\right)\cdot\frac{dy}{dE}, \tag{4.14}$$

where f_Birks is the function correcting for scintillator saturation as defined with Eq. 4.11.

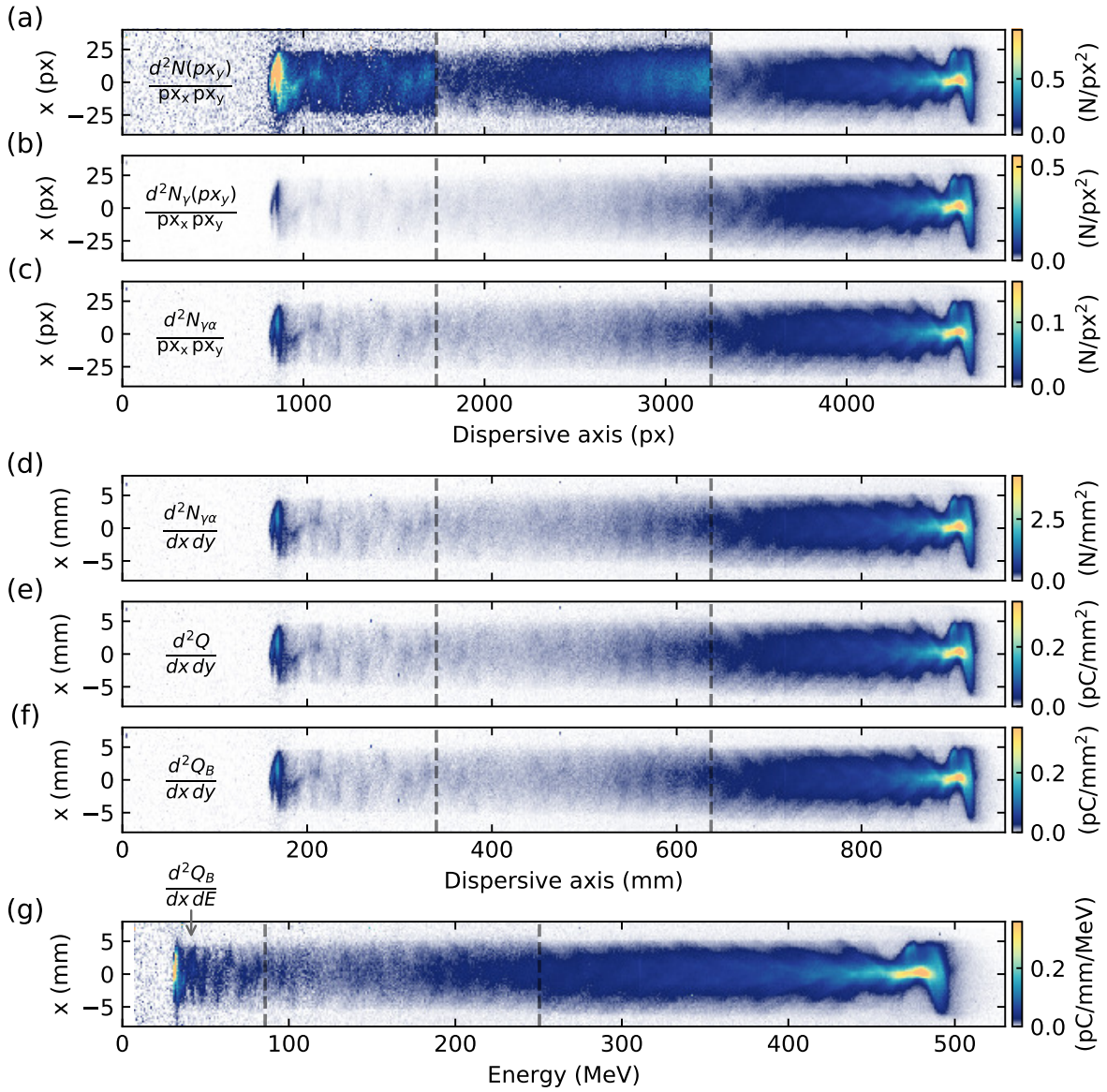

Figure 4.11: Sample image of the spectrometer for each step in the calibration process as described in Sec. 4.1, where (a) shows the initial image, and the others are corrected consecutively for: (b) the photon-capture efficiency with Eq. 4.4, (c) the incident angle on the scintillator with Eq. 4.6, (d) the applied spatial calibration with Eq. 4.8, (e) the applied charge calibration with Eq. 4.9, (f) correcting for scintillator saturation with Eq. 4.11, and (g) the applied energy calibration with Eq. 4.13. To allow for comparison between the images, the color map is scaled in each image such that they all show the same color at the highest density at the right of the screen, i.e. high energy. The vertical dashed gray lines show the boundary between consecutive cameras. In this figure, N is scaled down by the factor 1×10^{-3}.

4.2 Beam-quality preservation with high energy-extraction efficiency

Using the experimental facility described in Sec. 3, an electron beam was divided longitudinally to a driver-witness pair and focused down to a transverse size of 4.9 µm at the plasma entrance of the 50-mm-long cell. Further beam parameters are shown in Table 4.1.

The beam size of the trailing bunch around the waist, imaged on the high-resolution spectrometer, is shown in Fig. 4.12. A least-squares fit of Eq. 2.13 yields a 2.85 ± 0.07 mm mrad projected emittance at the cell entrance in the horizontal axis. As the other axis is the dispersive axis, the corresponding emittance could not be measured but is usually similar. When enabling the electrical discharge, the bunch pair propagates through the plasma and the acceleration takes place. Once at the cell exit, the trailing bunch transverse size increases as it diverges. Imaging the beam around the exit shows a virtual waist, with which the emittance can be measured in the same manner as at the entrance. For this working point, the emittance after acceleration was preserved within the measurement error. The charge and relative energy spread, with histograms in Figs. 4.12(d–e), were also preserved within the central 68-percentile range for 41%

Drive bunch

Parameter	Value	Unit
Charge	400	pC
Mean energy	1050	MeV
Length	150	fs
Peak current	1.0	kA

Trailing bunch

Parameter	Value	Unit
Charge	40	pC
Mean energy	1059	MeV
Length	37	fs
Average current	0.44	kA
Transverse emittance	2.79	mm mrad
Waist beta function	16	mm

Table 4.1: Measured incoming bunch parameters. The transverse emittance was only measured in the horizontal (x) axis, but the beam is usually symmetric. Values extracted from Ref. [160].

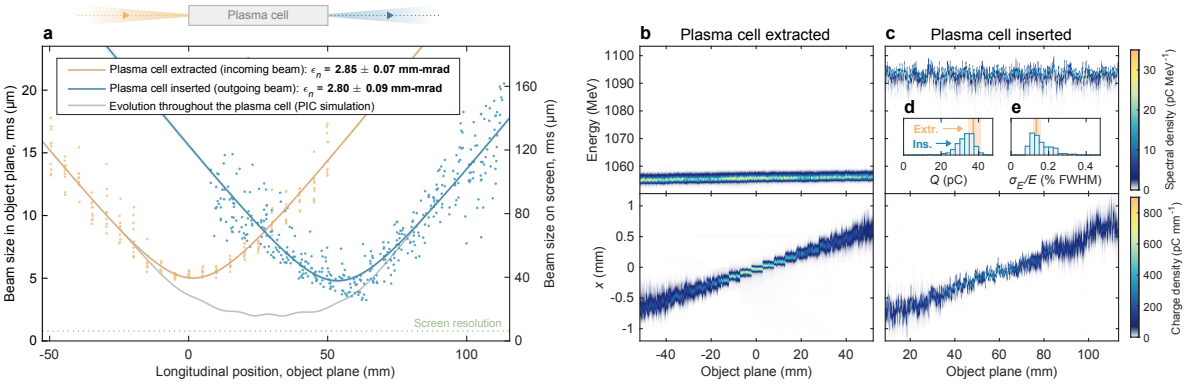

Figure 4.12: (a) Trailing bunch transverse size near the waist, when the plasma cell was extracted (orange points) and after plasma acceleration (blue points). The lines with the same colors correspond to the fitted beam size following Eq. 2.13. The beam size within the plasma is estimated with a PIC simulation (gray line). Projection on the energy (top) and transverse (bottom) axis for the beam when the plasma cell was extracted (b) and accelerated through plasma (c). Histogram of the bunch's charge (d) and energy spread (e). In orange, the average (line) and 68$^{\text{th}}$ percentile (band) for the non-interacted bunch. Figure from Ref. [160].

and 62% of all measurements, respectively.

The trailing bunch with 40 pC of charge was accelerated by up to 40 MeV in the 50-mm long cell. This corresponds to a longitudinally averaged accelerating gradient of 0.8 GV/m, and, according to simulations recreating the experiment, a peak of 1.4 GV/m. While the energy gain can be considered modest, this result shows that effects such as nonlinear focusing or nonuniform accelerating fields, mismatching, Coulomb scattering, and transverse misalignment are successfully mitigated and do not degrade the emittance. As transverse instabilities such as hosing or beam breakup develop gradually with propagation distance, simulations closely matching the experimental results were performed with the PIC code HiPACE++ [80]. This allows extending the plasma length by 500 mm and accelerating the trailing bunch to ∼650 MeV. In this simulation, the emittance in the horizontal plane continued preserved.

In Ref. [160], to show the sensitivity of emittance preservation to the alignment, this parameter is scanned around the optimum, where the emittance at each setting is measured as in Fig. 4.12. The scan was performed by adjusting the strength of a

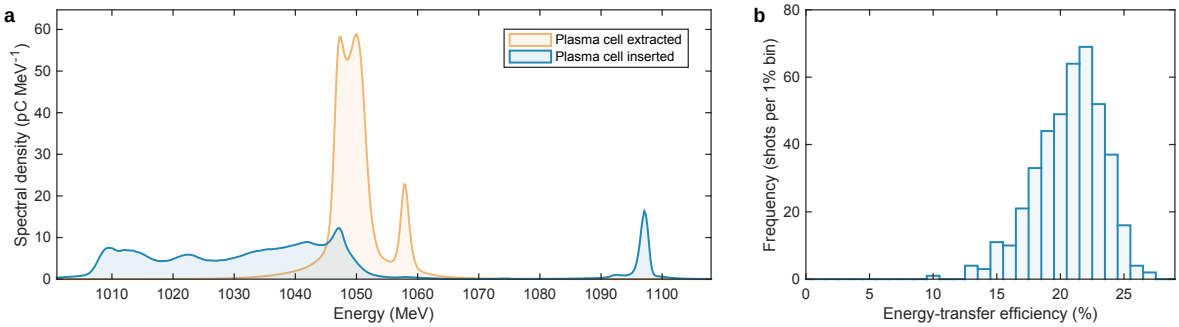

Figure 4.13: (a) Energy spectrum of the driver (lower energy) and witness (higher energy) bunches, with the plasma cell extracted (orange) and inserted (blue). The spectrum of the driver after interaction with plasma is reconstructed with an imaging energy scan, with a more detailed description of this procedure in Sec. 5.2.1. (b) Histogram of the plasma-to-trailing-bunch energy-transfer efficiency, i.e., Eq. 2.32. The energy deposition is determined with the average reconstructed driver spectrum; the deposition with the shot-to-shot well-imaged trailing bunch spectrum. Figure from Ref. [160].

quadrupole magnet (±1.5%) in a beamline section with horizontal dispersion, using the fact that the energy of the two bunches was slightly different (0.9%)*. It is shown that the emittance grows with the alignment away from the optimum and is sensitive to a 0.5 mrad misalignment in this experimental setup.

While Fig. 4.12 shows emittance-preserving acceleration, it does not show the energy-transfer efficiency of this process. For this, Fig. 4.13(a) shows the energy spectra of the bunches with and without plasma interaction, which allows computing the energy deposited by the driver and the energy extracted by the trailing bunch. Fig. 4.13(b) shows a histogram of the energy-extraction efficiency, where Eq. 2.32 was used. The efficiency ranges from 10–27% and peaks at (22 ± 2)%, where the error quoted arises from the reconstructed† plasma-interacted driver spectrum showing 20% less total charge than the cell-extracted spectrum. While in these results, only the beam quality preservation and not the energy-transfer efficiency was optimized, the efficiency achieved is similar in magnitude to previous experimental results, i.e., 30% and 42% [104, 144].

*This adjustment also affects the beam-waist location and waist beta function. However, for such small changes and a small beam size at the quadrupole magnet, these only changed within a 2–7 mm and ±25% range, respectively.

†This method is discussed in detail in Sec. 5.2.1.

4.3 Efficiency limitation by instabilities

Theory and simulations suggest that the energy-transfer efficiency from the plasma to the trailing bunch can be high, with up to 90% [100, 145, 146]. However, in Ref. [167], an efficiency-instability relation is presented, where a higher energy-extraction efficiency leads to the beam break-up instability. This interplay is described with

$$\eta_t \approx \frac{\eta_{p\to w}^2}{4(1-\eta_{p\to w})}, \tag{4.15}$$

where η_t is the ratio of the wake-deflecting force to the focusing force, and, in its essence, describes how susceptible the interaction is to the buildup of the transverse instability. While this was later partly challenged in Ref. [168], this instability could become a limitation for energy-transfer efficiency. This could be problematic, especially for future high-beam-power facilities, where energy gain and transfer efficiency will be maximized to lower the environmental footprint, running costs, and required cell cooling. For this reason, the instability – as well as a possible damping mechanism – is briefly discussed.

If a trailing bunch is misaligned or tilted within a wakefield, the off-axis particles will experience a transverse force toward the wakefield center. However, as the trailing bunch affects the plasma blowout with its charge, it will also change the wakefields, allowing for a resonant exponential growth of the particles' transverse position. This instability is generally referred to as beam break-up [151] or hose [152] instability. A method to mitigate this instability is by suppressing the resonance [169]. This can be done through BNS damping, after Balakin, Novokhatsky, and Smirnov [170]: an energy chirp along the bunch results in different slices oscillating at different frequencies. This method conflicts with the low-energy-spread requirement of applications. However, as manipulation of the energy spread with plasma accelerators has been shown [148–150], one could envisage accelerating a trailing bunch with an energy chirp and subsequently removing it before delivery to the application. The resonance can also be broken by the movement of

plasma ions, often assumed immobile, as they would change the focusing strength along the trailing bunch and lead to differing oscillation frequencies [171]. However, such non-linear focusing fields will spoil the emittance. In summary, mitigation of the beam break-up instability could require a combination of different strategies, as they each come with drawbacks. Understanding the onset of instabilities is key to experimentally developing successful strategies for their mitigation. To this end, a novel diagnostic method is presented in the following section.

4.4 Measuring the energy efficiency with longitudinal resolution and potentially the onset of instabilities

Until now, destructive diagnostics such as screens on energy spectrometers have been used to identify and measure instabilities, or the instabilities are inferred from a lost beam. However, in Ref [136], a correlation was established between the plasma-emitted light intensity after interaction with the beam and the beam-energy loss. Such a correlation can be used to measure the energy-extraction efficiency of an accelerating bunch. In the following paragraphs, an overview of this method is given.

Fig. 4.14(e) shows, compared to (d), that the plasma-light intensity increases with energy deposition of a drive bunch. Adding a trailing bunch that is accelerated results in less light emitted, as can be seen in Fig. 4.14(f). The scaling of the plasma light depending on how much energy remains after the beam–plasma interaction is measured in Ref. [137]. There, it is shown that, for the region where the correlation is linear, the linear slopes of increasing driver or trailing charge are approximately equal and of opposite sign. This suggests that the light yield is only dependent on the energy remaining after the beam–plasma interaction, irrespective if only energy was deposited or partly extracted, as long as the remaining energy is the same. It is demonstrated in Ref. [137] that it suffices to calibrate the light yield with the energy deposited in the

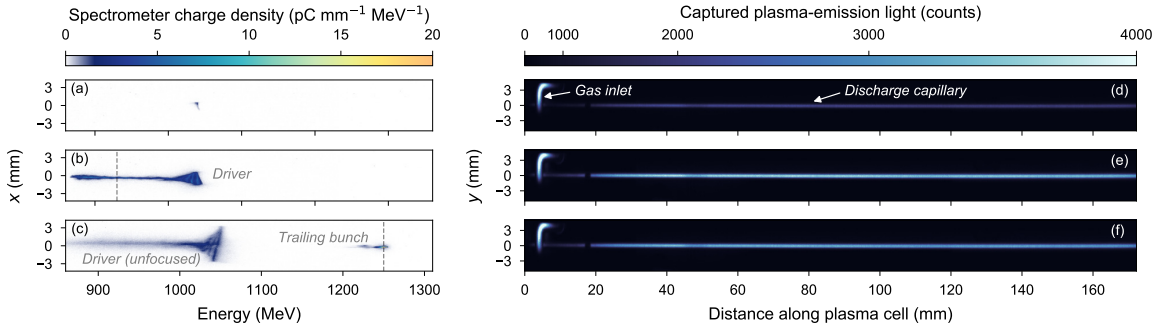

Figure 4.14: On the left are images of the spectrometer with (a) negligible driver charge, (b) a plasma-interacted 368 pC driver, and (c) the same driver together with an accelerated trailing bunch of 47 pC. The gray dashed lines show the imaging energy. On the right are images (d–f) with the recorded plasma light emitted a few microseconds after the beam–plasma interaction, for the corresponding measurements on the left, where, to better showcase the differences, a quadratic color scale is used. Figure from Ref. [137].

plasma, e.g., with an energy spectrometer, to measure the energy-extraction efficiency – if the energy deposited by the driver is known.

As the light yield can be measured along the plasma column, assuming that this energy-dependent light-emission process is local*, one can subdivide the measurement into different sections along the column, allowing for a longitudinally resolved measurement. Fig. 4.15(b) shows the evolution of the trailing-bunch extraction efficiency along the plasma, for two separate interactions. Both show a rise in efficiency at the beginning of the cell. This is caused by the plasma density rising and reaching the central flattop density for which the interaction was optimized. One measurement shows an efficiency peak at 58% and is followed by a steep decline (0.23% mm^{-1}); the other, with a later peak of 54%, shows a slower efficiency decline (0.11% mm^{-1}). On average, as measured on the spectrometer, the efficiency is 38% and 16%, and the charge of the trailing bunches is 38% and 98%, respectively. While both measurements were performed under unchanged parameters, variations from the jitter were enough to strongly affect the average energy efficiency and the charge reaching the spectrometer. This is consistent

*This assumption is validated later in Sec. 5.1 with Fig. 5.3(f–g). An upper bound for the longitudinal resolution is 11 mm.

with the growth of a transverse instability. However, these measurements do not prove the development of an instability by themselves: they show a change in the beam–plasma interaction across an approximately constant density, which could be caused by an instability. More development in this technique is required to confirm this hypothesis, but such a simple diagnostic could be used to study the rise and evolution of instabilities by their effect on energy-extraction efficiency. Furthermore, for an accelerator consisting of multiple plasma stages, this technique could be used for simultaneous non-destructive optimization at each stage.

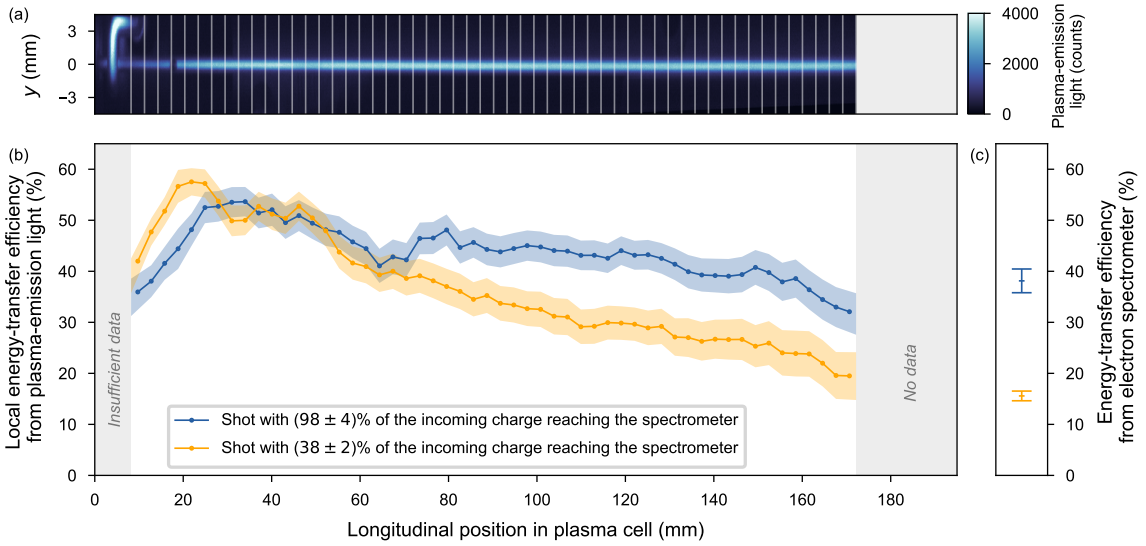

Figure 4.15: (a) Plasma light emitted after a beam–plasma interaction. The distinct shape on the very left is from a gas inlet, and the dark spot at 20 mm from a transverse hole in the capillary (see Fig. 3.3). (b) The energy-extraction efficiency along the plasma length. The error band shows the uncertainty from the fitted energy-light response and jitter in driver energy loss. (c) Longitudinally-averaged energy-extraction efficiency measured at the energy spectrometer for the two beams shown in (b). Figure from Ref. [137].

4.5 Conclusions

Demonstration of emittance preservation is a significant milestone: if beam quality preservation were not possible, it would bar their use in colliders and FELs. Furthermore, as this was demonstrated with an energy-extraction efficiency of 22%, it shows that both can be performed simultaneously and are not mutually exclusive for these parameters.

In the experimental results presented in Sec. 4.2, the emittance is of $\mathcal{O}$(mm mrad), and the relative energy spread of $\mathcal{O}(0.1\%)$, which is compatible with the requirements of FELs and puts plasma accelerators at the doorstep for implementation as energy boosters. There are, however, several caveats to this statement. First, the energy gain must be larger to enable FELs to reach energies beyond their capability. For this, instead of increasing the accelerating gradient, which would carry tighter tolerances and adapting the beam parameters, the plasma should be lengthened. However, this also gives the hose [152] and beam break-up [151] instabilities more time to develop. Tolerance studies must be performed to estimate better any limitations caused by these instabilities. Second, simulations suggest that, for the plane that was not measured, the emittance was also preserved [160]. This should be demonstrated experimentally. Third, due to the low driver-to-trailing-bunch efficiency (0.6%), the accelerator would probably have to operate at a lower repetition rate to keep the heat load on the driver beam dumps manageable. Once higher efficiency is established and high-repetition-rate operation of plasma accelerators is demonstrated, the average beam power delivered could be scaled up.

The requirements are tighter for particle colliders, mainly due to the beams' lower emittance, which can be down to 0.01 mm mrad in one plane. At this level, it is not clear that the emittance can be preserved, as processes such as Coulomb scattering of the beam particles with recombined background gas or plasma ions could spoil the emittance. It is shown in Ref. [172, Sec. 2.3.1] that the emittance growth through this process scales approximately with the squared atomic number of the gas species used, and, with

hydrogen, a 1 TeV bunch will have its emittance grow by 0.001 mm mrad. Therefore, demonstration of emittance preservation at these values must be demonstrated.

Chapter 5

Driver-depletion efficiency

The result with the high energy-extraction efficiency [160] reported in the previous section is an important milestone for demonstrating the suitability of plasma accelerators in colliders and FELs. However, in this experiment, the energy of the driver remained largely unused, as only ∼1.7% was deposited.

As discussed in Sec. 1, for high beam-power machines, disposing of such large energies would lead to significant environmental and financial detriment, and might become technically challenging for the driver beam dumps. The following presents a selection of previous experimental results with notable energy deposition.

Strongly energy-depleted driver electrons were reported in 2007 [105], where a single long electron bunch was used, with the front driving the wakefield and the charge at the back being accelerated. While the initial energy was 42 GeV, some electrons were reported to reach 5–7 GeV, which, for those individual electrons, would be an energy loss of ∼86%, though significantly less for the average of all driver electrons. In 2014 [144], a 2.1% energy deposition of the drive bunch can be inferred with Eq. 2.34 and from the bunch parameters and energy-extraction efficiency reported. Within the same experiment but using positrons instead of electrons, another publication in 2015 [87] also reported significant energy deposition. Here, a bunch with an initial energy of 45.6 J deposited 2.54 J into the plasma. As approximately 10% of its charge was accelerated,

assuming that all the remaining charge drove the wakefields, the driving charge deposited 5.9% of its energy. While these results showed energy deposition into the plasma, using a single long bunch as a driver and trailing bunch simultaneously is not usable for applications such as colliders and FELs. Well-defined and low-energy spread bunches are required there. Following this requirement, new results were published in 2021 [104], demonstrating an energy-extraction efficiency of $(42 \pm 4)\%$, with the same experimental setup as in this thesis. Here, a 490 pC electron bunch deposited $\sim$1.8%* of its energy into the plasma. In summary, experimentally, more than 90% of the driver energy is unused in the literature.

This chapter presents the main experimental result of this thesis: the demonstration of high driver-to-plasma energy-transfer efficiency. This can be limited by the process of electron re-acceleration, where energy-depleted driver electrons slip back in phase and are accelerated [174], which is reportedly seen experimentally in Ref. [175]. This mechanism is first investigated with simulations and subsequently measured and compared to theory. To measure the energy deposited at this limit, an average spectrum is reconstructed to account for imaging complications. Then, as the uncertainty in depletion efficiency is dominated by driver-charge loss, a model is constructed to allow for a better estimate. The result is then compared to the maximum predicted by simulations in the literature, and possible limitations and strategies to reach these experimentally are discussed.

5.1 Observation of electron re-acceleration

5.1.1 Simulation results

The propagation of an electron bunch through a plasma is simulated with the HiPACE++ PIC code (see Sec. 2.3) to investigate the evolution of the driver. The simulation and

*With the average energy of the driver at 1027.3 MeV and 1008.4 MeV, before and after plasma interaction, respectively [173], and assuming no charge loss.

beam parameters are shown in Tables 5.1 and 5.2, respectively. The beam is focused into the plasma with a transverse size of 17 µm rms in the horizontal and vertical plane, and the longitudinal plasma profile is shown in Fig. 5.1(a).

Figs. 5.1(g–i) show that the electrons, while losing energy, remain at the same longitudinal position, i.e., the same phase of the wakefields. However, once the electrons reach low energies, they become non-relativistic and start lagging behind the other relativistic electrons [Fig. 5.1(j)]. As soon as the slower electrons slip back enough to reach the accelerating phase, they are accelerated. Once they reach relativistic energies, they become locked in phase again [Fig. 5.1(k)]. Once this *re-acceleration* process starts, a steady stream of electrons moving from the head to the back reduces the charge driving the wakefields. This alters the wakefield structure and could lead to the linear regime, in which the emittance cannot be preserved (see Sec. 2.4.1). At the same time, the re-accelerated charge alters the accelerating field through beam-loading. As discussed in Sec. 2.4, if a trailing bunch doesn't experience a flat accelerating field on average throughout the plasma interaction, its energy spread will increase. Also, any non-relativistic charge within the trailing bunch will alter, through space charge, the focusing field and make it non-linear, which leads to emittance growth [97]. As re-acceleration must be avoided to preserve the trailing-bunch energy spread and emittance, it limits the energy deposition and the overall energy-transfer efficiency of a plasma accelerator stage.

It should be noted that the simulation code HiPACE++ [80] relies on the quasistatic approximation to significantly lower the computational costs, requiring that the bunch particles are relativistic (see Sec. 2.3). As, for some time, the charge slipping backward in phase is non-relativistic, this approximation might not be valid, and the result may be affected. To investigate this, two simulations with the same bunch and plasma parameters were performed, where one used the HiPACE++ code, and the other the full electromagnetic PIC code FBPIC [179]. The latter code does not rely on the quasistatic assumption, and, instead of 3D like HiPACE++, is a '*quasi*-3D' algorithm, with an

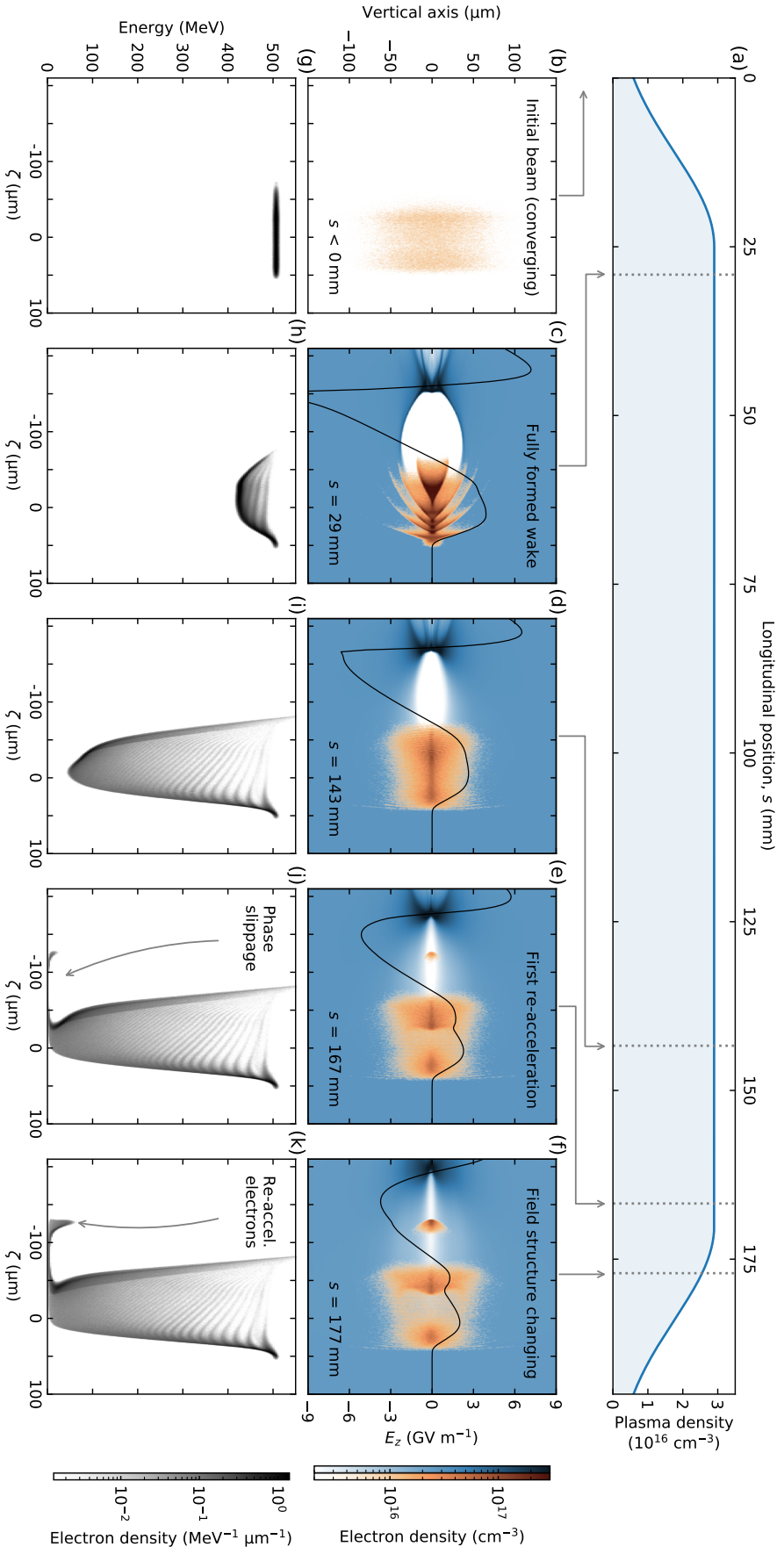

Figure 5.1: (a) The longitudinal plasma profile over 195 mm, consisting of a central flattop at 2.9×10^{16} cm^{-3}, with Gaussian up and down ramps starting 25 mm into the cell and an rms of 14 mm. (b–f) Show the density of plasma and beam electrons (blue and orange color maps, respectively) and the on-axis longitudinal electric field E_z (black line). The corresponding longitudinal phase spaces are shown in (g–k). Driver electrons lose energy while locked in phase (g–i) until the electrons are depleted in energy and become non-relativistic, at which point they slip backward in phase (j) and are re-accelerated (k). Figure from Ref. [176].

Parameter	Value	Unit
Simulation box ($x \times y \times \zeta$)	500×500×650	µm×µm×µm
Number of grid cells ($x \times y \times \zeta$)	511×511×2048	–
Number of plasma particles ($N_{p,x} \times N_{p,y}$)	2×2	–
Number of beam particles	5×10^6	–
Simulation length	200	mm
Time step	$\Delta t_{\text{adaptive}}$	s

Table 5.1: Simulation parameters for high driver-energy depletion. The adaptive time step is defined with $\Delta t_{\text{adaptive}} = \frac{2\pi}{N\omega_\beta}$, with the betatron frequency $\omega_\beta = \omega_{pe}/\sqrt{2\gamma}$, and γ as the average Lorentz factor for the slowest particles. N is the number of time steps per betatron period, which in this simulation was 20.

Parameter	Value	Unit
Charge	636	pC
Mean energy	501	MeV
Energy spread	2.35	MeV rms
Length	83	fs rms
Transverse emittance	30	mm mrad
Waist beta function	10	mm
Waist location	30	mm

Table 5.2: Measured driver parameters for high energy depletion. The waist location is relative to the cell entrance, and a positive value is downstream of it. The bunch is assumed transversely symmetric, and the waist beta function and location were estimated from the bunch position jitter, with the method described in Ref. [177]. The shape of the bunch current at the TDS downstream of the plasma is measured in Fig. 3.8. The total bunch charge is lower there than at the plasma entrance due to charge loss in transport to the TDS. The current used for the simulation is the measured current scaled up to match the initial bunch charge, assuming that the charge was lost uniformly across the bunch.

FBPIC		
Parameter	Value	Unit
Simulation box ($z\times r$)	360×350	µm×µm×µm
Number of grid cells ($z\times r$)	4096×1500	–
Number of plasma particles ($N_{p,z}\times N_{p,r}\times N_{p,\theta}$)	2×2×6	–
Number of modes	1	–
Number of beam particles	1×10^6	–
Bunch charge	443	pC
Simulation length	225	mm
Time step	Δt_γ	s
HiPACE++		
Parameter	Value	Unit
Simulation box ($x\times y\times\zeta$)	700×700×360	µm×µm×µm
Number of grid cells ($x\times y\times\zeta$)	4095×4095×3072	–
Number of plasma particles ($N_{p,x}\times N_{p,y}$)	1×1	–
Number of beam particles	1×10^7	–
Bunch charge	443	pC
Simulation length	225	mm
Time step	$\Delta t_{\text{adaptive}}$	s

Table 5.3: Simulation parameters for the comparison between FBPIC and HIPACE++, where the adaptive time-step of the latter is defined in the caption of Table 5.1, with $N = 10$. The FBPIC simulation was run in the boosted frame [178, 179] with $\gamma = 5$, and Δt_γ was set to the Courant-Friedrichs-Lewy (CFL) [180] condition limit. In both simulations, the longitudinal plasma-density profile consisted of a cosine up-ramp of 25 mm from 10^{14} cm^{-3} to the plateau density of 3.7×10^{16} cm^{-3}.

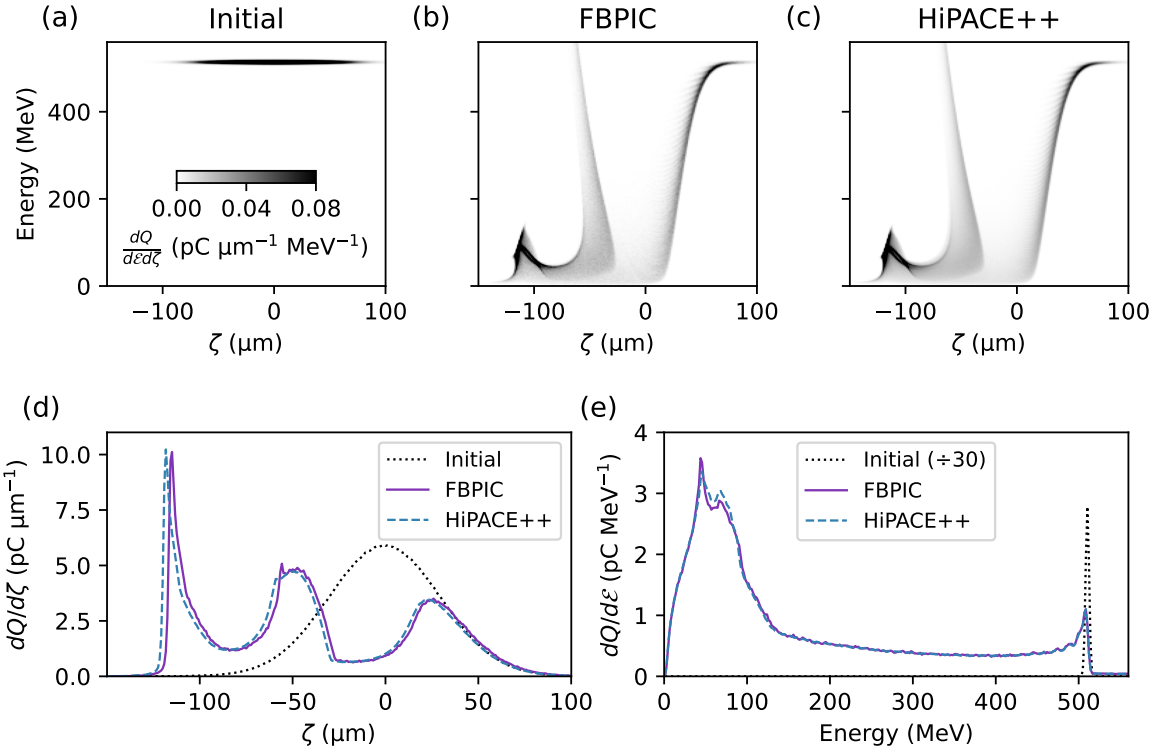

Figure 5.2: Longitudinal phase-space of the drive bunch before (a) and after plasma interaction, where the simulation was run with FBPIC (b) and HiPACE++ (c). For direct comparison, the longitudinal charge distribution (d) and energy spectra (e). The simulation parameters are shown in Table 5.3. The simulations for this comparison were run by M. Thévenet; Figure from Ref. [176].

r-z geometry and azimuthal mode decomposition. Such geometry is suitable for this simulation, as it has approximately cylindrical symmetry. The simulation parameters are shown in Table 5.3. It should be noted that these parameters differ from those used for the rest of this chapter's HiPACE++ simulations, mainly in bunch charge and transverse size. Therefore, the simulations are adequate for comparing PIC codes with re-acceleration but should not be used to interpret the experimental results qualitatively. Fig. 5.2 shows the bunch after the plasma interaction for both codes, and only small differences can be seen. Therefore, it can be concluded that HiPACE++ can capture the re-acceleration process well. This could be because, at any time, only a small fraction of charge is non-relativistic, having a negligible effect on the wakefield structure and the quasistatic assumption.

5.1.2 Experimental results

To investigate different degrees of energy deposition, in a simulation, one can analyze the bunch at different propagation lengths. However, recreating this experimentally requires changing the plasma length for each measurement, which can be technically challenging. While this was achieved at a different experiment with a custom cell design [181], this was not done in the experimental setup described in this thesis. Instead, for a fixed cell length of 195 mm, the energy-deposition rate is changed by adjusting the plasma density. Following Eqs. 2.24 and 2.26, the longitudinal field increases together with the plasma density. However, higher plasma densities also shrink the size of the blowout bubble as the plasma wavelength decreases. To ensure that the driver electrons are only placed in the decelerating region of the wakefield, the bunch-length rms should be no longer than the plasma skin depth, i.e., $\sigma_z k_p < 1$. Therefore, following Eq. 2.2, a bunch with a length of 83 fs rms is restricted to a maximum plasma density of $\sim 4 \times 10^{16}$ cm^{-3}, which has a skin depth of 27 µm or 89 fs. For the remainder of this chapter, the experimental results were achieved with the beam parameters shown in Table 5.2.

Fig. 5.3(c) shows the driver energy spectrum at different degrees of depletion, by scanning the plasma density. While the bunch enters the plasma at an average energy of 501 MeV [see Fig. 5.3(a)], at the density $\sim 7 \times 10^{15}$ cm^{-3} [see Fig. 5.3(b)], some electrons exit with 200 MeV, having deposited up to 301 MeV into the plasma. The higher the density, the more energy is deposited into the plasma and the lower the energy at which the electrons exit. At the density $\sim 1.5 \times 10^{16}$ cm^{-3}, the electrons go below 12 MeV, which is the spectrometer's measurement limit. By further increasing the density, a distinct peak in charge moves up in energy, and more charge is accelerated. This is consistent with the re-acceleration shown in Fig. 5.1. We note that the accelerated charge does not originate from the driver being too long and extending to the accelerating field, as it is short enough with 83 ± 3 fs rms length. Furthermore, if the bunch were too long, the accelerated electrons would be accelerated starting from their initial energy,

and Fig. 5.3 shows no charge beyond 501 MeV.

As shown in Sec. 4.4 with Fig. 4.14, the intensity of light emitted by the plasma is a function of the energy deposited during the beam–plasma interaction. For Figs. 5.3(e–g), the plasma light emitted after the interaction was recorded. As the emitted light is also dependent on the plasma density, the relative time between the electrical discharge and the camera trigger was kept constant by adjusting the camera timing*. This, in turn, increases the time delay between the beam–plasma interaction and the image acquisition at higher densities. The additional energy deposited has more time to dissipate, which can explain why the light intensity is approximately constant throughout the scan.

In addition to those arising from reflections and vignetting, some features can be seen in Fig. 5.3(f). The horizontal line at 20 mm is from a narrow hole to allow the introduction of a perpendicular-propagating laser pulse for a separate plasma injection experiment [130]. Also, at the entry and exit of the plasma cell, the density is lower [see Fig. 5.1(a)]. Therefore, the wakefields are weaker, and less energy is deposited, which leads to less light emitted locally. Fig. 5.3(f) shows that the longitudinal plasma-light profile remains approximately constant up to around 1.5×10^{16} cm^{-3}. From there on, a significant drop in light intensity appears at the downstream end of the plasma cell and gradually moves upstream with higher density. This decreased signal is consistent with driver-electron re-acceleration for two reasons: less charge drives and deposits energy into the wakefields, and the re-accelerating charge extracts energy.

The longitudinal position where the signal lessens marks the start of the re-acceleration process, which allows estimating the strength of the wakefields. As an example, for the density of 3.5×10^{16} cm^{-3} [see Fig. 5.3(d) and (g)], the driver electrons with initially 501 MeV are energy depleted within the first 115 mm of plasma, and are accelerated to 180 MeV in the last 80 mm. Therefore, the average decelerating and accelerating fields are 4.4 GV/m and 2.3 GV/m, respectively.

*An overview schematic of the trigger system, plasma decay, and discharge current is shown in Fig. 3.5.

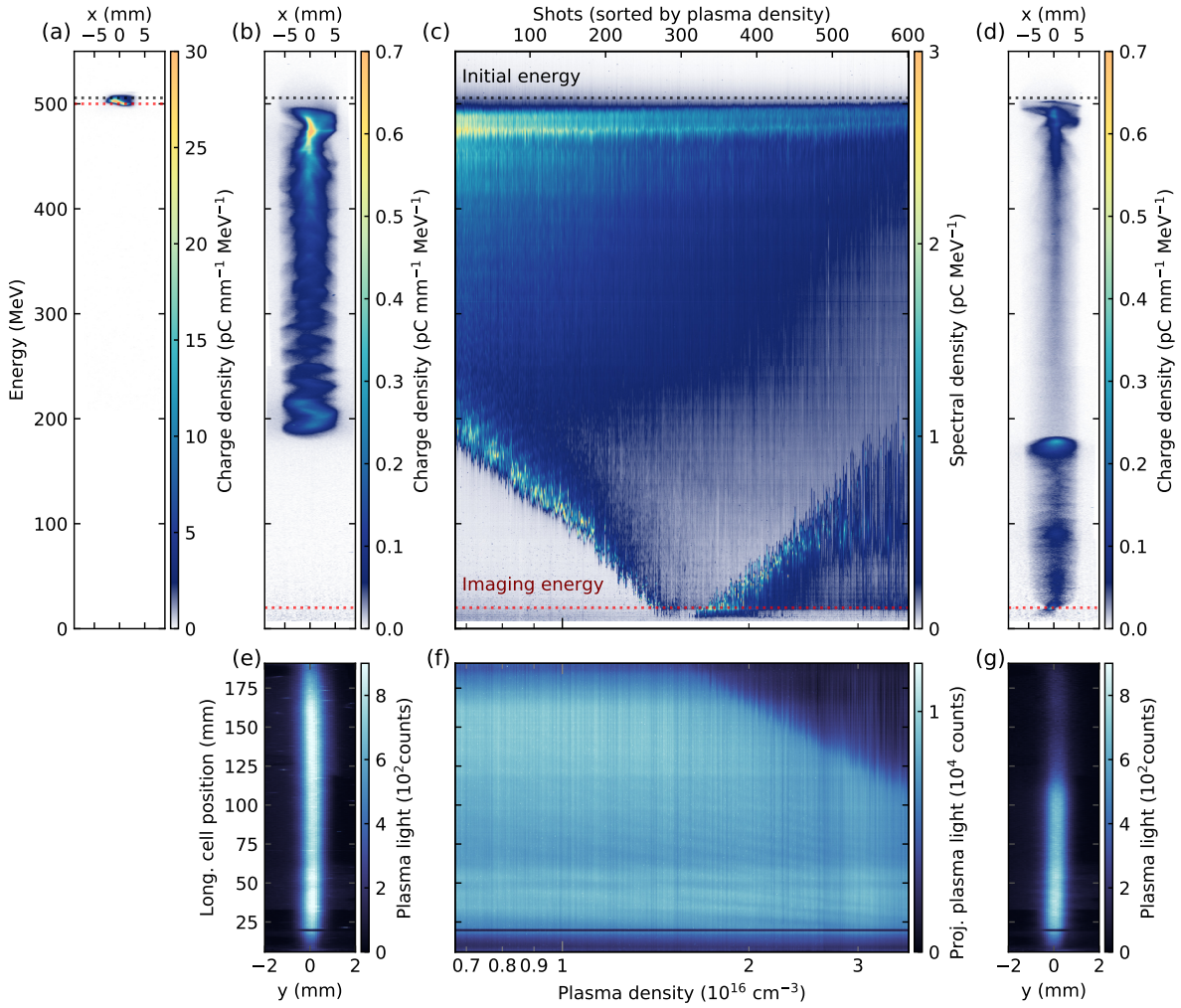

Figure 5.3: Spectrometer images of the drive bunch, where no plasma is present (a), at $\sim 7 \times 10^{15}$ cm^{-3} (b) and $\sim 3.5 \times 10^{16}$ cm^{-3} (d). (c) Energy spectra for a scan of plasma density. The dashed black and red lines show the initial beam and imaging energy, respectively. (e, g) Plasma light emitted along the plasma cell from $s = 6$ to 191 mm downstream from the plasma entrance, for the same data as in (b) and (d), respectively. (f) Plasma light projected onto the longitudinal axis (i.e., along the plasma cell) for the corresponding shots in (c). Figure adapted from Ref. [176].

To estimate how quickly the signal drops longitudinally, the *error function* can be fitted to all the measurements with re-acceleration in Fig. 5.3(f), yielding $\sigma = (11 \pm 2)$ mm. This shows that the dependency of the photon-emission intensity on the beam-energy deposition is a local effect, verifying the assumption made in Chapter 4.4 for Fig. 4.15(b) and placing an upper bound in resolution for the longitudinally-resolved energy-extraction efficiency.

5.1.3 Comparison to theory

The theory developed by Lu *et al.* [99] (see Sec. 2.4.2) can be used to predict at which density the electron-re-acceleration process should start, which can then be compared to that measured in Fig. 5.3.

The decelerating field required to energy-deplete the driver electrons is given by

$$E_{z,\,\mathrm{decel}} = \frac{U_{\mathrm{driver}}}{eL_{\mathrm{plasma}}}, \tag{5.1}$$

where U_{driver} is the initial driver energy (501 MeV), and L_{plasma} is the plasma length, which can be approximated with the flattop-density length of 145 mm [see Fig. 5.1(a)].

Assuming that the bunch has a Gaussian shape, with its total charge of $Q = 636$ pC and a length $\sigma_t = 83$ fs rms, the peak bunch current is $I_b = \frac{Q}{\sqrt{2\pi}\sigma_t} \approx 3$ kA. This current leads, with Eqs. 2.27 and 2.29, to a a maximum accelerating field of

$$E_{z,\,\mathrm{max}} = \frac{2I_b}{I_A} \ln\left(\frac{1}{\sqrt{\frac{2I_b}{I_A}/5.3}}\right) E_0 \approx 0.48 E_0, \tag{5.2}$$

with I_A as the Alfvén current of ∼17 kA, and E_0 as the wave-breaking field defined with Eq. 2.26. At the plasma density used in the simulation for Fig. 5.1, i.e., 2.9×10^{16} cm^{-3}, this yields an accelerating field of ∼7.8 GV/m, which is consistent with Fig. 5.1(c). In the same Figure, the peak decelerating field is approximately 4 GV/m, and therefore $E_{z,\,\mathrm{max}} \approx 1.95 E_{z,\,\mathrm{decel}}$. Inserting this into Eq. 5.1, together with Eq. 5.2, the plasma

density with the onset of re-acceleration is

$$n_p \approx \frac{\epsilon_0}{m_e c^2}\left(\frac{1.95 U_{\text{driver}}}{e L_{\text{plasma}}}\frac{1}{0.48}\right)^2, \tag{5.3}$$

which yields a plasma density of 2.1×10^{16} cm^{-3}, where the density at which re-acceleration was measured in Fig. 5.3 is $\sim 1.5 \times 10^{16}$ cm^{-3}. The discrepancy can arise from approximating the ratio of the peak decelerating and accelerating fields. In the weakly-driven blowout regime, their magnitude is approximately equal as the longitudinal field is approximately sinusoidal [99]. However, according to the simulations, this is not the case in the wakefields driven in this measurement. Furthermore, Figs. 5.1(c) and (d) show that the wakefield structure evolves, as the peak decelerating field decreases from $\sim$4 GV/m to $\sim$2.6 GV/m. This is possibly due to head erosion [105], where bunch slices, at the very front where the focusing fields have not fully formed, diverge and decrease the peak beam density. This process effectively lessens the strength of the wakefields driven. Nevertheless, the estimate based on theory yields a density within a factor of two to the one measured in the experiment.

5.2 Driver energy-depletion efficiency

To determine the driver-depletion efficiency as defined with Eq. 2.31, an accurately measured energy spectrum is required. While Fig. 5.3 can be used to draw the qualitative conclusion that re-acceleration has been measured, it is not good enough to estimate the overall energy of the bunch after the interaction, for two reasons. First, in Figs. 5.3(b–d), the imaging optics were set to properly image electrons at 20 MeV, leading to particles at higher energies in the spectrum being badly imaged. Second, some charge is lost in transport from the plasma exit to the diagnostic, introducing uncertainty in estimating the energy deposited into the plasma. In the following two sections, these two effects are treated such that the bunch energy spectrum at the plasma exit can be constructed

and used to estimate the driver depletion efficiency.

5.2.1 Point-to-point imaging

Point-to-point imaging ensures that the position at which particles hit the screen is independent of the angle with which they exit the plasma (see Sec. 2.2.5). This is limited to a certain range of energies for the same principle by which the energy spectrometer works: particles with different energies are deflected differently by a magnetic field (see Sec. 2.2.2). Therefore, if the transport optics are set to point-to-point image particles with 20 MeV (imaging energy), the particles' angle will have a larger impact on the screen position the further away from this energy. This results in a smearing out of the charge density. In the extreme case, the angle can lead to a collision with the beam pipe and an absence at the diagnostic. This issue is shown in Figs. 5.4(a) and 5.5(a), where the bunch energy spectrum at different imaging energies is shown. While charge below 200 MeV is visible when imaging at 20 MeV, it is absent when imaging at 500 MeV: the low-energy particles are overfocused and lost in transport. Also, one can see that the beam traverses the interaction chamber with a downward angle, as the particles at the initial energy appear lower on the screen, i.e., with lower energy, if their energy is not imaged.

Measuring a well-imaged spectrum throughout its full energy range requires measuring it at varying imaging energies and then combining the well-imaged ranges. Fig. 5.4 illustrates this process with only three imaging energies. First, the spectra are multiplied with weighting functions to select well-imaged energy ranges, yielding weighted spectra. In the analysis, different functions such as the rectangular or Gaussian function were used, which yielded spectra with a negligible difference when using sufficient scan steps. For simplicity, the triangular function as in Fig. 5.4(b) is used, which reflects better than the rectangular function the gradual deterioration further from the imaged energy. The weighting function for each spectrum is normalized by the number of measured

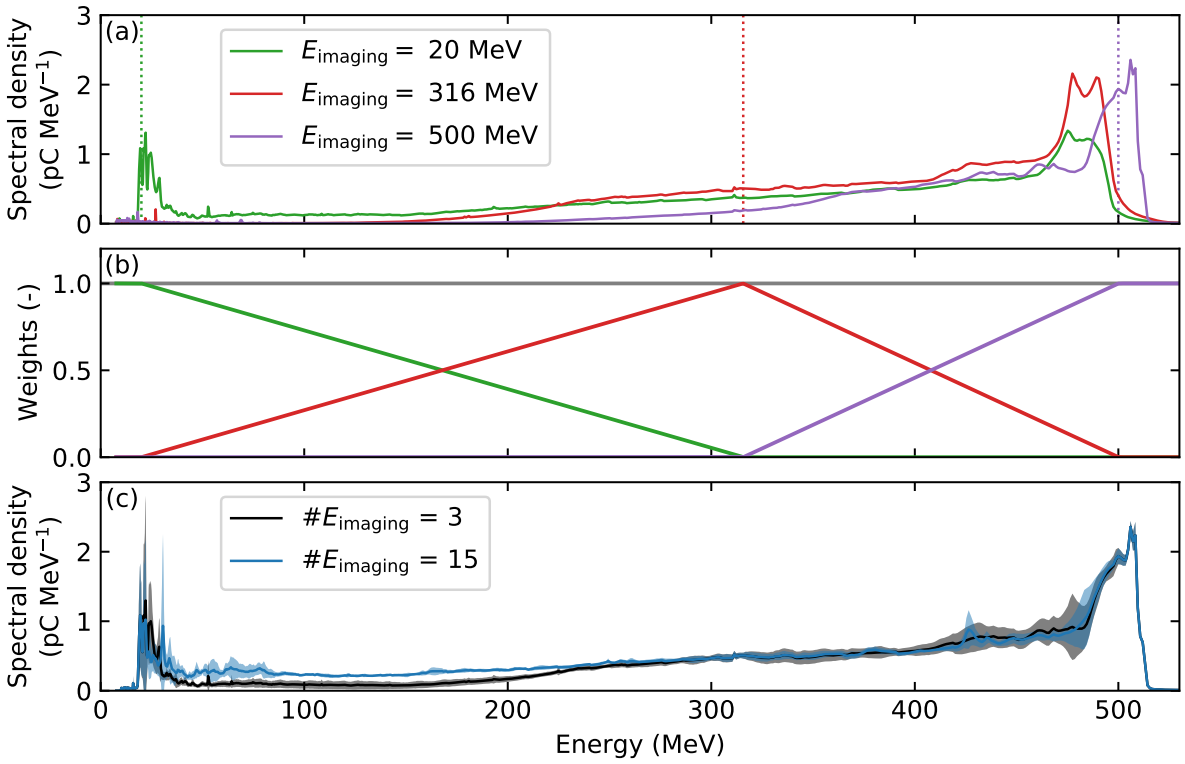

Figure 5.4: (a) Measured energy spectra for different imaging energies E_{imaging} marked with dotted vertical lines, at a plasma flattop density of 1.4×10^{16} cm^{-3}. (b) Weighting functions used to select well-imaged energy ranges for spectrum reconstruction. Across the full energy range, the sum of the weights is one (horizontal gray line). (c) In black, the reconstructed bunch energy spectrum, based on the measured spectra shown in (a) and weights in (b), with the band showing the rms error. For contrast, the reconstructed spectrum based on the full imaging energy scan as in Fig. 5.5 is shown in blue.

spectra per scan step. Second, the *average reconstructed spectrum* is computed with the sum of all the weighted spectra, as shown in Fig. 5.4(c). This process was repeated for a varying number of scan steps to ensure that the reconstructed spectra converged, which showed that 15 steps, as shown in Fig. 5.5(a), is sufficient. This yields the average reconstructed spectrum shown in Figs. 5.4(c) and 5.5(c).

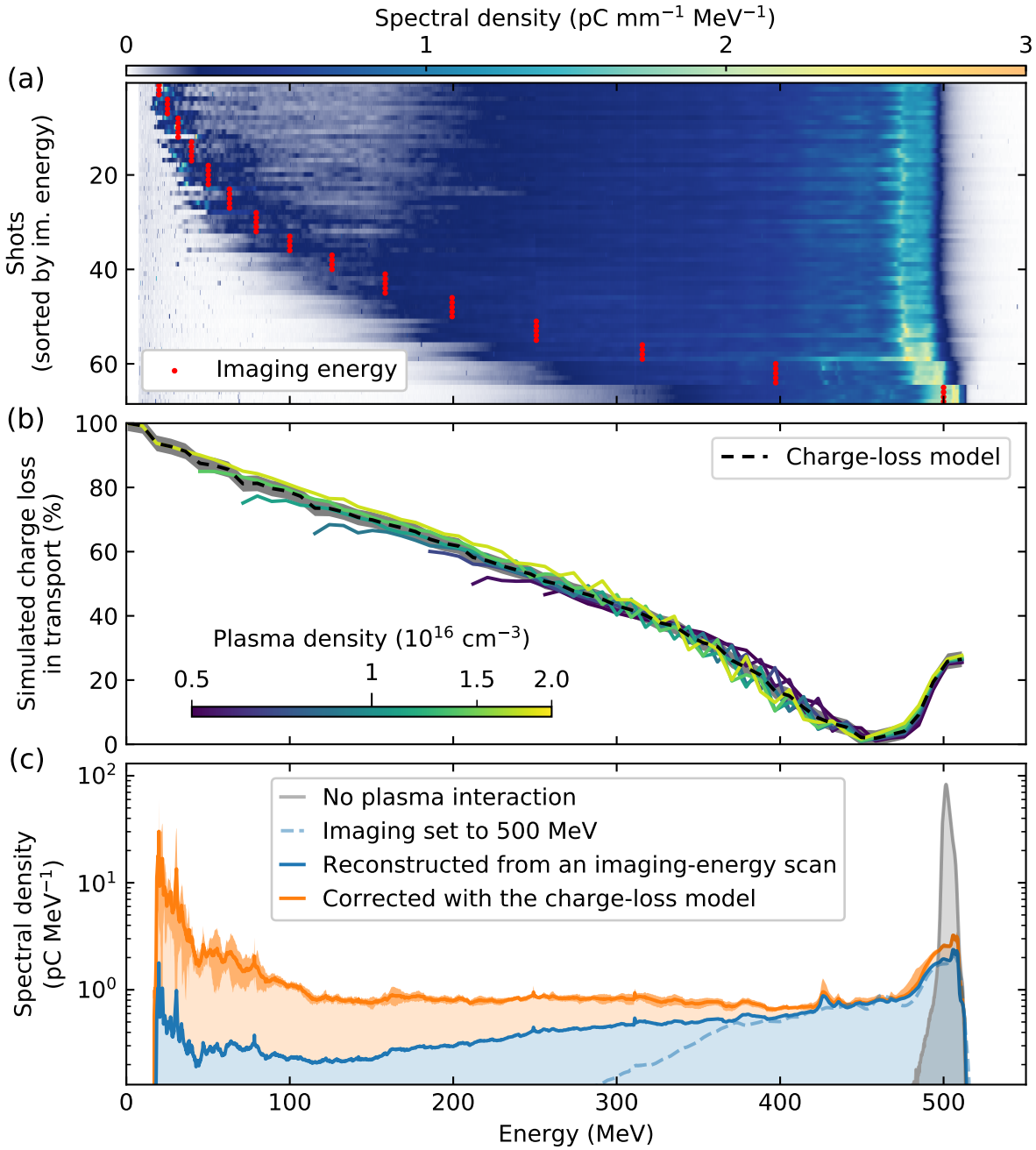

Figure 5.5: (a) Driver spectra measured at a plasma flattop density of 1.4×10^{16} cm^{-3}, for a scan of imaging energies (red points). (b) The fractional charge loss versus energy for PIC-simulated bunches, as caused by transport losses between the plasma-cell exit and the spectrometer screen. The average serves as a charge-loss model (dashed line), with an average rms error of 2.4% (gray band). (c) The reconstructed average spectrum (blue area) shows significant energy loss compared to no plasma interaction (gray area) but only accounts for 39% of the initial charge. The spectrum corrected by a charge-loss model (orange area), with a band indicating the rms error, accounts for all the charge. Figure adapted from Ref. [176].

5.2.2 Charge loss from high divergence

Integrating the average reconstructed spectrum yields a charge of ∼251 pC, which is well below the initial 636 pC. Not knowing where and at what energy the charge was lost introduces uncertainty on any estimate of the energy deposited into the plasma. To investigate this, simulations, such as in Fig. 5.1, were performed to recreate the experimental setup. Measured and estimated inputs were used for beam and plasma parameters. An overview of the simulation parameters can be found in Table 5.1, and the beam input parameters are summarized in Table 5.2. The bunch current shape follows that measured at the TDS and shown in Fig. 3.8. While the bunch charge at the TDS is lower than that measured at the cell entrance, assuming that the charge is lost uniformly during transport, the current is scaled up to match the incoming total charge. The simulations were not benchmarked quantitatively, but they agree qualitatively with the measurements in Fig. 5.3(b–d), and they do not show charge loss in the plasma. This is consistent with the measured plasma light, which is approximately longitudinally uniform until re-acceleration occurs, as shown in Fig. 5.3(e–f).

To investigate how the charge was lost on the way to the spectrometer, the bunch propagation was modeled with transfer matrices. To construct the matrices (see Sec. 2.2.5), we use the known beamline element positions, geometries, and magnetic field strengths. For each energy, a different transfer matrix is constructed. Using the simulated particles' position and angle at the plasma exit, the particles with a radial position beyond the beam-pipe aperture of 5 mm are identified. This reveals that the majority of the charge is already lost before the first quadrupole.

Fig. 5.5(b) shows the fraction of charge lost at each energy slice, for simulations with different flattop densities. Two distinct features can be seen: some charge is lost around the initial energy, and the majority is lost increasingly at lower energies. In the first case, the charge near the initial energy behaves as if no plasma were present, where a loss of ∼30% was already observed, which is attributed to the beam's divergence. In the

second case, the charge loss is predominant at lower energies, where the driver electrons are expected to have a larger divergence for the following three reasons.

- For a fixed transverse momentum p_x, a decrease in longitudinal momentum p_z will increase the divergence angle $x' \approx \arctan(x') = p_x/p_z$.

- Given a fixed focusing transverse force, low-energy beam slices are focused down to a smaller transverse beam size. As they exit the plasma, they will diverge faster from the smaller beam waist.

- Electrons at the head of the drive bunch, where the blowout regime has not yet fully formed, experience non-linear focusing fields. These fields increase the emittance, which, following Eq. 2.14, also increases the divergence.

We observe in Fig. 5.5(b) that the charge-loss fraction is similar for different densities, i.e., it is a function of energy and approximately independent of density. One can, therefore, construct a *charge-loss model* to predict what fraction of charge does not reach the spectrometer by averaging over the fractions of different densities, where average rms over the full energy range can be used as the error and is 2.4%. Dividing the reconstructed spectrum with this model yields the spectrum at the plasma exit, as shown in Fig. 5.5(c).

It should be noted that the charge-loss model does not account for the re-accelerated charge, which has a different and unknown angular distribution. Therefore, the model cannot be used to correct measurements where such charge is present. Nevertheless, as discussed in Sec. 5.1, measurements with re-acceleration are not suitable for preserving the quality of a trailing bunch. Therefore, placing a depletion-efficiency value in such measurements is irrelevant.

5.2.3 Estimating the energy deposition

Fig. 5.6 shows a scan of plasma density over the same range as in Fig. 5.3, for which the spectrum was measured with an imaging energy scan at each density step (as in Fig. 5.5). Fig. 5.6(a) shows that the charge of the measured average reconstructed spectrum decreases for higher densities. This is driven by the overall lower energy of the electrons and therefore larger divergence. Assuming that the charge is lost either at the initial energy or at the lowest energy observed in the spectrum allows placing bounds on the energy deposition, as shown with the blue bounds in Fig. 5.6(c). The true depletion efficiency lies within these bounds.

For a more certain estimate of the depletion efficiency, the charge-loss model can be used to account for all the incoming charge. However, both the charge-loss model as well as the reconstructed average spectrum have an uncertainty. Monte Carlo (MC) sampling can be used to assess how this affects the charge of the corrected spectra. The charge-loss model can be sampled with a normal distribution with $\sigma = 2.4\%$, which is the average rms error as shown in Fig. 5.5. Simultaneously, the average reconstructed spectra can be sampled with a normal distribution within its measured rms variation. As both uncertainties can be correlated with energy, the sampling is performed in equal-sized energy slices, where each slice is sampled independently. The energy-slice width yielding the largest error is used, as it is unknown which should be used. Then, for each separately sampled charge-loss model and spectrum, the spectrum is corrected. The charges of these corrected spectra are shown in Fig. 5.6(a).

Using the fact that, according to representative simulations, the charge was not lost in the plasma, those samples that reconstruct all the incoming charge can be selected; all other reconstructed spectra are not meaningful. The average depletion efficiency can be calculated with these selected samples, and the uncertainty estimated with the corresponding rms, as shown in Fig. 5.6(c). For the largest density without re-acceleration, i.e., 1.4×10^{16} cm^{-3}, the uncertainty drops from $\pm 29\%$ to $\pm 3\%$, and

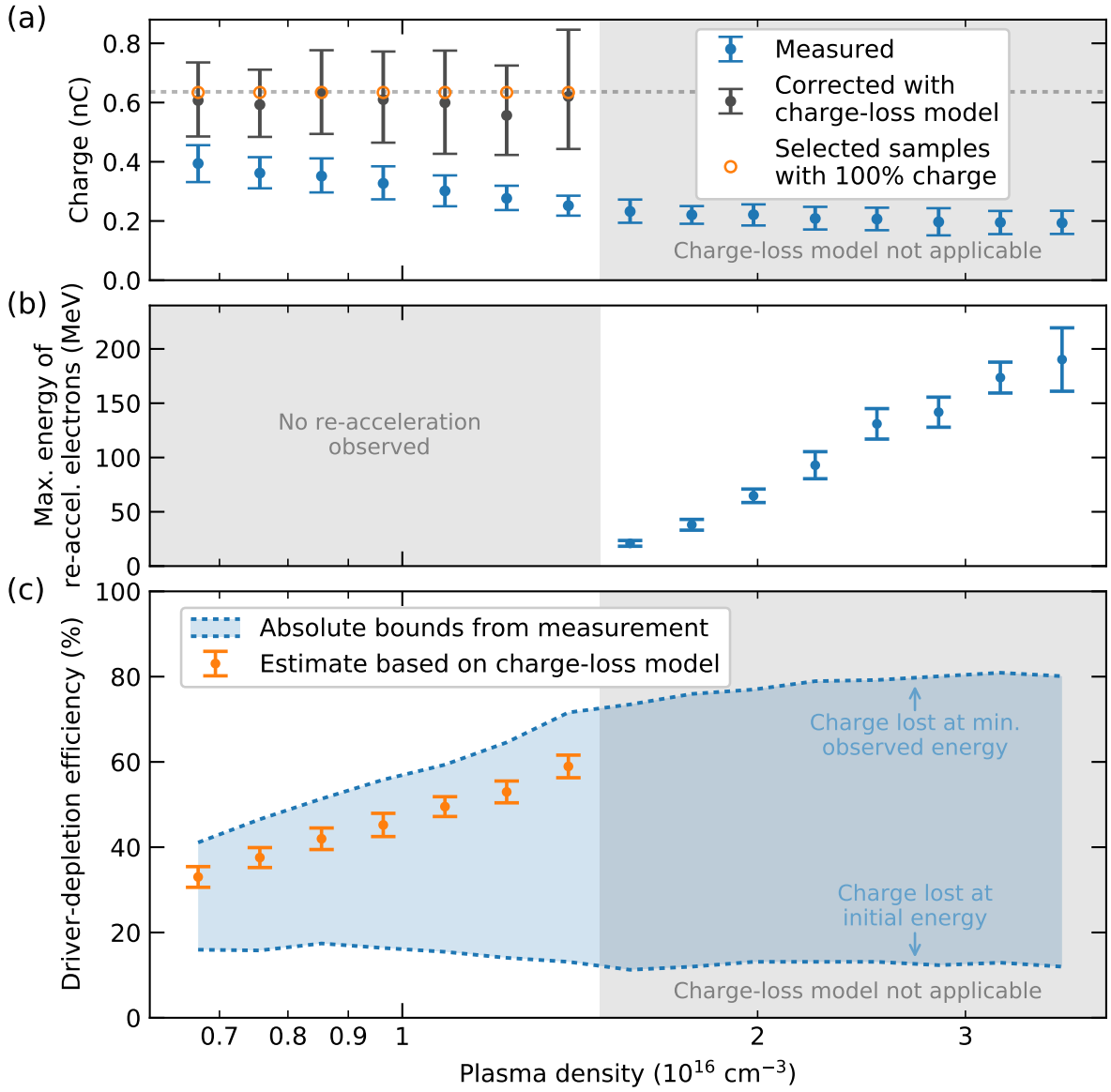

Figure 5.6: (a) For a scan of plasma density, the beam charge was measured upstream using a beam-position monitor (dashed line) and downstream using the spectrometer screen, with (blue) and without correction (gray). The error bars represent the median and central 68-percentile ranges, i.e., equivalent to σ, obtained by sampling the charge-loss model and spectra within their respective errors. As described in the text, the samples yielding the initial incoming charge at each density are selected to estimate the depletion efficiency (orange). (b) The maximum energy of the re-accelerated charge is shown (blue error bars; representing the mean and rms of the distribution), unless no such charge was observed (shaded area; left). (c) The driver-depletion efficiency is estimated by using the average efficiency of the samples reconstructing all the incoming charge [orange circles in (a)] and the uncertainty (orange error bar) by their rms. The absolute bounds based on the measurements, with unaccounted charge, are also shown (blue dashed lines). Figure from Ref. [176].

the maximum driver-depletion efficiency achieved is $(59 \pm 3)\%$.

It can be seen in Fig. 5.6(c) that the depletion efficiency follows a power-law increase with the plasma density. Doubling the plasma density results in 1.8 times the depletion, i.e., with an exponent of 0.85. Using Eqs. 2.26 and 2.27, the scaling should be with an exponent of 0.5. While the exponents are similar, their discrepancy can be explained as follows: the equations used in the estimate describe the peak fields. However, the energy-depletion efficiency is determined not by the maximum field but by the average decelerating field experienced by the driver. At the lower density, the bunch occupies a fraction of the decelerating region. While the bunch length stays constant, the wavelength of the wakefield decreases for higher plasma densities, moving the peak field toward the head of the bunch. Therefore, the peak field is nearer to the bulk of the bunch charge at higher density, increasing the overall energy-deposition rate. As a result, the depletion efficiency is expected to scale faster than the square root, as is shown in the measurement.

5.3 Discussion and Conclusions

Compared to previous results in the field ($\sim$6% [87, 137]), the driver-depletion efficiency of $(59 \pm 3)\%$ reported in this thesis is an order-of-magnitude improvement. It is, therefore, a key milestone in demonstrating high energy-transfer efficiency in a beam-driven plasma-wakefield accelerator. Also, this result was later supported by measurements performed at a different experiment, where a similar efficiency is reported [182]. However, simulations suggest that up to a $\sim$90% depletion efficiency should be possible. The limit for the experimental results presented here is the re-acceleration of driver electrons, as it hampers preserving the quality of a trailing bunch.

Re-acceleration starts when the first electrons reach non-relativistic energies, which are those located at the phase with the peak decelerating field. The onset of re-acceleration can be delayed by shaping the driver current, following the same idea as

beam-loading (see Sec. 2.4.2), such that all the driver electrons experience the same decelerating field. In this way, all the driver electrons will lose their energy at the same rate until they collectively* become non-relativistic. At this point, the drive-bunch energy is fully depleted, and the bunch has to be disposed of. Previous works calculated the ideal bunch current as trapezoidal, with increasing current towards the back and a short current spike at the very front [145, 146]. The plasma interaction of a drive bunch with such a current – but not optimized – is shown in Fig. 2.8, where the longitudinal field is approximately flat.

Over the decades, to cater to the needs of applications, many techniques have been developed to shape the current of a bunch in RF accelerators [71]. For example, a transverse-deflecting cavity can streak the beam vertically, then a collimating mask shapes the longitudinal charge distribution (which is in the vertical axis here), and finally, a second cavity streaks the beam back to the initial configuration [183]. Or multiple overlapping laser pulses at the gun photocathode can be used to tailor the bunch current [184], as was experimentally demonstrated with a plasma-interacted bunch pair in Ref. [185]. Another option is to map the transverse beam distribution onto the longitudinal axis in the so-called emittance exchange scheme, demonstrated experimentally with a plasma-interacted beam in Ref. [186]. In this experiment, the bunch was shaped by a combination of three actuators. First, an energy chirp can be imprinted on the bunch by off-crest acceleration in the RF modules. This chrip controls how strong the bunch is compressed in the downstream magnetic chicanes. Second, as the RF modules have a cosine-shaped accelerating field, so does the energy chirp. To linearize it, a third-harmonic cavity, also placed before the magnetic chicanes, was installed. This can be used to, at an approximately constant bunch length, change the charge distribution. Third, the bunch length can be sharply cut at the head and tail with the movable collimators [125–127]. However, to reach a decelerating field strong enough

*There will always be some fraction of the charge that is not energy depleted, as at the very front of the bunch the wakefields first have to develop.

to significantly deplete a 501 MeV drive bunch, high plasma densities are required. In turn, this shrinks the blowout bubble, which requires a short enough bunch and therefore strong bunch compression*. At the compression required, approximately a factor of 84, the longitudinal phase space is no longer linear, which renders the collimators significantly less effective. At the same time, the tuning range for shaping via the RF modules is reduced.

To increase the depletion with an experimental setup such as in this thesis, the simplest way is to make the plasma longer. This would allow using lower plasma densities and less-compressed bunches with a linear LPS. Currently, in beam-driven plasma wakefield acceleration, the plasma length is up to the order of hundreds of milimeters†. The longest plasma cell in the FLASHForward experiment at the time of writing is 195 mm long (see Fig. 3.3), which is the one used for the results in this Chapter. The cell design used here, which is widespread for creating and containing a plasma, consists of two sapphire slabs with drilled channels such that, when pressed together, a cylindrical channel is created. As the slab length, and therefore the plasma length, is limited by the channel-drilling machine, a new design is required. At FLASHForward, and with the involvement of the author‡, extensive work has gone into developing a longer cell of 500 mm. The design is based on a sapphire tube instead of two sapphire slabs, as depicted in Fig. 5.7.

Experimentally, operating a plasma accelerator with a longer plasma has proven more challenging, as processes such as instabilities or transverse kicks have more time to develop. However, with a similar deceleration between two cells of different lengths, the longer one would operate at a lower density, which would make the tolerances less restrictive as the wakefield structure becomes larger, at the price of lower accelerating gradients. Understanding the interplay between these two scalings will be the subject of

*The bunch at the gun is ∼7 ps long [108], and after compression 83 fs (see Table 5.2).

†The notable exception, with meters-long plasmas, is the AWAKE experiment [187]. Here, the plasma density is usually $\mathcal{O}(10^{14}\ \mathrm{cm}^{-3})$, lower than the densities used in this thesis, at 10^{15}–$10^{16}\ \mathrm{cm}^{-3}$.

‡Mainly organizational and assessing the physical requirements.

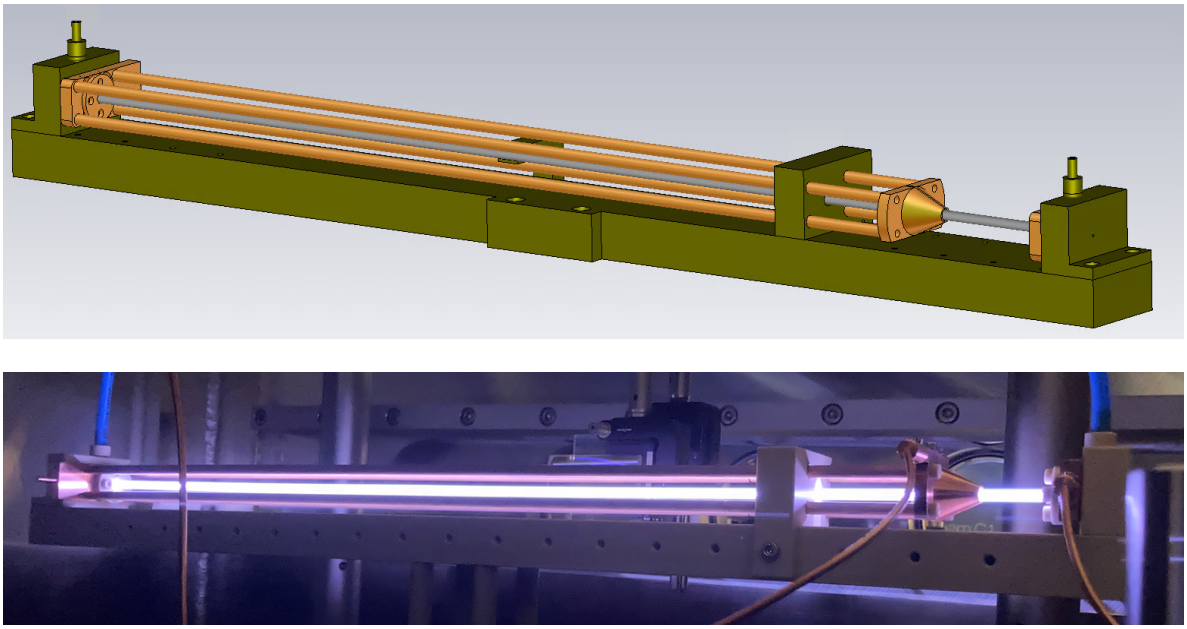

Figure 5.7: In the top: design of a 500-mm-long plasma cell. The cell holder is colored in olive green, the copper reddish brown, and the sapphire tube gray. Image courtesy of K. Ludwig. In the bottom: a picture of the prototype cell right after an electrical discharge in the beamline vacuum chamber. Image courtesy of G. Loisch.

future work.

Up to now, many experimental results have focused on achieving singled-out record efficiencies and key requirements such as high gradients. The next step is to recreate the energy-depletion efficiency demonstrated in this thesis with an accelerating trailing bunch. Achieving this at a sufficient repetition rate while preserving the trailing-bunch quality would demonstrate the suitability of plasma accelerators for high-beam-power applications.

Chapter 6

Summary, comparison to RF and outlook

This chapter provides an executive summary of this thesis, including an overview of literature publications related to energy-transfer efficiency (see Table 6.1). Then, the results presented in this thesis are compared with accelerators that are fully based on RF technology. This is followed by a discussion of different strategies to demonstrate higher overall efficiency in a plasma accelerator.

6.1 Executive summary

With the climate crisis advancing, greenhouse gas emissions must be reduced in all aspects of society. This includes research, where applications like colliders and *free-electron lasers* (FELs) can require large infrastructures and have a significant environmental impact. Furthermore, their size will increase based on developments in the last century and new facility designs. For linear accelerators, the elongation is driven by the requirement of higher particle energies, while their *radio-frequency* (RF) accelerating gradient is limited to 10–100 MV/m [26, 27].

With larger accelerating gradients of $\mathcal{O}$(1–100 GV/m), plasma accelerators promise

to shorten such research facilities. Experimental results have demonstrated acceleration with gradients of up to 265 GV/m [28, 29]. However, for high-beam-power accelerators, such as those used in colliders and FELs, plasma accelerators have further requirements to fulfill. These are mainly: operation at a high repetition rate, beam quality preservation, i.e., energy spread and emittance, and high energy-transfer efficiency. The latter two are treated in this thesis.

A plasma accelerator can be regarded as an energy transformer, where the energy of the driver is deposited into the plasma by forming wakefields and then extracted by the trailing bunch (see Fig. 2.9). The corresponding driver-to-plasma and plasma-to-trailing-bunch energy-transfer efficiencies are defined with Eqs. 2.31 and 2.32, respectively, where their product is the driver-to-trailing-bunch efficiency (Eq. 2.34). Ensuring high energy-transfer efficiency is important for several reasons. First, it determines the power consumption of the machine. For existing facilities, e.g., *Large Hadron Collider* (LHC) [3] and *European X-Ray Free-Electron Laser Facility* (European XFEL) [19] (see Fig. 1.1), the power consumption is already prohibitive economically and will become more so in future higher-energy facilities. Moreover, the power consumption also determines the environmental footprint. As can be seen in Fig. 1.4, for such machines, this constitutes a large fraction of the overall footprint. If the efficiency is insufficient, the gains from a reduced footprint from construction by using plasma accelerators are erased by excess power consumption, rendering this a futile effort. Second, low efficiency can lead to a limited performance of the machine. For example, any energy not extracted by the trailing bunch remains in the plasma. For colliders and FELs, usually with repetition rates of $\mathcal{O}$(10–100 kHz) and a beam power of $\mathcal{O}$(1 MW), this can lead to a build-up of heat that must be removed. Eq. 4.2 shows that a restrictive cooling capacity requires a compromise between accelerating gradient and charge, plasma-to-trailing-bunch efficiency, and repetition rate. Operating at high plasma-to-trailing-bunch efficiency can lessen the restriction on the other parameters, which together determine an accelerator's performance.

Publication	$\eta_{d\to p}$ (%)	$\eta_{p\to w}$ (%)	$\eta_{d\to w}$ (%)	E_D (MeV)	ΔE_D (MeV)	Q_D (pC)	E_W (MeV)	ΔE_W (MeV)	Q_W (pC)	E_z (GV/m)	L (cm)
M. Litos[a] *et al.*, 2014 [144]	2.1	30	0.63	20 350	427	926	20 350	1600	47	4.4	36[j]
S. Corde[a] *et al.*, 2015 [87]	5.9[d]	34	2	20 350	1200	2100	20 350	4200	207	3.2	130[j]
C. A. Lindstrøm[b] *et al.*, 2021 [104]	1.8[f]	42	0.8	1027[f]	19[f]	490	1030	45	100	1.3	3.2
L. Boulton[b] *et al.*, 2022 [137]	6.6	38[e]	2.5	1052	69	368	1052	194	47	1.0	19.5
F. Peña[c] *et al.*, 2023 [176]	59	–	–	501	295[h]	636	–	–	–	2.6[k]	19.5
C. A. Lindstrøm[b] *et al.*, 2024 [160]	1.7	22	0.4	1050	18	400	1050	40	40	0.8	5
K. V. Lotov,[b] 2005 [145]	90	90	81	510	459	$180Q_0$[i]	510	826	$90Q_0$[i]	$2E_0$[l]	$900k_{pe}^{-1}$
M. Tzoufras[b] *et al.*, 2008 [100]	–	90[g]	–	–	–	–	–	–	–	$1.75E_0$[l,g]	–
Q. Su[b] *et al.*, 2023 [146]	∼93	∼90	∼84	28 500	∼26 500	5000	28 500	27 800	4300	∼28	100

[a] A single bunch is used, where the head drives the wakefields and the charge in the tail is accelerated.
[b] A driver and trailing bunch pair is used.
[c] Only a drive bunch is used.
[d] Using the stated 2.54 J that were deposited into the plasma, and assuming that this was deposited by the non-accelerated charge.
[e] With a peak local extraction efficiency of 58%.
[f] With Ref. [173].
[g] Analytical approximation.
[h] For the corrected spectrum.
[i] $Q_0 = en_{pe}c^3\omega^{-3}$.
[j] Full width at half maximum.
[k] Average decelerating gradient.
[l] E_0 defined in Eq. 2.26.

Table 6.1: Literature selection with parameters relevant to energy-transfer efficiency in PWFA. The columns are (1) the publication; (2–4) the driver-to-plasma (Eq. 2.31), plasma-to-trailing-bunch (Eq. 2.32), and driver-to-trailing-bunch (Eq. 2.34) efficiency, respectively; (5, 6) driving-charge initial and deposited energy; (7) driving charge; (8, 9) accelerating-charge initial and gained energy; (10) accelerated charge; (11) average accelerating gradient; (12) plasma-column length. The efficiencies (2–4) are averaged throughout the plasma length. All values were either stated in the individual publications or calculated by the author from other parameters stated there. The symbol "∼" shows the values the author estimated or read from figures. The double horizontal line separates the experimental (upper) from the theoretical/simulation (lower) results.

Even if high energy-transfer efficiency in a plasma accelerator is demonstrated, colliders and FELs also have requirements in beam quality. Respectively, the energy spread is usually at or below 0.1% [67] and between 0.1–1% [66, 188], and the transverse emittance is as low as 0.01 mm mrad [27, 31] and at or below 1 mm mrad per 0.1% energy bandwidth. For this reason, this thesis focuses on energy efficiency while preserving the quality of a trailing bunch.

Chapter 4 shows experimental results with an energy-extraction efficiency of 22%, which is similar to previous experimental results (see Table 6.1). The novelty of this result is that the emittance of 2.8 mm mrad is preserved, together with 40 pC of charge and 0.1% of relative energy spread (see Fig. 4.12). This is a significant result, as processes that can degrade these parameters, such as mismatch, non-linear focusing, or nonuniform accelerating fields, are all mitigated. As beam-quality preservation at higher energy-extraction efficiency can be limited by the development of transverse instabilities (see Sec. 4.3), a novel diagnostic method is discussed in this chapter, which could measure the onset of such instabilities and help determine experimentally the interplay between plasma-to-trailing-bunch energy-transfer efficiency and transverse instability.

Chapter 5 investigates maximizing the driver-to-plasma energy-transfer efficiency. Simulations show that once the first driver electrons reach non-relativistic energies, they slip back in phase and are re-accelerated (see Fig. 5.1). This process limits the driver depletion efficiency, as the wakefield structure changes significantly in three ways. First, less charge drives the wakefields. Second, additional charge beam-loads the accelerating field. Third, the space charge of non-relativistic driver electrons, or the transition to the linear regime, de-linearizes the transverse focusing fields, which can lead to emittance growth. This process is measured in this thesis with Fig. 5.3, and the onset is shown to follow the theory presented in Ref. [99] (see Eq. 5.3). Estimating the driver-to-plasma efficiency at this limit requires accurate imaging of the beam with 98% energy spread and correcting for charge loss at different energy slices (see Fig. 5.5).

These two complications are a direct consequence of quadrupole (chromatic) optics and a larger divergence of decelerated particles, respectively. Therefore, they are not specific to this thesis's experimental setup and are important for future measurements and other experimental facilities. The direct measurement shows a depletion efficiency between 13% and 72%, where the charge loss due to the larger divergence at lower energies dominates the uncertainty. After correcting for this charge loss with a model based on simulations recreating the experiment, the depletion efficiency is $(59 \pm 3)\%$ (see Fig. 5.6). This is an order-of-magnitude improvement to previous results in the literature (see Table 6.1) and, therefore, a key milestone for demonstrating high-energy-efficient plasma accelerators. Furthermore, this thesis reports the first detailed measurement, with two independent diagnostics, of electron re-acceleration (see Fig. 5.3), which is a limitation for energy-depletion efficiency and consequently for the overall energy transfer efficiency of plasma accelerators.

6.2 Plasma-accelerator efficiency compared to RF accelerators

With the results on energy efficiency summarized in the previous section, now plasma and RF accelerators are compared. For this, the parameters of the proposed collider CLIC [27] are used. Its acceleration scheme is similar to plasma accelerators, as it also produces a drive bunch to then accelerate the *main bunch*, which is then used for collisions. Here, instead of using plasma, the energy is transferred through a *Power Extraction and Transfer Structure* (PETS). In these special RF cavities, the low-energy and high-current drive bunch is decelerated producing the RF power that is then transferred to power the cavities accelerating the low-current main bunch to high energies. This design allows for higher energy-transfer efficiency than powering the RF cavities directly with Klystrons, as is usual*. The wall-plug-to-main-beam energy-transfer efficiency in this two-beam-acceleration scheme is 11% [27, Fig. 2.36].

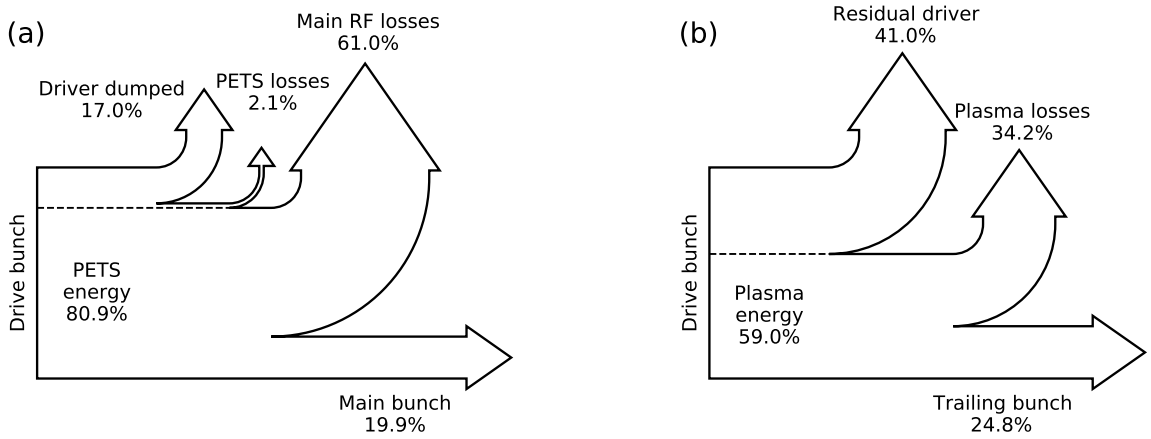

Figure 6.1: (a) Energy transfer diagram from the drive bunch to the main bunch at CLIC, adapted from Ref. [27, Fig. 2.36] (CC-BY 3.0). (b) The corresponding diagram for a beam-driven plasma accelerator, where the energy-deposition and extraction efficiencies from Chapter 5 and Ref. [104] are used, respectively.

Including beam transport, beam-delivery system, and cooling, this efficiency becomes 4.8% [27, Fig. 2.37]. This is similar to other constructed and proposed facilities, e.g., FLASH with 2.6% [189], XFEL with 10% [190], and ILC with up to 10% [31].

Fig. 6.1(a) shows a Sankey diagram illustrating the energy flow from the drive beam to the main beam at CLIC. To compare with plasma accelerators, Fig. 6.1(b) shows the energy transfer from the driver to the trailing bunch, where the record efficiencies to date are used, i.e., 59% [176] for deposition and 42% [104] for extraction. In this comparison, plasma accelerators seem promising, as their driver-to-trailing-bunch efficiency of 25% is similar to the driver-to-main-beam efficiency of CLIC at 19.9%. However, such a working point has not been demonstrated, as the deposition and extraction efficiencies were demonstrated only individually. Furthermore, as discussed in Sections 1.4 and 4, the quality of the trailing bunch must be preserved during acceleration. In the record extraction result, no emittance preservation was shown; in the record deposition result, no trailing bunch was present. Therefore, for a fair comparison, the result presented

*The high accelerating gradients require the use of high frequency, and therefore frequency-multiplying the Klystron output, which lowers their efficiency. This, together with the quantity of required Klystrons, makes it a disadvantageous design [27, Sec. 2.1.2].

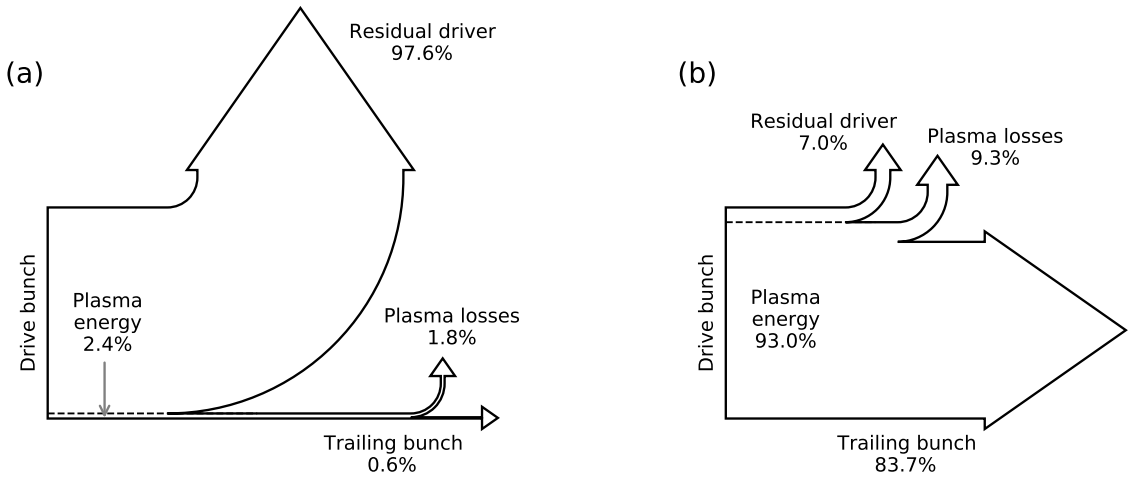

Figure 6.2: (a) Energy transfer diagram using the experimental result of Sec. 4.2. (b) Corresponding diagram using the simulation results of Ref. [146].

in Sec. 4.2 must be used, as here the quality of the trailing bunch is preserved. A Sankey diagram of this working point is shown in Fig. 6.2(a). While the extraction efficiency here was significant, the overall efficiency is low due to the energy dumped with the drive bunch, which showcases that high energy deposition is essential for the overall accelerator performance. It should be noted that in this result, the goal was the preservation of the trailing-bunch quality, and the energy-transfer efficiency was not optimized. Simultaneous optimization of both should be attempted in future experiments.

According to simulations higher energy efficiency is possible if the bunch currents are shaped accordingly. Following Ref. [146], the driver-to-plasma and plasma-to-trailing-bunch energy-transfer efficiency could be 93% and 90%, respectively, which is shown in Fig. 6.2(b). While the high gradients of plasma accelerators are usually stated as their main advantage, this figure shows that their overall energy-transfer efficiency could also be an asset, as the efficiency in this case is 83.7%. However, these simulations recreate the interaction under ideal conditions, i.e. initiating the bunch without tilts, which will not lead to instabilities. Experimentally, however, the bunches will not be perfectly aligned. Therefore, while high overall efficiency should be attempted experimentally, tolerance studies should take place to investigate what is possible under realistic conditions.

It should be noted that, in this chapter, the comparison is made without considering the efficiency at which the drive bunch is produced and accelerated. The efficiency of RF accelerators depends on their mode of operation, i.e., super or normal conducting cavities, their repetition rate, their accelerating gradient, etc. These conditions will be determined by the application, facility size, and restrictions in repetition rate set by, e.g., the long-term plasma evolution or cell cooling. Klystrons, which are the power source of RF accelerators, have become very efficient over the decades, reaching up to 80% [191]. This can yield an efficiency of generally $\mathcal{O}(10\%)$, with CLIC envisaged at a 55% drive-bunch production and acceleration efficiency. If this efficiency were used to estimate the efficiency of a plasma accelerator, for example as in Fig. 6.1(b), it would be 14%, which is similar to existing and proposed accelerator facilities. A more detailed estimate for a collider using plasma accelerator technology is given in the HALHF proposal [30]. While also based on assumptions*, it foresees an 8% collider-facility efficiency, including RF accelerators, beam transport, and beam-delivery systems.

6.3 Strategies for high overall energy-transfer efficiency

This section discusses different strategies to demonstrate experimentally high driver-to-trailing-bunch energy-transfer efficiency in plasma accelerators. This discussion is summarized with Fig. 6.3, where Eq. 2.34 was rewritten by replacing the trailing-bunch energy gain ΔE_w with E_z and L, which are the accelerating gradient and length, respectively. In each of the following paragraphs, the effect of individual parameters on efficiency is explained, while assuming all others are kept constant.

Accelerating gradient E_z

Adjusting the plasma density to increase the accelerating gradient will increase

*For the plasma-accelerator stages, a 72% energy-deposition and 53% energy-extraction efficiency.

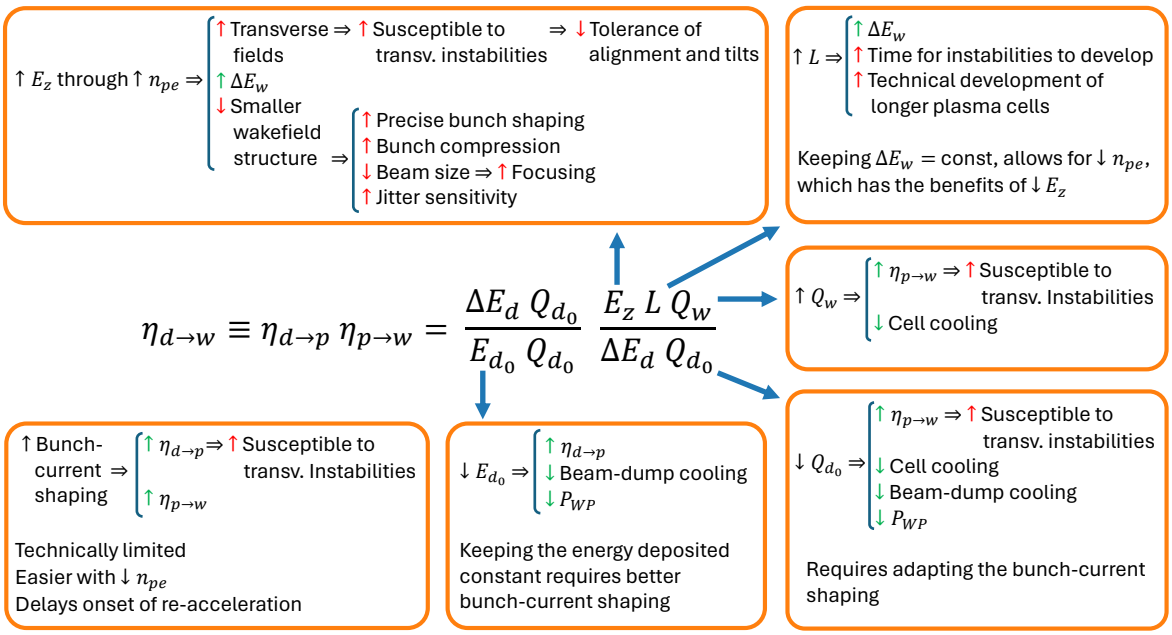

Figure 6.3: Overview of different strategies to increase the overall efficiency of a plasma accelerator. The effect of adjusting a single parameter while all others are kept constant is summarized in a yellow rounded rectangle. An arrow pointing upwards stands for "more", "increasing" or "stronger", with downwards meaning the opposite, and the symbol "⇒" stands for "yields" or "leads to". The colors red and green are used to identify the effects and scalings that are generally detrimental or beneficial, respectively.

the trailing bunch's energy gain and, consequently, the energy-extraction efficiency. However, higher plasma densities shrink the volume of the blowout bubble, leading to additional constraints. First, for the bunches to be placed in the correct wakefield phase, they must become shorter by stronger compression. Second, as the transverse fields become stronger, the tolerances for beam misalignment or tilts, which can lead to instabilities, are smaller. Third, the transverse bunch size must be reduced to keep the beam matched and within the radial extent of the wakefield. This can be done by using beams with smaller emittance or, being the simpler strategy, by strengthening the focusing system. The latter option, however, worsens any chromatic effects of the focusing system. For such reasons, although accelerating gradients of $\mathcal{O}(100\ \mathrm{GV/m})$ have been demonstrated [28, 29], experimental results usually show gradients of $\mathcal{O}(1\ \mathrm{GV/m})$, as can be seen in Table 6.1. This is a compromise between demonstrating high gradients

compared to RF accelerators and simplifying experimental operation. Another reason not to pursue higher gradients is that the size of a collider might not be dominated by the accelerator anymore. For example, the HALHF [30] collider proposes using gradients of 6.4 GV/m in the plasma stages. While the collider has a length of 3.3 km (see Fig. 1.3), the whole plasma-accelerator section would comprise 410 m, including the beamline connecting 16 plasma stages, and the beam-delivery system is 2.25 km long. In this case, using higher gradients would not significantly shorten the facility and not decrease the environmental footprint and construction cost.

Bunch current shaping

The energy deposition and extraction efficiencies can be improved by adequately shaping the bunch currents, as shown in Fig. 2.8. At FLASHForward, this was done by correlating the longitudinal position with energy and using collimating masks (see Sec. 3.1). The precision at which the bunches can be reliably shaped is limited in highly compressed setups as in Chapter 5. Generally, this can be eased by operating at a lower plasma density, as it allows using less compressed bunches. However, this method involves collimators removing the charge at the bunch's longitudinal center to create the driver and trailing bunch pair, effectively dumping a significant fraction of the initial charge. This becomes problematic if it is used in high-beam-power machines, as it lowers the machine's energy efficiency and produces additional radiation. Therefore, a method not involving collimating masks should be envisaged, such as using multiple laser pulses at the photocathode (see discussion in Sec. 5.3).

It should be noted that bunch-shaping capability is a general requirement for a plasma-accelerator facility. The onset of electron re-acceleration must be sufficiently delayed, and the accelerating fields must be appropriately beam-loaded; both require adjusting current shapes.

Trailing-bunch charge Q_w

A trailing bunch with a higher charge extracts more energy from the plasma. Therefore, the cell requires less cooling power and the energy-extraction efficiency is increased. The latter also leads to an increased susceptibility to instabilities (see Sec. 4.3), while chapter 4.2 demonstrates that an efficiency of 22% is possible.

Drive-bunch charge Q_{d_0}

Using less charge in the driving bunch leads to, with Eq. 2.32, a higher energy-extraction efficiency and, again, possibly to the development of instabilities. Again, the required cell cooling power is lower, and in this case, also for the beam dumps. As less beam power is used to drive the plasma accelerator stages, less wall-plug power would be required. While the latter outcome will be important for future facilities, it is the author's opinion that it has a lower priority at the current demonstrative research stage.

Drive-bunch energy E_{d_0}

Reducing the energy of the incoming driver while keeping the total energy deposited constant increases the driver-depletion efficiency. While the requirements for plasma-cell cooling are unchanged, they are lower for the beam dumps, as less energy remains in the driver after the interaction. Again, while being a lower priority for now, this reduces the overall power consumed.

Plasma length L

Another way to increase the efficiency is to allow the energy transfer to occur over a longer time, i.e., making the plasma longer. This leads to higher trailing-bunch energy and allows for instabilities to develop further. If the energy gain is kept constant, elongating the plasma column would allow using a lower plasma density, which eases operation*. For this reason, while experiments often employed plasma columns of

*This has the opposite consequences as for the case where the accelerating gradient is increased, described further above.

$\leq$ 200 mm, they are generally converging towards longer plasmas.

A compromise

Building upon the experimental results at the FLASHForward experiment, a strategy is proposed in the following to demonstrate a $\mathcal{O}(10\%)$ driver-to-trailing-bunch efficiency. As is often the case for complex systems, a combination of optimizing different parameters might be required. Parting from the results presented in Ref. [137] (see Table 6.1), the simplest path is to elongate the plasma by, e.g., a factor of ∼2.5, from 195 mm to 500 mm. This would allow for the trailing bunch to gain ∼490 MeV, yielding a driver-to-trailing-bunch efficiency of ∼6%. Increasing the accelerating field by, e.g., a factor of two, would allow the trailing bunch to reach ∼980 MeV, and the driver-to-trailing-bunch efficiency would be 12%. Following Eqs. 2.24 and 2.26, such a change in fields can be achieved by increasing the plasma density by a factor of four. However, care has to be taken since, as discussed previously, the tolerances for bunch alignment will become smaller. Also, the bunch separation and their current shapes must be changed accordingly. Successfully implementing the steps suggested here could demonstrate a plasma accelerator operating close to the driver-to-main-bunch energy-transfer efficiency of 20% at CLIC (see Fig. 6.1), which would be a key milestone toward implementation of plasma accelerators in high-beam-power applications. However, as discussed in the introduction, the quality of the bunch must also be preserved. This will become increasingly difficult the longer the plasma becomes and the higher the plasma density used.

References

The Digital Object Identifier (DOI) is a unique identifier for objects on the internet, including publications, which can be accessed by appending the DOI to the URL `https://www.doi.org/`.

[1] Intergovernmental Panel on Climate Change (IPCC) (2021). (Cited on p. 1)
"Climate Change 2021 – The Physical Science Basis: Working Group I Contribution to the Sixth Assessment Report of the Intergovernmental Panel on Climate Change"
DOI: 10.1017/9781009157896.

[2] SustainableHECAP+ Initiative. (2023). (Cited on pp. 1, 8)
"Environmental sustainability in basic research: A perspective from HECAP+"
URL: https://sustainable-hecap-plus.github.io/.

[3] Lyndon Evans and Philip Bryant. *Journal of Instrumentation* **3**, 08, S08001 (Aug. 2008). (Cited on pp. 1, 102)
"LHC Machine"
DOI: 10.1088/1748-0221/3/08/S08001.

[4] CMS Collaboration. *Physics Letters B* **716**, 1, pp. 1–29 (2012). (Cited on pp. 1, 2)
"Observation of a new particle in the search for the Standard Model Higgs boson with the ATLAS detector at the LHC"
DOI: 10.1016/j.physletb.2012.08.020.

[5] ATLAS Collaboration. *Physics Letters B* **716**, 1, pp. 30–61 (2012). (Cited on pp. 1, 2)
"Observation of a new boson at a mass of 125 GeV with the CMS experiment at the LHC"
DOI: 10.1016/j.physletb.2012.08.021.

[6] G. Arnison et al. *Physics Letters B* **126**, 5, pp. 398–410 (1983). (Cited on p. 2)
"Experimental observation of lepton pairs of invariant mass around 95 GeV/c2 at the CERN SPS collider"
DOI: 10.1016/0370-2693(83)90188-0.

[7] S. Abachi et al. *Phys. Rev. Lett.* **74**, pp. 2632–2637 (14 Apr. 1995). (Cited on p. 2)
"Observation of the Top Quark"
DOI: 10.1103/PhysRevLett.74.2632.

[8] F. Abe et al. *Phys. Rev. Lett.* **74**, pp. 2626–2631 (14 Apr. 1995). (Cited on p. 2)
"Observation of Top Quark Production in $\overline{p}p$ Collisions with the Collider Detector at Fermilab"
DOI: 10.1103/PhysRevLett.74.2626.

[9] U.S. Department of Energy. 2010. (Cited on p. 2)
"Accelerators for America's Future"
URL: https://science.osti.gov/-/media/hep/pdf/files/pdfs/Accel_for_Americas_Future_final_report.pdf.

[10] Barney L. Doyle et al. *Reviews of Accelerator Science and Technology* **10**, 01, pp. 93–116 (2019). (Cited on p. 2)
"The Future of Industrial Accelerators and Applications"
DOI: 10.1142/S1793626819300068.

[11] Komitee für Beschleunigerphysik. 2016. (Cited on p. 2)
"Beschleuniger für Teilchen, Wissen und Gesellschaft"
URL: https://www.beschleunigerphysik.de/de/service/broschuere/.

[12] E A Seddon et al. *Reports on Progress in Physics* **80**, 11, p. 115901 (Oct. 2017). (Cited on pp. 2, 5)
"Short-wavelength free-electron laser sources and science: a review*"
DOI: 10.1088/1361-6633/aa7cca.

[13] Richard Neutze et al. *Current Opinion in Structural Biology* **33**, pp. 115–125 (2015). (Cited on p. 2)
"Membrane protein structural biology using X-ray free electron lasers"
DOI: 10.1016/j.sbi.2015.08.006.

[14] Oliver Gessner and Markus Gühr. *Accounts of Chemical Research* **49**, 1, pp. 138–145 (Jan. 2016). (Cited on p. 2)
"Monitoring Ultrafast Chemical Dynamics by Time-Domain X-ray Photo- and Auger-Electron Spectroscopy"
DOI: 10.1021/acs.accounts.5b00361.

[15] D. Milathianaki et al. *Science* **342**, 6155, pp. 220–223 (2013). (Cited on p. 2)
"Femtosecond Visualization of Lattice Dynamics in Shock-Compressed Matter"
DOI: 10.1126/science.1239566.

[16] T. D. Swinburne et al. *Phys. Rev. B* **93**, p. 144119 (14 Apr. 2016). (Cited on p. 2)
"Picosecond dynamics of a shock-driven displacive phase transformation in Zr"
DOI: 10.1103/PhysRevB.93.144119.

[17] Maximilien Brice, CERN. (2008) (CC-BY-SA-4.0). (Cited on p. 4)
URL: https://cds.cern.ch/record/1295244.

[18] European XFEL / Luftaufnahmen: FHH, Landesbetrieb Geoinf. und Vermessung (2017/18/21). (Cited on p. 4)
URL: https://media.xfel.eu/XFELmediabank/catalog/Presse_XFEL_2023/r/6261.

[19] M. Altarelli et al. DESY XFEL Project Group, DESY-06-097. 2007. (Cited on pp. 5, 20, 102)
"The European X-ray free-electron laser, technical design report"
DOI: 10.3204/DESY_06-097.

[20] John M. J. Madey. *Journal of Applied Physics* **42**, 5, pp. 1906–1913 (Apr. 1971). (Cited on p. 5)
"Stimulated Emission of Bremsstrahlung in a Periodic Magnetic Field"
DOI: 10.1063/1.1660466.

[21] Tomas Ekeberg et al. *Light: Science & Applications* **13**, 1, p. 15 (Jan. 2024). (Cited on p. 5)
"Observation of a single protein by ultrafast X-ray diffraction"
DOI: 10.1038/s41377-023-01352-7.

[22] Thomas P Wangler. John Wiley & Sons. (2008) (Cited on p. 5)
"RF Linear accelerators"
DOI: 10.1002/9783527623426.

[23] W. D. Kilpatrick. *Review of Scientific Instruments* **28**, 10, pp. 824–826 (Oct. 1957). (Cited on p. 5)
"Criterion for Vacuum Sparking Designed to Include Both rf and dc"
DOI: 10.1063/1.1715731.

[24] TJ Boyd Jr. *Los Alamos Group AT-1 report AT-1* **82**, p. 28 (1982). (Cited on p. 5)
"Kilpatrick's criterion"

[25] Alexander Wu Chao et al. World Scientific. (2013) (Cited on p. 5)
"Handbook of Accelerator Physics and Engineering"
DOI: 10.1142/8543.

[26] A. Grudiev et al. *Phys. Rev. ST Accel. Beams* **12**, p. 102001 (10 Oct. 2009). (Cited on pp. 5, 101)
"New local field quantity describing the high gradient limit of accelerating structures"
DOI: 10.1103/PhysRevSTAB.12.102001.

[27] M Aicheler et al. CERN Yellow Reports: Monographs (2012). (Cited on pp. 5, 6, 10, 24, 52, 101, 104–106)
"A Multi-TeV Linear Collider Based on CLIC Technology: CLIC Conceptual Design Report"
DOI: 10.5170/CERN-2012-007.

[28] S Bohlen et al. *Physical Review Letters* **129**, 24, p. 244801 (2022). (Cited on pp. 6, 102, 109)
"In situ measurement of electron energy evolution in a laser-plasma accelerator"
DOI: 10.1103/PhysRevLett.129.244801.

[29] Sébastien Corde et al. *Nature communications* **7**, 1, p. 11898 (2016). (Cited on pp. 6, 102, 109)
"High-field plasma acceleration in a high-ionization-potential gas"
DOI: 10.1038/ncomms11898.

[30] B Foster et al. *New Journal of Physics* **25**, 9, p. 093037 (Sept. 2023). (Cited on pp. 6, 7, 10, 50, 51, 108, 110)
"A hybrid, asymmetric, linear Higgs factory based on plasma-wakefield and radio-frequency acceleration"
DOI: 10.1088/1367-2630/acf395.

[31] Ties Behnke et al. *arXiv* [physics.acc-ph] (2013). (Cited on pp. 6, 20, 52, 104, 106)
"The International Linear Collider Technical Design Report - Volume 1: Executive Summary"
DOI: 10.48550/arXiv.1306.6327.

[32] M Aicheler et al. *CERN Yellow Reports: Monographs* **4** (2018). (Cited on pp. 6, 10, 20, 51)
"The Compact Linear Collider (CLIC) – Project Implementation Plan"
DOI: 10.23731/CYRM-2018-004.

[33] R D'Arcy et al. *Nature* **603**, 7899, pp. 58–62 (2022). (Cited on p. 7)
"Recovery time of a plasma-wakefield accelerator"
DOI: 10.1038/s41586-021-04348-8.

[34] Jérôme Faure et al. *Plasma Physics and Controlled Fusion* **61**, 1, p. 014012 (2018). (Cited on p. 7)
"A review of recent progress on laser-plasma acceleration at kHz repetition rate"
DOI: 10.1088/1361-6587/aae047.

[35] James Chappell. PhD thesis. University College London, London, 2021. (Cited on p. 7)
"Experimental study of long timescale plasma wakefield evolution"
URL: https://discovery.ucl.ac.uk/id/eprint/10134739.

[36] G. Bernardi et al. *arXiv* [hep-ex] (2022). (Cited on pp. 8, 10)
"The Future Circular Collider: a Summary for the US 2021 Snowmass Process"
DOI: 10.48550/arXiv.2203.06520.

[37] A Abada et al. *The European Physical Journal Special Topics* **228**, pp. 261–623 (2019). (Cited on pp. 8, 10)
"FCC-ee: the lepton collider: future circular collider conceptual design report volume 2"
DOI: 10.1140/epjst/e2019-900045-4.

[38] Huajie Cheng et al. *arXiv* [hep-ph] (2022). (Cited on pp. 8, 10)
"The Physics potential of the CEPC. Prepared for the US Snowmass Community Planning Exercise (Snowmass 2021)"
DOI: 10.48550/arXiv.2205.08553.

[39] CEPC Accelerator Study Group. *arXiv* [physics.acc-ph] (2022). (Cited on pp. 8, 10)
"Snowmass2021 White Paper AF3-CEPC"
DOI: 10.48550/arXiv.2203.09451.

[40] Martin Breidenbach et al. *PRX Energy* **2**, p. 047001 (4 Oct. 2023). (Cited on pp. 8–10)
"Sustainability Strategy for the Cool Copper Collider"
DOI: 10.1103/PRXEnergy.2.047001.

[41] IEA, World Energy Outlook 2022, (2022), Paris, Licence: CC BY 4.0 (report); CC BY NC SA 4.0 (Annex A). (Cited on p. 8)
URL: https://www.iea.org/reports/world-energy-outlook-2022.

[42] The Green ILC Project. (Cited on p. 8)
URL: https://green-ilc.in2p3.fr/home/.

[43] OECD, in: *OECD Environment Statistics (database)*. (accessed on 19 February 2024). (Cited on p. 9)
"Air and climate: Air Transport CO2 Emissions"
DOI: 10.1787/13d4f295-en, URL: https://stats.oecd.org/Index.aspx?DataSetCode=AIRTRANS_CO2.

[44] Bundesamt für Statistik, Schweizerische Eidgenossenschaft: Ständige Wohnbevölkerung des Canton Genève (2022), accessed on Mar. 14, 2024. (Cited on p. 9)
URL: https://www.pxweb.bfs.admin.ch/pxweb/de/px-x-0102010000_101/-/px-x-0102010000_101.px/.

[45] CERN, Energy management, (accessed on Dec. 3, 2022). (Cited on p. 9)
URL: https://hse.cern/content/energy-management.

[46] Emilio A. Nanni et al. *arXiv* [physics.acc-ph] (2022). (Cited on p. 10)
"C^3 Demonstration Research and Development Plan"
DOI: 10.48550/arXiv.2203.09076.

[47] Alexander Aryshev et al. *arXiv* [physics.acc-ph] (2023). (Cited on p. 10)
"The International Linear Collider: Report to Snowmass 2021"
DOI: 10.48550/arXiv.2203.07622.

[48] S. Evans and B. Castle. *ARUP Group*. (2023). (Cited on p. 10)
"CLIC and ILC Life Cycle Assessment Final Report"
URL: https://edms.cern.ch/document/2917948/1.

[49] D. A. Edwards and M. J. Syphers. Wiley Series in Beam Physics and Accelerator Technology. Wiley. (2008) (Cited on p. 11)
"An Introduction to the Physics of High Energy Accelerators"
DOI: 10.1002/9783527617272, ISBN: 9783527617289.

[50] Helmut Wiedemann. *Nuclear Instruments and Methods in Physics Research Section A: Accelerators, Spectrometers, Detectors and Associated Equipment* **266**, 1, pp. 24–31 (1988). (Cited on p. 11)
"An ultra-low emittance mode for PEP using damping wigglers"
DOI: 10.1016/0168-9002(88)90354-3.

[51] M. Reiser. Wiley series in beam physics and accelerator technology. John Wiley & Sons, New York. (2008) (Cited on pp. 12, 21, 22)
"Theory and Design of Charged Particle Beams"
DOI: 10.1002/9783527622047, ISBN: 978-3-527-40741-5.

[52] Peter Schmüser et al. Springer Tracts in Modern Physics. Springer Cham. (2014) (Cited on p. 12)
"Free-Electron Lasers in the Ultraviolet and X-Ray Regime"
DOI: 10.1007/978-3-319-04081-3, ISBN: 978-3-319-04081-3.

[53] Francis F. Chen. Springer New York, NY. (1984) (Cited on p. 16)
"Introduction to Plasma Physics and Controlled Fusion"
DOI: 10.1007/978-3-319-22309-4, ISBN: 978-3-319-22309-4.

[54] Paul Gibbon. *arXiv* [physics.acc-ph] (2020). (Cited on p. 16)
"Introduction to Plasma Physics"
DOI: 10.48550/arXiv.2007.04783.

[55] Ferenc Krausz and Misha Ivanov. *Rev. Mod. Phys.* **81**, pp. 163–234 (1 Feb. 2009). (Cited on p. 16)
"Attosecond physics"
DOI: 10.1103/RevModPhys.81.163.

[56] R Shalloo. PhD thesis. University of Oxford, Oxford, 2018. (Cited on p. 16)
"Hydrodynamic optical-field-ionized plasma waveguides for laser plasma accelerators"
URL: https://ora.ox.ac.uk/objects/uuid:aa7a03d0-2d64-423f-be42-40e01479d312.

[57] D.N. Fittinghoff. PhD thesis. Lawrence Livermore National Laboratory, 1993. (Cited on p. 16)
"Optical field ionization of atoms and ions using ultrashort laser pulses"
URL: https://inis.iaea.org/search/search.aspx?orig_q=RN:25038227.

[58] L. V. Keldysh. *J. Exp. Theor. Phys.* **20**, 5, pp. 1307–1314 (1965). (Cited on p. 16)
"Ionization in the Field of a Strong Electromagnetic Wave"
DOI: 10.1142/9789811279461_0008.

[59] Friedrich Paschen. *Annalen der Physik* **273**, 5, pp. 69–96 (1889). (Cited on p. 16)
"Ueber die zum Funkenübergang in Luft, Wasserstoff und Kohlensäure bei verschiedenen Drucken erforderliche Potentialdifferenz"
DOI: 10.1002/andp.18892730505.

[60] D. J. Spence and S. M. Hooker. *Phys. Rev. E* **63**, p. 015401 (1 Dec. 2000). (Cited on pp. 16, 43)
"Investigation of a hydrogen plasma waveguide"
DOI: 10.1103/PhysRevE.63.015401.

[61] D. J. Spence et al. *J. Opt. Soc. Am. B* **20**, 1, pp. 138–151 (Jan. 2003). (Cited on p. 16)
"Gas-filled capillary discharge waveguides"
DOI: 10.1364/JOSAB.20.000138.

[62] Felipe Peña. Master thesis. Technical University of Munich, Munich (2019). (Cited on p. 18)
"Predicting the Trajectories of Relativistic Particle Beams for External Injection in Plasma Wakefield Acceleration"
DOI: 21.11116/0000-0005-D6C3-D.

[63] Klaus Wille. Oxford University Press. (2000) (Cited on pp. 19, 23)
"The physics of particle accelerators: an introduction"
ISBN: 978-0198505495.

[64] H. Zyngier. *Laboratoire de l'Accélérateur Linéaire, LAL-77/35.* (Nov. 1977). (Cited on p. 20)
"Strategy for Correcting for Chromaticity"
URL: https://lib-extopc.kek.jp/preprints/PDF/1978/7801/7801139.pdf.

[65] Brian William Montague. (1979). (Cited on p. 20)
"Linear Optics For Improved Chromaticity Correction"
URL: https://cds.cern.ch/record/443342.

[66] Zhirong Huang and Kwang-Je Kim. *Phys. Rev. ST Accel. Beams* **10**, p. 034801 (3 Mar. 2007). (Cited on pp. 20, 104)
"Review of x-ray free-electron laser theory"
DOI: 10.1103/PhysRevSTAB.10.034801.

[67] Pantaleo Raimondi and Andrei Seryi. *Phys. Rev. Lett.* **86**, pp. 3779–3782 (17 Apr. 2001). (Cited on pp. 20, 104)
"Novel Final Focus Design for Future Linear Colliders"
DOI: 10.1103/PhysRevLett.86.3779.

[68] Klaus Floettmann. *Phys. Rev. ST Accel. Beams* **6**, p. 034202 (Mar. 2003). (Cited on p. 21)
"Some basic features of the beam emittance"
DOI: 10.1103/PhysRevSTAB.6.034202.

[69] Klaus Floettmann. *Phys. Rev. ST Accel. Beams* **6**, p. 079901 (July 2003). (Cited on p. 21)
"Erratum: Some basic features of the beam emittance [Phys. Rev. ST Accel. Beams 6, 034202 (2003)]"
DOI: 10.1103/PhysRevSTAB.6.079901.

[70] Helmut Wiedemann. Springer. (2015) (Cited on pp. 22, 25, 31)
"Particle Accelerator Physics"
DOI: 10.1007/978-3-319-18317-6, ISBN: 978-3-319-18317-6.

[71] G. Ha et al. *Rev. Mod. Phys.* **94**, p. 025006 (2022). (Cited on pp. 22, 97)
"Bunch shaping in electron linear accelerators"
DOI: 10.1103/RevModPhys.94.025006.

[72] T.O. Raubenheimer et al., in: *Proceedings Particle Accelerator Conference*. (1995), 3291–3293 vol.5. (Cited on p. 24)
"Beam distribution function after filamentation"
DOI: 10.1109/PAC.1995.505858.

[73] M. Sands. (1991). (Cited on pp. 24, 52)
"A beta mismatch parameter"
URL: https://lib-extopc.kek.jp/preprints/PDF/1991/9105/9105527.pdf.

[74] T. Mehrling et al. *Phys. Rev. ST Accel. Beams* **15**, p. 111303 (11 Nov. 2012). (Cited on p. 24)
"Transverse emittance growth in staged laser-wakefield acceleration"
DOI: 10.1103/PhysRevSTAB.15.111303.

[75] P. Michel et al. *Phys. Rev. E* **74**, p. 026501 (2 Aug. 2006). (Cited on p. 24)
"Radiative damping and electron beam dynamics in plasma-based accelerators"
DOI: 10.1103/PhysRevE.74.026501.

[76] Karl L. Brown. *Report-75, Rev. 2, SLAC*. (Aug. 1971). (Cited on p. 25)
"A First and Second Order Matrix Theory for the Design of Beam Transport Systems and Charged Particle Spectrometers"
DOI: 10.2172/4742148, URL: https://www.osti.gov/biblio/4742148.

[77] P. Baxevanis and G. Stupakov. *Phys. Rev. Accel. Beams* **21**, p. 071301 (7 July 2018). (Cited on p. 27)
"Novel fast simulation technique for axisymmetric plasma wakefield acceleration configurations in the blowout regime"
DOI: 10.1103/PhysRevAccelBeams.21.071301.

[78] A Ferran Pousa et al. *Journal of Physics: Conference Series* **1350**, 1, p. 012056 (Nov. 2019). (Cited on pp. 27, 121)
"Wake-T: a fast particle tracking code for plasma-based accelerators"
DOI: 10.1088/1742-6596/1350/1/012056.

[79] Jean-Luc Vay and Rémi Lehe. *Reviews of Accelerator Science and Technology* **09**, pp. 165–186 (2016). (Cited on p. 27)
"Simulations for Plasma and Laser Acceleration"
DOI: 10.1142/S1793626816300085.

[80] S. Diederichs et al. *Computer Physics Communications* **278**, p. 108421 (2022). (Cited on pp. 28, 69, 79)
"HiPACE++: A portable, 3D quasi-static particle-in-cell code"
DOI: 10.1016/j.cpc.2022.108421.

[81] P. Sprangle et al. *Phys. Rev. A* **41**, pp. 4463–4469 (8 Apr. 1990). (Cited on p. 28)
"Nonlinear interaction of intense laser pulses in plasmas"
DOI: 10.1103/PhysRevA.41.4463.

[82] P. Sprangle et al. *Phys. Rev. Lett.* **64**, pp. 2011–2014 (17 Apr. 1990). (Cited on p. 28)
"Nonlinear theory of intense laser-plasma interactions"
DOI: 10.1103/PhysRevLett.64.2011.

[83] A. Ting et al. *Physics of Fluids B: Plasma Physics* **2**, 6, pp. 1390–1394 (1990). (Cited on p. 28)
"Nonlinear wake-field generation and relativistic focusing of intense laser pulses in plasmas"
DOI: 10.1063/1.859561.

[84] E. Esarey et al. *AIP Conference Proceedings* **569**, 1, pp. 473–486 (2001). (Cited on p. 28)
"Betatron radiation from electron beams in plasma focusing channels"
DOI: 10.1063/1.1384377.

[85] E. Esarey et al. *Rev. Mod. Phys.* **81**, pp. 1229–1285 (3 Aug. 2009). (Cited on p. 29)
"Physics of laser-driven plasma-based electron accelerators"
DOI: 10.1103/RevModPhys.81.1229.

[86] T. Tajima and J. M. Dawson. *Phys. Rev. Lett.* **43**, pp. 267–270 (4 July 1979). (Cited on p. 29)
"Laser Electron Accelerator"
DOI: 10.1103/PhysRevLett.43.267.

[87] Sébastien Corde et al. *Nature* **524**, 7566, pp. 442–445 (2015). (Cited on pp. 29, 77, 96, 103)
"Multi-gigaelectronvolt acceleration of positrons in a self-loaded plasma wakefield"
DOI: 10.1038/nature14890.

[88] Erik Adli et al. *Nature* **561**, 7723, pp. 363–367 (2018). (Cited on p. 29)
"Acceleration of electrons in the plasma wakefield of a proton bunch"
DOI: 10.1038/s41586-018-0485-4.

[89] P. Gibbon. Imperial College press. (2005) (Cited on p. 29)
"Short Pulse Laser Interactions with Matter: An Introduction"
DOI: 10.1142/p116.

[90] Allen Caldwell et al. *Nat Phys* **5**, 5, pp. 363–367 (May 2009). (Cited on p. 29)
"Proton-driven plasma-wakefield acceleration"
DOI: 10.1038/nphys1248.

[91] W. Lu et al. *Physics of Plasmas* **12**, 6, p. 063101 (2005). (Cited on p. 30)
"Limits of linear plasma wakefield theory for electron or positron beams"
DOI: 10.1063/1.1905587.

[92] Roswell Lee and Martin Lampe. *Phys. Rev. Lett.* **31**, pp. 1390–1393 (23 Dec. 1973). (Cited on p. 30)
"Electromagnetic Instabilities, Filamentation, and Focusing of Relativistic Electron Beams"
DOI: 10.1103/PhysRevLett.31.1390.

[93] A. Bret et al. *Physics of Plasmas* **17**, 12, p. 120501 (Dec. 2010). (Cited on p. 30)
"Multidimensional electron beam-plasma instabilities in the relativistic regime"
DOI: 10.1063/1.3514586.

[94] L. Verra et al. *arXiv* [physics.plasm-ph] (2023). (Cited on p. 30)
"Filamentation of a Relativistic Proton Bunch in Plasma"
DOI: 10.48550/arXiv.2312.13883.

[95] Rhon Keinigs and Michael E. Jones. *The Physics of Fluids* **30**, 1, pp. 252–263 (Jan. 1987). (Cited on pp. 30, 31)
"Two-dimensional dynamics of the plasma wakefield accelerator"
DOI: 10.1063/1.866183.

[96] Ian Blumenfeld. PhD thesis. Stanford University, California, 2009. (Cited on pp. 30, 36)
"Scaling of the longitudinal electric fields and transformer ratio in a non-linear Plasma Wakefield Accelerator"
URL: https://ui.adsabs.harvard.edu/abs/2009PhDT.......154B.

[97] C.A. Lindstrøm and M. Thévenet. *Journal of Instrumentation* **17**, 05, P05016 (May 2022). (Cited on pp. 31, 52, 53, 79)
"Emittance preservation in advanced accelerators"
DOI: 10.1088/1748-0221/17/05/p05016.

[98] The Figure was created by the author with the simulation code Wake-T [78]. (Cited on pp. 31, 33, 35)

[99] W. Lu et al. *Physics of Plasmas* **13**, 5 (2006). (Cited on pp. 32–37, 87, 88, 104)
"A nonlinear theory for multidimensional relativistic plasma wave wakefields"
DOI: 10.1063/1.2203364.

[100] M. Tzoufras et al. *Phys. Rev. Lett.* **101**, p. 145002 (14 Sept. 2008). (Cited on pp. 32, 34, 37, 51, 71, 103)
"Beam Loading in the Nonlinear Regime of Plasma-Based Acceleration"
DOI: 10.1103/PhysRevLett.101.145002.

[101] A. A. Golovanov and I. Yu. Kostyukov. *Physics of Plasmas* **25**, 10, p. 103107 (Oct. 2018). (Cited on p. 32)
"Bubble regime of plasma wakefield in 2D and 3D geometries"
DOI: 10.1063/1.5047274.

[102] James Albritton and Paul Koch. *The Physics of Fluids* **18**, 9, pp. 1136–1139 (Sept. 1975). (Cited on p. 34)
"Cold plasma wavebreaking: Production of energetic electrons"
DOI: 10.1063/1.861300.

[103] W. K. H. Panofsky and W. A. Wenzel. *Review of Scientific Instruments* **27**, 11, pp. 967–967 (1956). (Cited on p. 34)
"Some Considerations Concerning the Transverse Deflection of Charged Particles in Radio-Frequency Fields"
DOI: 10.1063/1.1715427.

[104] C. A. Lindstrøm et al. *Phys. Rev. Lett.* **126**, p. 014801 (1 Jan. 2021). (Cited on pp. 34, 41, 51, 52, 70, 78, 103, 106)
"Energy-Spread Preservation and High Efficiency in a Plasma-Wakefield Accelerator"
DOI: 10.1103/PhysRevLett.126.014801.

[105] Ian Blumenfeld et al. *Nature* **445**, 7129, pp. 741–744 (2007). (Cited on pp. 36, 77, 88)
"Energy doubling of 42 GeV electrons in a metre-scale plasma wakefield accelerator"
DOI: 10.1038/nature05538.

[106] David L Bruhwiler et al. *Physics of Plasmas* **10**, 5, pp. 2022–2030 (2003). (Cited on p. 36)
"Particle-in-cell simulations of tunneling ionization effects in plasma-based accelerators"
DOI: 10.1063/1.1566027.

[107] The simulation was run with Wake-T, and VisualPIC [192] was used to produce the image, with help from A. de la Ossa and A. Ferran Pousa. (Cited on p. 37)

[108] Siegfried Schreiber and Bart Faatz. *High Power Laser Science and Engineering* **3**, e20 (2015). (Cited on pp. 39–41, 98)
"The free-electron laser FLASH"
DOI: 10.1017/hpl.2015.16.

[109] AM Kondratenko and EL Saldin. *Part. Accel.* **10**, pp. 207–216 (1980). (Cited on p. 39)
"Generating of coherent radiation by a relativistic electron beam in an ondulator"
URL: https://cds.cern.ch/record/1107977/files/p207.pdf.

[110] R. Bonifacio et al. *Optics Communications* **50**, 6, pp. 373–378 (1984). (Cited on p. 39)
"Collective instabilities and high-gain regime in a free electron laser"
DOI: 10.1016/0030-4018(84)90105-6.

[111] Jörg Rossbach et al. *Physics Reports* **808**, pp. 1–74 (2019). (Cited on p. 39)
"10 years of pioneering X-ray science at the Free-Electron Laser FLASH at DESY"
DOI: 10.1016/j.physrep.2019.02.002.

[112] J. Andruszkow et al. *Phys. Rev. Lett.* **85**, pp. 3825–3829 (18 Oct. 2000). (Cited on p. 39)
"First Observation of Self-Amplified Spontaneous Emission in a Free-Electron Laser at 109 nm Wavelength"
DOI: 10.1103/PhysRevLett.85.3825.

[113] V. Ayvazyan et al. *The European Physical Journal D - Atomic, Molecular, Optical and Plasma Physics* **37**, 2, pp. 297–303 (Feb. 2006). (Cited on p. 39)
"First operation of a free-electron laser generating GW power radiation at 32 nm wavelength"
DOI: 10.1140/epjd/e2005-00308-1.

[114] Jörg Rossbach, in: *Proceedings of the 10th European Particle Accelerator Conference - EPAC2006*. JACoW Publishing. (2006), pp. 34–38. (Cited on p. 39)
"Results from FLASH"
URL: https://accelconf.web.cern.ch/e06/PAPERS/MOZBPA01.PDF.

[115] W. Ackermann et al. *Nature Photonics* **1**, 6, pp. 336–342 (June 2007). (Cited on p. 39)
"Operation of a free-electron laser from the extreme ultraviolet to the water window"
DOI: 10.1038/nphoton.2007.76.

[116] Siegfried Schreiber et al., in: *Proceedings of the 11th European Particle Accelerator Conference - EPAC2008*. JACoW Publishing. (2008), pp. 133–135. (Cited on p. 39)
"Operation of FLASH at 6.5 nm wavelength"
URL: https://accelconf.web.cern.ch/e08/papers/mopc030.pdf.

[117] Jörg Rossbach, in: *Proc. of the 30th Intl. FEL Conf.* (2008). (Cited on p. 39)
"First lasing below 7 nm wavelength at FLASH/DESY, Hamburg"
URL: https://accelconf.web.cern.ch/fel2008/papers/moaau01.pdf.

[118] Richard D'Arcy et al. *Philosophical Transactions of the Royal Society A* **377**, 2151, p. 20180392 (2019). (Cited on p. 39)
"FLASHForward: plasma wakefield accelerator science for high-average-power applications"
DOI: 10.1098/rsta.2018.0392.

[119] Pau González Caminal. PhD thesis. Universität Hamburg, Hamburg, 2022, p. 262. (Cited on pp. 40, 46)
"Time-Resolved Phase-Space Characterisation of Plasma-Wakefield-Accelerated Electrons at FLASHForward"
URL: https://doi.org/10.3204/PUBDB-2022-03578.

[120] S. Schreiber et al., in: *Proc. of International Free Electron Laser Conference (FEL'17), Santa Fe, NM, USA, August 20-25, 2017*. JACoW. (Feb. 2018), pp. 415–418. (Cited on p. 40)
"Update on the Lifetime of Cs2Te Photocathodes Operated at FLASH"
DOI: 10.18429/JACoW-FEL2017-WEP003, ISBN: 978-3-95450-179-3.

[121] T. Limberg et al. *Nuclear Instruments and Methods in Physics Research Section A: Accelerators, Spectrometers, Detectors and Associated Equipment* **375**, 1, pp. 322–324 (1996). (Cited on p. 41)
"The bunch compression system at the TESLA test facility FEL"
DOI: 10.1016/0168-9002(95)01470-5.

[122] Frank Stulle. PhD thesis. Hamburg: Universität Hamburg, 2004, p. 111. (Cited on p. 41)
"A bunch compressor for small emittances and high peak currents at the VUV Free-Electron Laser"
URL: https://doi.org/10.3204/DESY-THESIS-2004-041.

[123] H. Edwards et al., in: *25th International Linear Accelerator Conference*. KEK. (Sept. 2010). (Cited on p. 41)
"3.9 GHz Cavity Module for Linear Bunch Compression at FLASH"
URL: https://bib-pubdb1.desy.de/record/91880.

[124] E. Vogel et al. *Proceedings of the 1st International Particle Accelerator Conference - IPAC2010* **100523**, 4281–4283 (May 2010). (Cited on p. 41)
"Test and Commissioning of the Third Harmonic RF System for FLASH"
DOI: https://www.osti.gov/biblio/1847753.

[125] S Schröder et al. *Journal of Physics: Conference Series* **1596**, 1, p. 012002 (July 2020). (Cited on pp. 42, 97)
"Tunable and precise two-bunch generation at FLASHForward"
DOI: 10.1088/1742-6596/1596/1/012002.

[126] P. Muggli et al. *Phys. Rev. Lett.* **101**, p. 054801 (2008). (Cited on pp. 42, 97)
"Generation of Trains of Electron Microbunches with Adjustable Subpicosecond Spacing"
DOI: 10.1103/PhysRevLett.101.054801.

[127] P. Muggli et al. *Phys. Rev. ST Accel. Beams* **13**, p. 052803 (2010). (Cited on pp. 42, 97)
"Simple method for generating adjustable trains of picosecond electron bunches"
DOI: 10.1103/PhysRevSTAB.13.052803.

[128] S Schröder et al. *Journal of Physics: Conference Series* **1596**, 1, p. 012002 (July 2020). (Cited on p. 42)
"Tunable and precise two-bunch generation at FLASHForward"
DOI: 10.1088/1742-6596/1596/1/012002.

[129] Sarah Schröder. PhD thesis. Universität Hamburg, Hamburg, 2021. (Cited on p. 42)
"External injection of electron beams into plasma-wakefield accelerators"
URL: https://doi.org/10.3204/PUBDB-2021-05396.

[130] A. Knetsch et al. *Phys. Rev. Accel. Beams* **24**, p. 101302 (10 Oct. 2021). (Cited on pp. 42, 85)
"Stable witness-beam formation in a beam-driven plasma cathode"
DOI: 10.1103/PhysRevAccelBeams.24.101302.

[131] Carl A. Lindstrøm et al., in: *Proceedings of The European Physical Society Conference on High Energy Physics — PoS(EPS-HEP2021)*. (2022), p. 880. (Cited on p. 42)
"Progress of the FLASHForward X-2 high-beam-quality, high-efficiency plasma-accelerator experiment"
DOI: 10.22323/1.398.0880.

[132] J. M. Garland et al. *Review of Scientific Instruments* **92**, 1 (Jan. 2021). (Cited on p. 43)
"Combining laser interferometry and plasma spectroscopy for spatially resolved high-sensitivity plasma density measurements in discharge capillaries"
DOI: 10.1063/5.0021117.

[133] Hans Griem. Elsevier. (2012) (Cited on p. 43)
"Spectral line broadening by plasmas"
ISBN: 9780323150941.

[134] Marco A Gigosos and Valentín Cardeñoso. *Journal of Physics B: Atomic, Molecular and Optical Physics* **29**, 20, p. 4795 (Oct. 1996). (Cited on p. 43)
"New plasma diagnosis tables of hydrogen Stark broadening including ion dynamics"
DOI: 10.1088/0953-4075/29/20/029.

[135] Marco A. Gigosos et al. *Spectrochimica Acta Part B: Atomic Spectroscopy* **58**, 8, pp. 1489–1504 (2003). (Cited on p. 43)
"Computer simulated Balmer-alpha, -beta and -gamma Stark line profiles for non-equilibrium plasmas diagnostics"
DOI: 10.1016/S0584-8547(03)00097-1.

[136] E. Oz et al. *AIP Conference Proceedings* **737**, 1, pp. 708–714 (Dec. 2004). (Cited on pp. 43, 72)
"Optical Diagnostics for Plasma Wakefield Accelerators"
DOI: 10.1063/1.1842612.

[137] L. Boulton et al. *arXiv* [physics.acc-ph] (2022). (Cited on pp. 43, 51, 53, 72–74, 96, 103, 112)
"Longitudinally resolved measurement of energy-transfer efficiency in a plasma-wakefield accelerator"
DOI: 10.48550/arXiv.2209.06690.

[138] Lewis Boulton. PhD thesis. University of Strathclyde, Glasgow, 2023. (Cited on pp. 43, 51, 53)
"Optimisation of energy and brightness transformer stages in a Plasma Wakefield Accelerator"

[139] P. González Caminal et al. *Phys. Rev. Accel. Beams* **27**, p. 032801 (3 Mar. 2024). (Cited on p. 46)
"Beam-based commissioning of a novel X-band transverse deflection structure with variable polarization"
DOI: 10.1103/PhysRevAccelBeams.27.032801.

[140] P. Craievich et al. *Phys. Rev. Accel. Beams* **23**, p. 112001 (11 Nov. 2020). (Cited on p. 46)
"Novel X-band transverse deflection structure with variable polarization"
DOI: 10.1103/PhysRevAccelBeams.23.112001.

[141] Barbara Marchetti et al. *Scientific reports* **11**, 1, p. 3560 (2021). (Cited on p. 46)
"Experimental demonstration of novel beam characterization using a polarizable X-band transverse deflection structure"
DOI: 10.1038/s41598-021-82687-2.

[142] Gregor Loisch and Harry Jones, private communication (2023). (Cited on p. 50)

[143] Gregor Loisch et al., in: *6th European Advanced Accelerator Concepts workshop*. (2023). (Cited on p. 50)
"Beam-driven plasma wakefield acceleration at Megahertz repetition rates"
URL: https://agenda.infn.it/event/35577/contributions/208732/.

[144] M. Litos et al. *Nature* **515**, 7525, pp. 92–95 (2014). (Cited on pp. 51, 70, 77, 103)
"High-efficiency acceleration of an electron beam in a plasma wakefield accelerator"
DOI: 10.1038/nature13882.

[145] K. V. Lotov. *Physics of Plasmas* **12**, 5, p. 053105 (May 2005). (Cited on pp. 52, 71, 97, 103)
"Efficient operating mode of the plasma wakefield accelerator"
DOI: 10.1063/1.1889444.

[146] Q. Su et al. *Physics of Plasmas* **30**, 5, p. 053108 (May 2023). (Cited on pp. 52, 71, 97, 103, 107)
"Optimization of transformer ratio and beam loading in a plasma wakefield accelerator with a structure-exploiting algorithm"
DOI: 10.1063/5.0142940.

[147] Kaoru Yokoya and Pisin Chen, in: *Frontiers of Particle Beams: Intensity Limitations*. Ed. by M. Dienes et al. Springer Berlin Heidelberg. (1992), pp. 415–445. (Cited on p. 52)
"Beam-beam phenomena in linear colliders"
DOI: 10.1007/3-540-55250-2_37, ISBN: 978-3-540-46797-7.

[148] R. D'Arcy et al. *Phys. Rev. Lett.* **122**, p. 034801 (3 Jan. 2019). (Cited on pp. 52, 71)
"Tunable Plasma-Based Energy Dechirper"
DOI: 10.1103/PhysRevLett.122.034801.

[149] V. Shpakov et al. *Phys. Rev. Lett.* **122**, p. 114801 (11 Mar. 2019). (Cited on pp. 52, 71)
"Longitudinal Phase-Space Manipulation with Beam-Driven Plasma Wakefields"
DOI: 10.1103/PhysRevLett.122.114801.

[150] Y. P. Wu et al. *Phys. Rev. Lett.* **122**, p. 204804 (20 May 2019). (Cited on pp. 52, 71)
"Phase Space Dynamics of a Plasma Wakefield Dechirper for Energy Spread Reduction"
DOI: 10.1103/PhysRevLett.122.204804.

[151] W. K. H. Panofsky and M. Bander. *Review of Scientific Instruments* **39**, 2, pp. 206–212 (1968). (Cited on pp. 52, 71, 75)
"Asymptotic Theory of Beam Break-Up in Linear Accelerators"
DOI: 10.1063/1.1683315.

[152] David H. Whittum et al. *Phys. Rev. Lett.* **67**, pp. 991–994 (8 Aug. 1991). (Cited on pp. 52, 71, 75)
"Electron-hose instability in the ion-focused regime"
DOI: 10.1103/PhysRevLett.67.991.

[153] T. Mehrling et al. *Phys. Rev. ST Accel. Beams* **15**, p. 111303 (11 Nov. 2012). (Cited on p. 52)
"Transverse emittance growth in staged laser-wakefield acceleration"
DOI: 10.1103/PhysRevSTAB.15.111303.

[154] Ralph Assmann and Kaoru Yokoya. *Nuclear Instruments and Methods in Physics Research Section A: Accelerators, Spectrometers, Detectors and Associated Equipment* **410**, 3, pp. 544–548 (1998). (Cited on p. 52)
"Transverse beam dynamics in plasma-based linacs"
DOI: 10.1016/S0168-9002(98)00187-9.

[155] Maxence Thévenet et al. *Phys. Rev. Accel. Beams* **22**, p. 051302 (5 May 2019). (Cited on p. 52)
"Emittance growth due to misalignment in multistage laser-plasma accelerators"
DOI: 10.1103/PhysRevAccelBeams.22.051302.

[156] J. B. Rosenzweig et al. *Phys. Rev. Lett.* **95**, p. 195002 (19 Oct. 2005). (Cited on p. 52)
"Effects of Ion Motion in Intense Beam-Driven Plasma Wakefield Accelerators"
DOI: 10.1103/PhysRevLett.95.195002.

[157] Bryan W Montague, in: *Proceedings of the CAS-ECFA-INFN Workshop: Generation of High Fields for Particle Acceleration to Very-high Energies*. (1984), pp. 208–218. (Cited on p. 52)
"Emittance growth from multiple scattering in the plasma beat-wave accelerator"
DOI: 10.5170/CERN-1985-007.208.

[158] N. Kirby et al., in: *Proceedings of PAC2007*. (2007), pp. 3097–3099. (Cited on p. 52)
"Emittance growth from multiple Coulomb scattering in a plasma wakefield accelerator"
DOI: 10.1109/PAC.2007.4440680.

[159] C. B. Schroeder et al. *Physics of Plasmas* **20**, 8, p. 080701 (Aug. 2013). (Cited on p. 52)
"Control of focusing forces and emittances in plasma-based accelerators using near-hollow plasma channels"
DOI: 10.1063/1.4817799.

[160] C. A. Lindstrøm et al. *arXiv* [physics.acc-ph] (2024). (Cited on pp. 53, 68–70, 75, 77, 103)
"Emittance preservation in a plasma-wakefield accelerator"
DOI: 10.48550/arXiv.2403.17855.

[161] This Figure was produced with help from K. Meenenga. (Cited on p. 57)

[162] William R Leo. Springer. (1994) (Cited on p. 58)
"Techniques for Nuclear and Particle Physics Experiments : A How-To Approach"
DOI: 10.1007/978-3-642-57920-2, ISBN: 978-3-642-57920-2.

[163] A. Buck et al. *Review of Scientific Instruments* **81**, 3, p. 033301 (Mar. 2010). (Cited on p. 59)
"Absolute charge calibration of scintillating screens for relativistic electron detection"
DOI: 10.1063/1.3310275.

[164] Thomas Kurz et al. *Review of Scientific Instruments* **89**, 9, p. 093303 (Sept. 2018). (Cited on pp. 59, 62, 63)
"Calibration and cross-laboratory implementation of scintillating screens for electron bunch charge determination"
DOI: 10.1063/1.5041755.

[165] John Betteley Birks. *Proc. Phys. Soc. A* **64**, pp. 874–877 (1951). (Cited on p. 62)
"Scintillations from Organic Crystals: Specific Fluorescence and Relative Response to Different Radiations"
DOI: 10.1088/0370-1298/64/10/303.

[166] John Betteley Birks. Pergamon Press. (1964) (Cited on p. 62)
"The theory and practice of scintillation counting"
DOI: 10.1016/C2013-0-01791-4, ISBN: 978-0-08-010472-0.

[167] Valeri Lebedev et al. *Phys. Rev. Accel. Beams* **20**, p. 121301 (12 Dec. 2017). (Cited on p. 71)
"Efficiency versus instability in plasma accelerators"
DOI: 10.1103/PhysRevAccelBeams.20.121301.

[168] S. S. Baturin. *arXiv* [physics.acc-ph] (2020). (Cited on p. 71)
"On 'Efficiency versus Instability in plasma accelerators'"
DOI: 10.48550/arXiv.2010.01046.

[169] T. J. Mehrling et al. *Phys. Rev. Accel. Beams* **22**, p. 031302 (3 Mar. 2019). (Cited on p. 71)
"Mechanisms for the mitigation of the hose instability in plasma-wakefield accelerators"
DOI: 10.110/PhysRevAccelBeams.22.031302.

[170] V. E. Balakin et al., in: *12th International Conference on High-Energy Accelerators*. Ed. by Francis T Cole and Rene Donaldson. (Aug. 1983), pp. 119–120. (Cited on p. 71)
"VLEPP: Transverse beam dynamics"
URL: https://inspirehep.net/literature/198113.

[171] T. J. Mehrling et al. *Phys. Rev. Lett.* **121**, p. 264802 (26 Dec. 2018). (Cited on p. 72)
"Suppression of Beam Hosing in Plasma Accelerators with Ion Motion"
DOI: 10.1103/PhysRevLett.121.264802.

[172] C. A. Lindstrøm. PhD thesis. University of Oslo, Oslo, 2019. (Cited on p. 75)
"Emittance growth and preservation in a plasma-based linear collider"
URL: http://urn.nb.no/URN:NBN:no-69347.

[173] C. A. Lindstrøm, private communication (2024). (Cited on pp. 78, 103)

[174] O Jakobsson et al. *Plasma Physics and Controlled Fusion* **61**, 12, p. 124002 (Oct. 2019). (Cited on p. 78)
"Tailored plasma-density profiles for enhanced energy extraction in passive plasma beam dumps"
DOI: 10.1088/1361-6587/ab4cfb.

[175] S. Chou et al. *Phys. Rev. Lett.* **117**, p. 144801 (14 Sept. 2016). (Cited on p. 78)
"Collective Deceleration of Laser-Driven Electron Bunches"
DOI: 10.1103/PhysRevLett.117.144801.

[176] F. Peña et al. *arXiv* [physics.acc-ph] (2023). (Cited on pp. 80, 83, 86, 91, 95, 103, 106)
"Energy Depletion and Re-Acceleration of Driver Electrons in a Plasma-Wakefield Accelerator"
DOI: 10.48550/arXiv.2305.09581.

[177] C. A. Lindstrøm et al. *Phys. Rev. Accel. Beams* **23**, p. 052802 (5 May 2020). (Cited on p. 81)
"Matching small β functions using centroid jitter and two beam position monitors"
DOI: 10.1103/PhysRevAccelBeams.23.052802.

[178] J.-L. Vay. *Phys. Rev. Lett.* **98**, p. 130405 (13 Mar. 2007). (Cited on p. 82)
"Noninvariance of Space- and Time-Scale Ranges under a Lorentz Transformation and the Implications for the Study of Relativistic Interactions"
DOI: 10.1103/PhysRevLett.98.130405.

[179] Remi Lehe et al. *Computer Physics Communications* **203**, pp. 66–82 (2016). (Cited on pp. 79, 82)
"A spectral, quasi-cylindrical and dispersion-free Particle-In-Cell algorithm"
DOI: 10.1016/j.cpc.2016.02.007.

[180] R. Courant et al. *Mathematische Annalen* **100**, 1, pp. 32–74 (1928). (Cited on p. 82)
"Über die partiellen Differenzengleichungen der mathematischen Physik"
DOI: 10.1007/BF01448839.

[181] Amina E Hussein et al. *Scientific reports* **9**, 1, p. 3249 (2019). (Cited on p. 84)
"Laser-wakefield accelerators for high-resolution X-ray imaging of complex microstructures"
DOI: 10.1038/s41598-019-39845-4.

[182] C Zhang et al. *Plasma Physics and Controlled Fusion* **66**, 2, p. 025013 (Jan. 2024). (Cited on p. 96)
"Generation of meter-scale hydrogen plasmas and efficient, pump-depletion-limited wakefield excitation using 10 GeV electron bunches"
DOI: 10.1088/1361-6587/ad1ae4.

[183] Gwanghui Ha et al. *Phys. Rev. Accel. Beams* **23**, p. 072803 (7 2020). (Cited on p. 97)
"Coherent synchrotron radiation free longitudinal bunch shaping using transverse deflecting cavities"
DOI: 10.1103/PhysRevAccelBeams.23.072803.

[184] Ingo Will and Guido Klemz. *Opt. Express* **16**, 19, pp. 14922–14937 (Sept. 2008). (Cited on p. 97)
"Generation of flat-top picosecond pulses by coherent pulse stacking in a multicrystal birefringent filter"
DOI: 10.1364/OE.16.014922.

[185] Gregor Loisch et al. *Physical Review Letters* **121**, 6, p. 064801 (2018). (Cited on p. 97)
"Observation of high transformer ratio plasma wakefield acceleration"
DOI: 10.1103/PhysRevLett.121.064801.

[186] R. Roussel et al. *Phys. Rev. Lett.* **124**, p. 044802 (4 Jan. 2020). (Cited on p. 97)
"Single Shot Characterization of High Transformer Ratio Wakefields in Nonlinear Plasma Acceleration"
DOI: 10.1103/PhysRevLett.124.044802.

[187] E. Gschwendtner et al. *Nuclear Instruments and Methods in Physics Research Section A: Accelerators, Spectrometers, Detectors and Associated Equipment* **829**, pp. 76–82 (2016). (Cited on p. 98)
"AWAKE, The Advanced Proton Driven Plasma Wakefield Acceleration Experiment at CERN"
DOI: 10.1016/j.nima.2016.02.026.

[188] M. Röhrs and DESY. Dr. Hamburg: Univ. Hamburg, 2008. (Cited on p. 104)
"Investigation of the Phase Space Distribution of Electron Bunches at the FLASH-Linac Using a Transverse Deflecting Structure"
URL: https://doi.org/10.3204/DESY-THESIS-2008-012.

[189] Siegfried Schreiber, Head FLASH Accelerator, private communication (2023). (Cited on p. 106)

[190] Winfried Decking, head of the European XFEL accelerator operation, private communication (2023). (Cited on p. 106)

[191] Andrey Yu Baikov et al. *IEEE Transactions on Electron Devices* **62**, 10, pp. 3406–3412 (2015). (Cited on p. 108)
"Toward High-Power Klystrons With RF Power Conversion Efficiency on the Order of 90%"
DOI: 10.1109/TED.2015.2464096.

[192] Ángel Ferran Pousa et al., in: *8th International Particle Accelerator Conference*. (May 2017). (Cited on p. 122)
"VisualPIC: A New Data Visualizer and Post-Processor for Particle-in-Cell Codes"
DOI: 10.18429/JACoW-IPAC2017-TUPIK007.